Computational neuroscience models at different levels of abstraction for synaptic plasticity, astrocyte modulation of synchronization and systems memory consolidation

Lisa Blum Moyse

N°d'ordre NNT : 2023ISAL0058

THESE de DOCTORAT DE L'INSA LYON, membre de l'Université de Lyon

Ecole Doctorale 512
InfoMaths

Spécialité/ discipline de doctorat :
Informatique

Soutenue publiquement le 14/09/2023, par:
Lisa Blum Moyse

Computational neuroscience models at different levels of abstraction for synaptic plasticity, astrocyte modulation of synchronization and systems memory consolidation

---

Devant le jury composé de :

Delord, Bruno Président du jury, Examinateur	Professeur	Sorbonne Université, Paris
Clopath, Claudia Rapporteure	Professor	Imperial College London, UK
Desroches, Mathieu Rapporteur	Chargé de Recherche HDR	Inria, Sophia-Antipolis
Rouzaud-Cornabas, Jonathan Examinateur	Maître de conférence	Insa Lyon
Berry, Hugues Directeur de thèse	Directeur de recherche	Inria, Lyon

INSTITUT NATIONAL DES SCIENCES APPLIQUÉES LYON

Département de la Formation par la Recherche et des Études Doctorales (**FEDORA**)

Bâtiment INSA direction, 1er étage
37, av. J. Capelle
69621 Villeurbanne Cédex
fedora@insa-lyon.fr

Référence : TH0989_ Lisa BLUM MOYSE
L'INSA Lyon a mis en place une procédure de contrôle systématique via un outil de détection de similitudes (logiciel Compilatio). Après le dépôt du manuscrit de thèse, celui-ci est analysé par l'outil. Pour tout taux de similarité supérieur à 10%, le manuscrit est vérifié par l'équipe de FEDORA. Il s'agit notamment d'exclure les auto-citations, à condition qu'elles soient correctement référencées avec citation expresse dans le manuscrit.

Par ce document, il est attesté que ce manuscrit, dans la forme communiquée par la personne doctorante à l'INSA Lyon, satisfait aux exigences de l'Etablissement concernant le taux maximal de similitude admissible.

INSA LYON
Campus LyonTech La Doua
20, avenue Albert Einstein - 69621 Villeurbanne cedex - France
Tél. +33 (0)4 72 43 83 83 - Fax +33 (0)4 72 43 85 00
www.insa-lyon.fr

membre de UNIVERSITÉ DE LYON

Département FEDORA – INSA Lyon - Ecoles Doctorales

SIGLE	ECOLE DOCTORALE	NOM ET COORDONNEES DU RESPONSABLE
CHIMIE	**CHIMIE DE LYON** **https://www.edchimie-lyon.fr** Sec. : Renée EL MELHEM Bât. Blaise PASCAL, 3e étage secretariat@edchimie-lyon.fr	**M. Stéphane DANIELE** C2P2-CPE LYON-UMR 5265 Bâtiment F308, BP 2077 43 Boulevard du 11 novembre 1918 69616 Villeurbanne **directeur@edchimie-lyon.fr**
E.E.A.	**ÉLECTRONIQUE, ÉLECTROTECHNIQUE, AUTOMATIQUE** **https://edeea.universite-lyon.fr** Sec. : Stéphanie CAUVIN Bâtiment Direction INSA Lyon Tél : 04.72.43.71.70 secretariat.edeea@insa-lyon.fr	**M. Philippe DELACHARTRE** INSA LYON Laboratoire CREATIS Bâtiment Blaise Pascal, 7 avenue Jean Capelle 69621 Villeurbanne CEDEX Tél : 04.72.43.88.63 **philippe.delachartre@insa-lyon.fr**
E2M2	**ÉVOLUTION, ÉCOSYSTÈME, MICROBIOLOGIE, MODÉLISATION** **http://e2m2.universite-lyon.fr** Sec. : Bénédicte LANZA Bât. Atrium, UCB Lyon 1 Tél : 04.72.44.83.62 secretariat.e2m2@univ-lyon1.fr	**Mme Sandrine CHARLES** Université Claude Bernard Lyon 1 UFR Biosciences Bâtiment Mendel 43, boulevard du 11 Novembre 1918 69622 Villeurbanne CEDEX **sandrine.charles@univ-lyon1.fr**
EDISS	**INTERDISCIPLINAIRE SCIENCES-SANTÉ** **http://ediss.universite-lyon.fr** Sec. : Bénédicte LANZA Bât. Atrium, UCB Lyon 1 Tél : 04.72.44.83.62 secretariat.ediss@univ-lyon1.fr	**Mme Sylvie RICARD-BLUM** Institut de Chimie et Biochimie Moléculaires et Supramoléculaires (ICBMS) - UMR 5246 CNRS - Université Lyon 1 Bâtiment Raulin - 2ème étage Nord 43 Boulevard du 11 novembre 1918 69622 Villeurbanne Cedex Tél : +33(0)4 72 44 82 32 **sylvie.ricard-blum@univ-lyon1.fr**
INFOMATHS	**INFORMATIQUE ET MATHÉMATIQUES** **http://edinfomaths.universite-lyon.fr** Sec. : Renée EL MELHEM Bât. Blaise PASCAL, 3e étage Tél : 04.72.43.80.46 infomaths@univ-lyon1.fr	**M. Hamamache KHEDDOUCI** Université Claude Bernard Lyon 1 Bât. Nautibus 43, Boulevard du 11 novembre 1918 69 622 Villeurbanne Cedex France Tél : 04.72.44.83.69 **hamamache.kheddouci@univ-lyon1.fr**
Matériaux	**MATÉRIAUX DE LYON** **http://ed34.universite-lyon.fr** Sec. : Yann DE ORDENANA Tél : 04.72.18.62.44 yann.de-ordenana@ec-lyon.fr	**M. Stéphane BENAYOUN** Ecole Centrale de Lyon Laboratoire LTDS 36 avenue Guy de Collongue 69134 Ecully CEDEX Tél : 04.72.18.64.37 **stephane.benayoun@ec-lyon.fr**
MEGA	**MÉCANIQUE, ÉNERGÉTIQUE, GÉNIE CIVIL, ACOUSTIQUE** **http://edmega.universite-lyon.fr** Sec. : Stéphanie CAUVIN Tél : 04.72.43.71.70 Bâtiment Direction INSA Lyon mega@insa-lyon.fr	**M. Jocelyn BONJOUR** INSA Lyon Laboratoire CETHIL Bâtiment Sadi-Carnot 9, rue de la Physique 69621 Villeurbanne CEDEX **jocelyn.bonjour@insa-lyon.fr**
ScSo	**ScSo*** **https://edsciencessociales.universite-lyon.fr** Sec. : Mélina FAVETON INSA : J.Y. TOUSSAINT Tél : 04.78.69.77.79 melina.faveton@univ-lyon2.fr	**M. Bruno MILLY** Université Lumière Lyon 2 86 Rue Pasteur 69365 Lyon CEDEX 07 **bruno.milly@univ-lyon2.fr**

*ScSo : Histoire, Géographie, Aménagement, Urbanisme, Archéologie, Science politique, Sociologie, Anthropologie

Remerciements
Acknowledgments

Je tiens à remercier mon directeur de thèse, Hugues Berry, pour m'avoir encadrée pendant ces trois années avec beaucoup de patience et de compréhension, et grâce à qui j'ai beaucoup appris scientifiquement et humainement.
I would like to thank all other members of my committee for accepting to examine my thesis: Pr Claudia Clopath, Dr Mathieu Desroches, Pr Bruno Delord, and Pr Jonathan Rouzaud-Cornabas.
Merci à Srdjan Ostojic et à Guillaume Damiand pour avoir été membres de mon comité de suivi de thèse et pour leurs réflexions intéressantes.
Merci à l'INSA de Lyon pour le financement de cette thèse. Merci à l'INRIA et au LIRIS pour m'avoir accueillie.
Merci à mes collaborateurs et collaboratrices Laurent Venance, Marie Vandecasteele, Elodie Perrin, Nicolas Gervasi du Collège de France pour les échanges et leur patience.

Je souhaite remercier chaleureusement toutes les personnes travaillant à l'INRIA que j'ai pu côtoyer ces dernières années.

Merci à Laetitia pour tes aides précieuses, ta patience et ta gentillesse toutes ces années
Merci à Jonathan Rouzaud-Cornabas pour ta bonne humeur, tes conseils, ton aide précieuse pour améliorer le script du réseau neurones-astrocytes
Merci à Samuel Bernard pour les idées sur les chimères dans les réseaux qui ont beaucoup fait avancer les choses
Merci Léo pour toutes les choses intéressantes, ta vision du monde et tes rires
Merci à Guillaume pour ton empathie et tous les conseils!
Merci à Thomas pour ta bonne humeur et tes aides précieuses pour triompher de l'imprimante!

Merci à toi Paul pour ton soutien, ta compréhension et pour toutes les invitations chez toi!
Merci Aurélien pour ton humour, ton aide dans l'organisation des week-ends, et les discussions philosophiques autour d'un plat de pâtes
Merci à Julie pour les petit-déjs matinaux, nos discussions très intéressantes, ton empathie et ta sensibilité
Merci à Marco pour ta bonne humeur, tes jeux de mots de qualité et tes chants polyphoniques qui ont illuminé mes journées
Merci à Théotime pour les sorties, la coloc, et pour m'avoir fait découvrir le son des vinyles!
Merci à Romain, pour tes dessins incroyables au tableau, tes jeux de mots, ton T-shirt avocats, les photos de tes chats!
Merci à toi Mirabelle pour toutes nos discussions, tes réflexions, ton soutien!
Merci à Hana pour nos discussions, ta sympathie et ta gentillesse
Merci à Nicolas pour ton humour, ton amour du beurre et de la Bretagne, et ta voiture (je rigole)
Merci à Arsène pour ton enthousiasme communicatif au volley et ta maîtrise approximative du canoë
Merci à Charlotte pour tes sourires et ton humour!
Merci à Laurent pour ton rire communicatif, et les bon plans théâtre!
Merci Lisa pour ta bonne humeur et toutes les informations importantes que tu connais sur la vie du centre et la recherche!
Merci à Nathan pour ta joie de vivre, les foots et volleys du midi
Merci à Arnaud pour tes concerts au melodica, ta décontraction et les discussions scientifiques
Merci à Juliette pour tes rires, et pour toutes tes réflexions intéressantes

Merci à tout·e·s celleux de l'INRIA que je connais un peu moins, merci pour tout! Vos sourires et votre bonne humeur sont communicatifs! Merci à Claire, Salwa, Stéphane, Anne-Laure, Anton, Christophe, Carole, David, Eric, Mostafa, Audrey, Mike, Elie, Lionel, Salim, Guillaume, Zoé, Manon, et tout·e·s les autres!

Merci à tout·e·s les autres ami·e·s en dehors.

Un spécial merci à Mirabelle, Nicolas, Pepper et Noah pour m'avoir accueillie si gentiment plusieurs fois!

Un grand merci à vous l'Ovalie!
Merci à toi Valéri pour toutes nos longues discussions, les sorties, l'Italie, ta générosité, ta vision du monde et la force que tu as pour défendre tes valeurs
Merci Loïc pour ton amitié toutes ces années, ton humour et ton rire, ton soutien, tes expressions non homologuées, ton amour pour Goldman et les pâtes, et surtout ton sens des valeurs

Merci à toute la coloc élargie! Sans vous ces dernières années n'auraient pas été les mêmes. Merci pour votre générosité pour accueillir des squatteureuses comme moi, les repas, les vacances, les soirées. Sans vous je n'aurais pas découvert de réfs internet d'une si grande qualité, ni connu les genoux après insanity!
Merci à toi Clem pour ton amitié, ton soutien et ta passion pour la physique!
Merci à Sasha pour ta générosité et ta gentillesse qui sont immenses!
Merci Nacim pour tes citations, l'attention que tu portes à tes ami·e·s, et tes crêpes évidemment
Merci Fred pour ton accueil, ta joie de vivre et ta passion du babyfoot
Merci Colléaux pour tes anecdotes de niveau 0 comme de niveau 1000, tes jeux de mots, ton amour pour Kaamelott
Merci Sophie pour tes rires communicatifs, tes valeurs et ta sensibilité
Merci Lily pour ton sens des valeurs, tes réflexions toujours intéressantes et ton énergie
Merci Manon pour ta bonne humeur, les parties de jeux de société et tes currys incroyables!

Merci aussi à toi Arnaud, pour ton humour et tous les moments en amphi comme au foyer!
Merci Chrysostome pour nos discussions, pour ton enthousiasme communicatif pour la physique!
Merci également à tout·e·s les autres! Ambroise, Blandine, Charles, Rémi, Solène, Lise, Nico, Pascal, Lorianne, Laetitia, Guillaume, Hector, Claire...

Merci à mes amies de prépa pour leur soutien toutes ces années.
Merci Mélissandre pour ton énergie et ta bonne humeur qui sont sans commune mesure!
Merci Caro pour tes blagues de qualité, ton amour du fromage et du rock.
Merci Pauline pour ton sens de la fête et ton amitié!
Merci également à tout·e·s les autres, Emile, Othman, Lauranne, Salma, Anaïs, Emmeline, Camille, Paul...

Merci à mes ami·e·s de Bordeaux, merci pour tous les moments partagés et votre soutien! Eulalie, Estelle, Ludivine, Alexandre, Clément, Valentin, Océane...

Enfin un très grand merci à ma famille!
Merci à Frédérique et à Laurent pour votre soutien et votre affection toutes ces années!
Merci à mes frangin·e·s Pauline et Axel pour votre bonne humeur et tous les moments partagés
Merci à mes grand-parents Raymonde, Jacques, Corinne et Jean-Michel pour votre gentillesse et votre patience
Et merci à tout·e·s les autres, Nathalie, Jérôme, Mirabelle, Jérémie, Alain, Benjamin, Louise, Barbara, Virginie, François, Morgane, Nathan, Stéphane, Ouardia, Basile, Arsène, Noor-Clément, pour votre joie de vivre et votre soutien!

Résumé

Dans cette thèse, des modèles théoriques à niveaux d'abstraction croissants sont développés pour aborder des questions issues d'expériences de neuroscience. Ils sont étudiés par des approches numériques et analytiques.

Avec le laboratoire de Laurent Venance (Paris), nous avons développé un modèle du protocole ITDP (input-timing-dependent plasticity) pour la plasticité des synapses cortico- et thalamo-striatales. Le modèle a été calibré par des données ex vivo et permettra de déterminer la présence de plasticité synaptique in vivo, lors d'expériences de comportement visant à déterminer le rôle des entrées corticales et thalamiques dans l'apprentissage moteur.

Au niveau des populations neuronales, j'ai étudié la modulation des comportements collectifs neuronaux par les astrocytes, en particulier la synchronisation Up-Down, une alternance spontanée entre des périodes de forte activité collective et des périodes de silence. J'ai proposé des modèles de fréquence de décharge et de réseaux de neurones à spikes de populations interconnectées de neurones et d'astrocytes. Ils proposent des explications sur la façon dont les astrocytes induisent les transitions Up-Down.
Les astrocytes sont aussi probablement impliqués dans la génération des crises d'épilepsie, pendant lesquelles la synchronisation neuronale est altérée. Sur la base des modèles précédents, j'ai développé un réseau neurone-astrocyte avec une connectivité en clusters, montrant la transition entre des dynamiques Up-Down et des événements de très forte activité mimant une crise d'épilepsie.

Enfin, au niveau du cerveau lui-même, j'ai étudié la théorie standard de la consolidation, selon laquelle la mémoire à court terme dans l'hippocampe permet la consolidation de la mémoire à long terme dans le néocortex. J'ai cherché à expliquer ce phénomène en intégrant des hypothèses biologiques – taille du néocortex expliquant la lenteur de l'apprentissage, et neurogenèse dans l'hippocampe expliquant l'effacement de sa mémoire – dans un modèle de champs neuronaux interconnectés qui reproduit bien les principales caractéristiques de la théorie.

Mots clés : neurosciences computationnelles, plasticité dépendante de la synchronisation des entrées, astrocytes, synchronisation, champs neuronaux, théorie de la consolidation des systèmes

Abstract

In this thesis, theoretical models with increasing levels of abstraction are developed to address questions arising from neuroscience experiments. They are studied using numerical and analytical approaches.

With Laurent Venance's laboratory (Paris), we have developed an ITDP (input-timing-dependent plasticity) protocol model for the plasticity of cortico- and thalamo-striatal synapses. The model has been calibrated with ex vivo data and will be used to determine the presence of synaptic plasticity in vivo, in behavioral experiments aimed at determining the role of cortical and thalamic inputs in motor learning.

At the level of neuronal populations, I have studied the modulation of neuronal collective behaviors by astrocytes, in particular Up-Down synchronization, a spontaneous alternation between periods of high collective activity and periods of silence. I have proposed rate and spiking neural network models of interconnected populations of neurons and astrocytes. They offer explanations of how astrocytes induce Up-Down transitions.
Astrocytes are also probably involved in the generation of epileptic seizures, during which neuronal synchronization is impaired. Based on the above models, I have developed a neuron-astrocyte network with a cluster connectivity, showing the transition between Up-Down dynamics and events of very high activity mimicking an epileptic seizure.

Finally, at the level of the brain itself, I studied the standard theory of consolidation, according to which short-term memory in the hippocampus enables the consolidation of long-term memory in the neocortex. I have sought to explain this phenomenon by integrating biological hypotheses – the size of the neocortex explaining the slowness of learning, and neurogenesis in the hippocampus explaining the erasure of its memory – into a model of interconnected neural fields that well reproduces the main features of the theory.

Key words: computational neuroscience, input-timing-dependent plasticity, astrocytes, synchronization, neural fields, systems consolidation theory

List of scientific productions

Publications

Blum Moyse, L., & Berry, H. (2023). Modelling memory consolidation at a systems level with neural fields.
Preprint

Blum Moyse, L., & Berry, H. (2022). Modelling the modulation of cortical Up-Down state switching by astrocytes. *PLoS Computational Biology, 18*(7), e1010296.
https://doi.org/10.1371/journal.pcbi.1010296

Communications

Modelling Systems Memory Consolidation with neural fields (poster)
COSYNE: Computational and Systems Neuroscience, Conference
Lisbon, Portugal, March 2022

Systems consolidation model: How does the hippocampus guide the reorganization of the information stored in the neocortex (poster)
Statistical Mechanics and Emergent Phenomena in Biology, summer school
Beg Rohu, France, June 2021

Contents

List of Figures

List of Tables

Abbreviations

Chapter 1

LTP	Long-term potentiation
LTD	Long-term depression
STDP	Spike-timing-dependent plasticity

Chapter 2

ITDP	Input-timing-dependent plasticity
MSN	Medium-sized spiny neuron
S2	Secondary somatosensory cortex
Pf	Parafascicular nucleus of the thalamus
CS	Corticostriatal
TS	Thalamostriatal
EPSP	Excitatory postsynaptic potential
LFP	Local field potential
EEG	Electroencephalography

Chapter 3

E	Excitatory neurons
I	Inhibitory neurons
A	Astrocytes
IAF	Integrate-and-fire

Chapter 4

SCT	Standard consolidation theory
C	Neocortex
H	CA1-CA3
D	Dentate Gyrus

Chapter 1

An introduction to models and levels of abstraction in computational neuroscience

1.1 The computational approach in neuroscience and the different levels of abstraction

In order to connect brain processes observations and theories, modelling approaches have been widely used in neuroscience in the last decades [208]. Indeed, models constitute a useful tool to clarify or quantify a phenomenon. A key step in their development is the identification and implementation of the relevant elements for the phenomenon description. Among the different types of models, those constituted with mathematical equations or algorithms are of particular interest in neuroscience, since they can be used for simulation and/or theoretical analysis, and can be assessed and fitted with results of corresponding experiments.

The field that uses such models in neuroscience is named computational, theoretical or mathematical neuroscience [225]. This research area aims to model mechanistics and cognitive observations with biologically plausible systems, which is a different approach from artificial neural networks for instance, even if many exchanges occur between the disciplines [210]. Various models have been introduced to study neuroscience issues at multiple spatiotemporal scales, which go from the detailed mechanisms generating action potentials to cognitive processes, such as memory, and their predictions can be assessed with biological or psychological experiments [225, 92].
Depending on the spatiotemporal scales studied, different abstraction levels are chosen. For example in neural networks, it is often useful to "summarize" the detailed mechanisms of action potentials integration and formation into a simple firing rate function, since the aim here is to prioritize details at that scale (network), while further simplifying details at others smaller (cellular) and larger (brain area) scales [36]. Each model at a given level of abstraction could be seen as a dimensionality reduction of lower level models. This simplification is permitted by the fact that there is a large number of parameter space dimensions along which parameters can fluctuate without having a significant impact on pertinent higher level features. For example, in mammals, individual synaptic weights are usually small and have individually little influence on the postsynaptic neurons. Presence or absence of an individual synapse is therefore usually not significant at the overall level of neuronal population [129, 237]. Such dimensions are "removed" or replaced by averages or homogeneized quantities, and only dimensions that have a significant effect on the higher-level system characteristics are kept [152]. The ways to reduce the size of the parameter space go from simple methods, such as averaging or considering an asymptotic behaviour [240], to nonlinear and complex approachs [192].

In this thesis, models at different spatiotemporal scales and suitable levels of abstraction were developed, see figure 1.1, and used to study some topics in neuroscience. We provide in the following introduction a rapid overview of classical models in computational neuroscience at different spatial

levels of abstraction, with a detailed focus on models of interest to better understand the works carried out during this thesis.

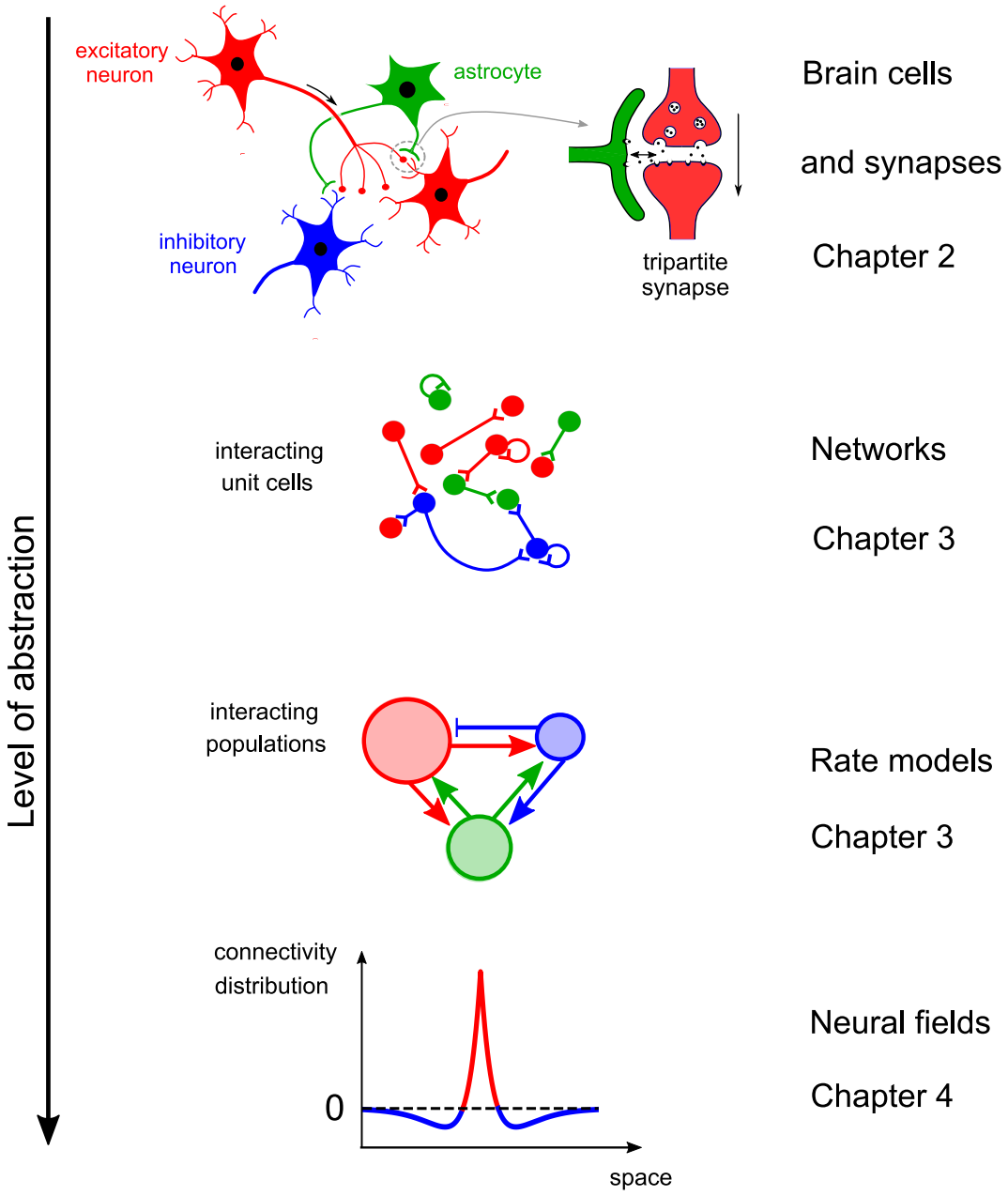

Figure 1.1: Different levels of spatial abstraction in computational neuroscience. The color code is the same for the different drawings: red for excitatory neurons, blue for inhibitory neurons and green for astrocytes. Models presented here are used in the differents chapters of the thesis, at a single-cell and synapse scale in chapter 2, networks in chapter 3 and spatial continuum (rate in chapter 3 and neural fields in chapter 4).

1.2 Single-cell and synapse dynamics modelling

1.2.1 Overview

A single brain cell is a complex biophysical entity, which can interact with multiple other cells [92].

Neurons The brain's basic processing units are thought to be neurons. A well-known model of their dynamics is the Hodgkin-Huxley model [109]. This mathematical model describes how action potentials are formed and propagated. It is defined by four nonlinear differential equations (1.1)(1.3)(1.4)

(1.5), that reproduce the electrical dynamics, by describing ion channels and ion current flows. The total current per unit area $I(t)$ is defined as:

$$I(t) = C\frac{du}{dt} + \sum_k I_k(t) \tag{1.1}$$

with the voltage u, the capacity C and the sum of the ionic currents defined by

$$\sum_k I_k(t) = g_{\mathrm{Na}} m^3 h(u - E_{\mathrm{Na}}) + g_{\mathrm{K}} n^4 (u - E_{\mathrm{K}}) + g_L(u - E_L) \tag{1.2}$$

g_{Na}, g_{K} and g_L are respectively the sodium, potassium and leak conductances per unit area. E_{Na}, E_{K} and E_L denote respectively the sodium, potassium and leak equilibrium potentials. The three gating variables m, n and h evolve according to

$$\frac{dm}{dt} = \alpha_m(u)(1 - m) - \beta_m(u)m \tag{1.3}$$

$$\frac{dn}{dt} = \alpha_n(u)(1 - n) - \beta_n(u)n \tag{1.4}$$

$$\frac{dh}{dt} = \alpha_h(u)(1 - h) - \beta_h(u)h \tag{1.5}$$

α_i and β_i, for $i \in \{m, n, h\}$, are rate constants dependent on the voltage u.

To better visualize the behaviours of this model, methods of phase plane analysis and dimension reduction can be useful [92]. These are generic tools that can be used in many models in theoretical neuroscience.
Similar single-neuron models exist with simpler expressions, for example the Morris-Lecar model [169], the FitzHugh-Nagumo [80, 174], or the Hindmarsch-Rose [3]. But the Hodgkin-Huxley also serves as a basis for detailed biophysical neuron models with more types of currents. Indeed the set of ion channels is different from one neuron to the next and determines its electrical characteristics [132]. Using similar descriptions, there also exist models named compartmental models that describe the arrangment of synapses on the dendritic tree. Indeed, these details of the subcellular structure has an important effect on signals integration [35].

Synapses Neurons are not isolated entities but are interconnected, they transmit and receive action potentials through synapses. The synaptic transmission process consists schematically in a release of neurotransmitters into the synaptic cleft by a presynaptic neuron, which will activate receptors and induce a postsynaptic current [165]. Both detailed biophysical or simple phenomenological models exist to describe synaptic kinetics [196]. An example of such phenomenological model is the description of the synaptic conductance $g_{\mathrm{syn}}(t)$ with an alpha function [229]:

$$g_{\mathrm{syn}}(t) = G_{\mathrm{syn}} \frac{t - t_0}{\tau} e^{\frac{1-(t-t_0)}{\tau}} \tag{1.6}$$

With G_{syn} the peak amplitude and τ a time constant. This function peaks at a time $t = t_0 + \tau$.

Tripartite synapse: modulation by astrocytes Synaptic transmission is not only an affair of neurons, it can be modulated by astrocytes. In the past three decades, it has become clear that these star-shaped glial cells not only procure a structural support, but also have a role in signaling through interactions with neurons at a "tripartite synapse" [58]. This structure is typically constituted with a pre- and postsynapse enveloped by an astrocyte extension (named process). While astrocytes do not generate action potentials, they can detect neurotransmitters, such as glutamate, and encode this signal into the dynamics of their cytosolic Ca^{2+}. In response, they can release molecules named gliotransmitters, such as glutamate, which will activate neurons [183]. Nevertheless, it is important to note that it is still uncertain whether the concept of gliotransmission is effective in vivo [204].
Astrocytic dynamics in computational models of tripartite synapses can be either defined in an abstract way, or be more descriptive, with the details of membrane transport processes for example [181, 157]. All in all, computational models that include astrocytes share similar features with those describing neurons.

Modelling Dynamic Synapses Synapses are dynamical entities, that can strengthen or weaken with time in a way that depends on past neuronal activity. This process is called synaptic plasticity, and occurs through mechanisms at different timescales [196]. For example, short-term synaptic plasticity is a widespread form of fast modulation of synaptic efficacy (timescale from 10 ms to a few minutes). This activity-dependent process can cause both potentiation and depression [105]. Different phenomenological models exist to describe this effect, such as the model of Tsodyks and Markram [227, 228], where a set of differential equations describes the evolution of the fractions of synaptic resources in respectively the recovered (x), active (y), and inactive states (z):

$$\frac{dx}{dt} = \frac{z}{\tau_{\text{rec}}} - ux\delta(t - t_{\text{sp}}) \tag{1.7}$$

$$\frac{dy}{dt} = -\frac{y}{\tau_{\text{I}}} + ux\delta(t - t_{\text{sp}}) \tag{1.8}$$

$$\frac{dz}{dt} = \frac{y}{\tau_{\text{I}}} - \frac{z}{\tau_{\text{rec}}} \tag{1.9}$$

With the different time constants: t_{sp} is the timing of presynaptic spikes, τ_{I} is the decay constant of postsynaptic currents, and τ_{rec} is the recovery time from synaptic depression.
Furthermore, the variable u describes the effective "use" of synaptic resources, that increases for each presynaptic spike and decreases towards its initial value with a time constant τ_{facil}:

$$\frac{du}{dt} = -\frac{u}{\tau_{\text{facil}}} + U(1 - u)\delta(t - t_{\text{sp}}) \tag{1.10}$$

Another form of plasticity occurring at a larger timescale is long-term plasticity, through long-term potentiation (LTP) and long-term depression (LTD). LTP and LTD are respectively a persistent strengthening and decrease in synaptic strength, triggered by short activity sequences and maintained over large time periods [220]. Several biological processes underly this type of plasticity that some models aimed to detail [106, 196], but a usual modelling choice is a simple rate-based description, such as the Hebbian learning [209], covariance [207], Oja's [179] or Bienenstock-Cooper-Munro (BCM) [27] rules.

For instance, the BCM rule modulates the LTP-LTD modification threshold θ_M depending on average postsynaptic activity y, typically by computing the power of the mean of y, scaled by a parameter y_0 :

$$\theta_M = E^p[y/y_0] \tag{1.11}$$

with y computed as:

$$y = \sum_i w_i x_i \tag{1.12}$$

x_i is the i^{th} presynaptic activity, and w_i the synaptic weight, which evolves according to:

$$\frac{dw_i}{dt} = y(y - \theta_M)x_i - \epsilon w_i \tag{1.13}$$

with ϵ a positive constant.
Nevertheless, synaptic weight modifications do not only rely on mean firing rates, but also on the specific temporal order of pre- and postsynaptic spikes, a phenomenon known as spike-timing-dependent plasticity (STDP) [39].

1.2.2 An example: a spike-timing-dependent plasticity model

STDP is a biological process through which synaptic weights can be strengthened (LTP) or decreased (LTD) in an activity-dependent way, following the timing between pre and postsynaptic spikes [81]. In the last two decades, this phenomenon has been extensively investigated and experimentally studied for different types of synapses [39].

Experimentally, STDP results are measured by an iteration (around 100 times, with a 0.1 Hz frequency) of pre (t_{pre}) and post-synaptic (t_{post}) paired stimulations. We note $\Delta t = t_{post} - t_{pre}$ the

interval between the two activations, see figure 1.2 (A). The STDP experiments are most often carried out ex vivo or in vitro, so that the firing of one postsynaptic neuron can be finely tuned. Figure 1.2 (B) represents schematically the modifications of synaptic weights as a function of the interval between the pre and post spikes Δt. In the case $\Delta t > 0$, LTP is induced, while for $\Delta t < 0$, LTD is observed. This type of plasticity is classified as Hebbian. These changes do not happen anymore for large Δt values, typically for $|\Delta t| > 50$ ms [232].

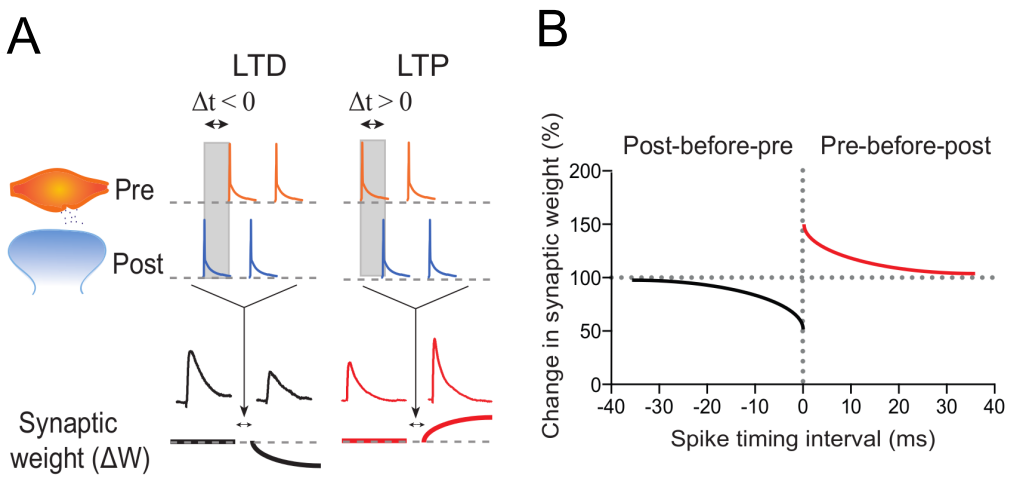

Figure 1.2: Spike-timing-dependent plasticity (STDP) protocol for a Hebbian plasticity, adapted from Brzosko et al. (2019) [39]. **(A)** STDP is carried out through repeated paired pre- and postsynaptic spikes separated by Δt of the order of a few milliseconds, that induce synaptic weight modifications (ΔW). **(B)** For a classic Hebbian case, pre-before-post spike pairings induce long-term potentiation (LTP), while post-before-pre pairings induce long-term depression (LTD). The percentage of change in synaptic weight is a measure of synaptic plasticity.

Theoretically, several models detailing pre- and postsynaptic spikes timing were proposed to reproduce STDP results. Such models can take the form of an abstract exponentially decaying synaptic rule [196], to mimic the figure 1.2 (B) for the synaptic weight w:

$$\Delta w = A \ \mathrm{sign}(t_{\mathrm{pre}} - t_{\mathrm{post}}) \exp(-|t_{\mathrm{pre}} - t_{\mathrm{post}}|/\tau_{\mathrm{STDP}}) \tag{1.14}$$

With A the baseline value and τ_{STDP} a time scale that corresponds to the time window for the spikes interaction. While this rule is very simple, STDP models can take the form of more complex phenomenological approaches [49], and can include detailed biophysical components that describe different intracellular pathways [97].
We describe here a model of STDP inbetween detailed biophysical and more phenomenological models, developed by Graupner and Brunel in 2012 [98], which provides an understanding of the link between calcium dynamics and the observed diversity of synaptic plasticity.

This model describes a single synapse receiving pre- and postsynaptic spikes. Its state is described by $\rho(t)$, a synaptic efficacy variable, which evolves according to the stochastic differential equation:

$$\tau \frac{d\rho}{dt} = -\rho(1-\rho)(\rho^* - \rho) + \gamma_p(1-\rho)\Theta[c(t) - \theta_p] - \gamma_d \rho \Theta[c(t) - \theta_d] + Noise(t) \tag{1.15}$$

The t dependency of ρ have not been noted in the equation for an easier comprehension.
τ is a time constant of the synaptic efficacy modifications, whose value is between a few seconds to minutes. The evolution of $\rho(t)$ without stimulations is described by the first term on the right-hand side, a cubic function. Thus, there are three stationary states for the noiseless equations: two stable states corresponding to a low ($\rho = 0$) and a high efficacy ($\rho = 1$), and an unstable boundary inbetween ($\rho^* = 0.5$).
The two other terms represent the way calcium concentration $c(t)$ controls plasticity. Indeed, it has been shown that increases in postsynaptic calcium concentration play a key role in long-term plasticity [97]. If $c(t) > \theta_p$, $\rho(t)$ tends to increase, and if $\theta_p > c(t) > \theta_d$, $\rho(t)$ tends to decrease (Θ

denotes the Heaviside function). θ_p and θ_d are respectively named the potentiation and depression thresholds. γ_p and γ_d are the rates of potentiation and depression. The last term is an activity-dependent noise term. Therefore, the model is a bistable model where calcium levels can induce switches between a low ($\rho = 0$) and a high efficacy state ($\rho = 1$).

The dynamics of calcium concentration $c(t)$ is determined by the pre and post spikes:

$$\frac{dc}{dt} = -\frac{c}{\tau_{\text{Ca}}} + C_{\text{pre}} \sum_i \delta(t - t_i - D) + C_{\text{post}} \sum_j \delta(t - t_j) \tag{1.16}$$

C_{pre} and C_{post} are the amplitudes of the calcium signals induced by the pre- and postsynaptic spikes, D is the delay between the presynaptic spike and its induced calcium response. In absence of stimulations, the calcium concentration decays exponentially with time constant τ_{Ca} (few milliseconds).

Analytical solution for transition probabilities: The probabilities that ρ will transition from an initial value ρ_0 towards 1 or 0 are denoted respectively U and D. With this stochastic model, their expressions are:

$$U(\rho_0) = \frac{1}{2}\left(1 + \text{erf}\left(-\frac{\rho_* - \bar{\rho} + (\bar{\rho} - \rho_0)e^{-nT/\tau_{\text{eff}}}}{\sqrt{\sigma_\rho^2(1 - e^{-2nT/\tau_{\text{eff}}})}}\right)\right) \tag{1.17}$$

$$D(\rho_0) = \frac{1}{2}\left(1 - \text{erf}\left(-\frac{\rho_* - \bar{\rho} + (\bar{\rho} - \rho_0)e^{-nT/\tau_{\text{eff}}}}{\sqrt{\sigma_\rho^2(1 - e^{-2nT/\tau_{\text{eff}}})}}\right)\right) \tag{1.18}$$

with τ_{eff} a characteristic time scale

$$\tau_{\text{eff}} = \frac{\tau}{\Gamma_p + \Gamma_d} \tag{1.19}$$

$\bar{\rho}$ and σ_ρ are respectively the average value and the standard deviation of ρ at the end of the whole process.

$$\bar{\rho} = \frac{\Gamma_p}{\Gamma_p + \Gamma_d} \tag{1.20}$$

$$\sigma_\rho^2 = \frac{\sigma^2(\alpha_p + \alpha_d)}{\Gamma_p + \Gamma_d} \tag{1.21}$$

and α_a, for $a = p$ or d, is the average fraction of time spent above a given threshold

$$\alpha_a = \frac{1}{nT}\int_0^{nT} \Theta[c(t) - \theta_a]dt \tag{1.22}$$

with $\Gamma_a = \gamma_a \alpha_a$.
These equations and analyses will be used in Chapter 2.

To conclude, this model explains the links between calcium signals induced by pre and post spikes timing and plasticity results. In particular, this framework has been applied to model STDP between corticostriatal and thalamostriatal synapses interactions [164].
The low complexity of the model and the possibility of mathematical predictions are interesting features that could be useful for modelling at a network level.

1.3 Networks

1.3.1 Overview

To obtain a model of what happens when individual cells are assembled into networks, one could gather the biophysical mechanisms in single cells and synapses to build realistic networks. However,

it would be too computationally expensive to integrate such biophysically detailed models as they are, as a large number of units have to be simulated. Therefore, the biological mechanisms at this lower scale are abstracted in simpler formulas, which are still thought to reproduce biologically realistic behaviours [152, 146].
The networks that have been most studied in computational neuroscience are neural networks, but networks with different unit cells are increasingly investigated. Indeed, as astrocytes also form interconnected networks (communicate through gap junctions) [94, 112], and neurons and astrocytes can interact (with neuro- and gliotransmitters) [73], large mixed neurons-astrocytes networks have started to be studied [181].
All in all, networks in computational neuroscience can differ with the cell types considered, the types of connections, the topology, and the equations that govern their individual behaviour.

As in the previous section, neural network models can be highly detailed or simplified to isolate key features, as in the well-known Hopfield network, an attractor model [111]. This neural network, similar to an Ising model, is typically used to model memory storage and recalling of patterns. In this model, each neuron i is in a state $S_i = \pm 1$ which evolves probabilistically according to the input potential $h_i(t)$,

$$\text{Prob}\{S_i(t + \Delta t) = +1 | h_i(t)\} = g(h_i(t)) \tag{1.23}$$

Where g is a gain function that bounds values between 0 and 1. The input potential $h_i(t)$ is itself dependent on the other neuron states $S_j(t)$:

$$h_i(t) = \sum_j w_{ij} S_j(t) \tag{1.24}$$

Where w_{ij} denotes the synaptic weight between neurons i and j.

The network can store and recall M memory patterns, which are fixed points of the dynamics. Their configurations are defined as $\{p_\mu^i = \pm 1; 1 \leq i \leq N\}$, for a pattern μ. If all neurons satisfy $S_i(t) = S_i(t + \Delta t) = p_i^\mu$, then the pattern μ is properly encoded. Synaptic weights are expressed as a function of these patterns:

$$w_{ij} = c \sum_{\mu=1}^{M} p_i^\mu p_j^\mu \tag{1.25}$$

with c a positive constant.
In this model, neuron states are thus binary. Below, we detail another well-known type of neural network, composed of integrate-and-fire neurons, which describes a little bit more the neural dynamics, while staying computationally and analytically accessible.

1.3.2 An example: integrate-and-fire networks

These simplified neuron models have been widely used in studies of neural coding, memory, and network dynamics [92]. They present the advantage to be easily fitted to experimental data.
In these models, whenever the membrane potential V_i exceeds a firing threshold V_{th}, a spike is produced, see figure 1.3. The membrane potential is then reset to a value V_r. In some integrate-and-fire models, a short refractory period in the dynamics is also added after a spike.

As an illustration, we focus here on a network composed of a simple form of integrate-and-fire neurons, leaky integrate-and-fire neurons, developed by Jercog et al. (2017) [116]. Despite the simplicity of the individual cells modelling, this network has been used to model complex oscillatory behaviours, like the Up-Down dynamics. This regime is characterized by the spontaneous alternation between periods of high collective activity (Up state) and periods of silence (Down state).
The model is constituted by N_E excitatory neurons and $N_I = N_E/4$ inhibitory neurons.

In this network, the membrane potential V_i^X of neuron i within the population X ($X = E$ for excitatory neurons and $X = I$ for inhibitory neurons) evolves according to

$$\tau_E \frac{dV_i^E(t)}{dt} = -(V_i^E(t) - V_L) + I_{rec,i}^E(t) + I_{ext,i}^E(t) - I_{a,i}(t) \tag{1.26}$$

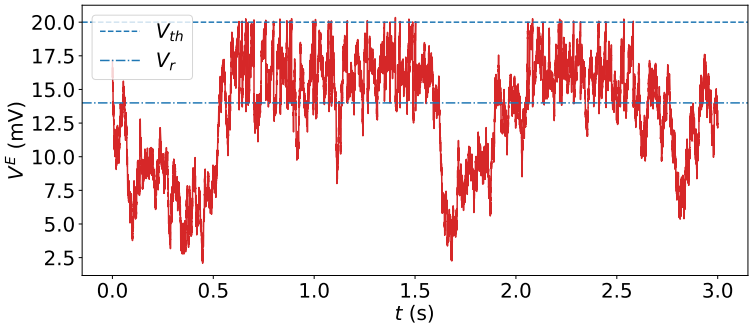

Figure 1.3: Illustration of a leaky integrate-and-fire neuron dynamics, adapted from Blum Moyse and Berry (2022) [29]. The membrane potential V^E of a neuron (here excitatory) in a network evolves as a function of time. Whenever the membrane potential crosses the firing threshold V_{th} (dashed line), a spike is emitted and the membrane potential is reset to V_r (dashdotted line).

$$\tau_I \frac{dV_i^I(t)}{dt} = -(V_i^I(t) - V_L) + I_{rec,i}^I(t) + I_{ext,i}^I(t) \tag{1.27}$$

with $i \in \{1, ..., N_X\}$. V_L is the leaky potential. $I_{ext,i}^I(t)$ is an external input, with in particular a gaussian white noise part $\sigma_X \sqrt{\tau_X} \eta_i(t)$. Where σ_X is the noise standard deviation and $\eta_i(t)$ is a random value with uniform distribution between 0 and 1. The synaptic current $I_{rec,i}^X(t)$ is defined by

$$I_{rec,i}^X(t) = J_{XE} s_E(t) + J_{XI} s_I(t) \tag{1.28}$$

where the synaptic variables s_X integrate the spikes or release events emitted by all the neurons in population X:

$$\tau_r^X \frac{du_X(t)}{dt} = -u_X(t) + \underline{\tau_X} \sum_k \sum_{j=1}^{N_X} \delta(t - t_j^k - d_j^k) \tag{1.29}$$

$$\tau_d^X \frac{ds_X(t)}{dt} = -s_X(t) + u_X(t) \tag{1.30}$$

with t_j^k the k^{th} spike (or release) time of cell j of population X, d_j^k its transmission delay (uniformly distributed between $d_{\min}^X$ and $d_{\max}^X$), and τ_r^X and τ_d^X the rise and decay times of the synapse, respectively. $\underline{\tau_X}$ is a normalizing time constant. Please note that there is a single variable s_X, which integers (through u_X) the spikes of all neurons of the population X. This model is thus an hybrid model between the single cell and the population scales.

In addition, the excitatory neurons displayed an after hyperpolarization current, which evolves according to

$$\tau_a \frac{dI_{a,i}(t)}{dt} = -I_{a,i}(t) + \beta \sum_k \delta(t - t_i^k) \tag{1.31}$$

This after hyperpolarization current is one of the possible mechanisms that could induce Up to Down transitions.

Stationary solutions and stability Analytical analyses of neural networks are most often carried out within the "mean-field" framework [74]. This approach can be applied to weakly coupled networks with regular firing [141], where the input received by a neuron is averaged. It can also be used for strongly coupled networks with irregular firing, where the fluctuations of the synaptic input are taken into account [38].

The second type of analysis can thus be applied to the model described above, which allows to find stable states (attractors) [141, 11]. In this approach, the stochastic equations (1.26) (1.27) can be expressed in terms of Fokker-Planck equations describing the temporal evolution of the neuron depolarization distribution $P^X(V^X, t)$ [45].

$$\tau_X \frac{\partial P^X}{\partial t}(V^X, t) = \frac{{\sigma_X}^2(t)}{2} \frac{\partial^2 P^X}{\partial {V^X}^2}(V^X, t) + \frac{\partial}{\partial V^X} \left[(V^X(t) - I_{rec}^X(t) - I_{ext}^X(t)) P^X(V^X, t) \right] \tag{1.32}$$

This equation is associated with the boundary conditions:

$$P^X(V_{th}, t) = 0 \tag{1.33}$$

$$\frac{\partial P^X}{\partial t}(V_{th}, t) = -\frac{2r_X(t)\tau_X}{{\sigma_X}^2(t)} \tag{1.34}$$

$$\frac{\partial P^X}{\partial t}(V_r^+, t) - \frac{\partial P^X}{\partial t}(V_r^-, t) = -\frac{2r_X(t)\tau_X}{{\sigma_X}^2(t)} \tag{1.35}$$

$$\lim_{V^X \to -\infty} P^X(V^X, t) = 0 \tag{1.36}$$

$$\lim_{V^X \to -\infty} V^X P(V^X, t) = 0 \tag{1.37}$$

Stationary solutions $P^X(V^X, t) = P_0^X(V^X)$ of equation (1.32) that respect the boundary conditions (1.33) to (1.37) are given by

$$P_0^X(V^X) = \frac{2r_{X,0}\tau_X}{\sigma_X} \exp\left(-\frac{(V^X - I_{X,0})^2}{\sigma_X^2}\right) \int_{\frac{V^X - I_{X,0}}{\sigma_X}}^{\frac{V_{th} - I_{X,0}}{\sigma_X}} \Theta\left(u - \frac{V_r - I_{X,0}}{\sigma_X}\right) e^{u^2} du \tag{1.38}$$

Applying the normalization condition for a probability distribution

$$\int_{-\infty}^{V_{th}} P_0^X(V^X) dV^X = 1 \tag{1.39}$$

to equation (1.38) gives the self-consistent (nullclines) mean-field equations for the equilibrium firing rates ($r_{X,0}$) [38]:

$$r_{X,0} = \frac{1}{\tau_X} \left[\int_0^\infty \frac{dy}{y} e^{-y^2} (e^{2yy_t^X} - e^{2yy_r^X})\right]^{-1} \tag{1.40}$$

with

$$y_r^X = \frac{V_r - I_{X,0}}{\sigma_X} \qquad y_t^X = \frac{V_{th} - I_{X,0}}{\sigma_X} \tag{1.41}$$

and with the currents:

$$I_{E,0} = V_{L,E} + N_E J_{EE} r_{E,0} \underline{\tau_E} + N_I J_{EI} r_{I,0} \underline{\tau_I} + I_a \tag{1.42}$$

$$I_{I,0} = V_{L,I} + N_E J_{IE} r_{E,0} \underline{\tau_E} + N_I J_{II} r_{I,0} \underline{\tau_I} \tag{1.43}$$

The stability of these solutions can be determined using linear perturbation analysis [141, 197]. For that purpose, a small perturbation $\delta r_X e^{\lambda t}$ to the equilibrium firing rate is introduced, such as

$$r_X = r_{X0} + \delta r_X e^{\lambda t} \tag{1.44}$$

the corresponding perturbation of the synaptic variable s_X is computed as

$$\delta s_Y = S_Y(\lambda) \delta r_Y(t) e^{\lambda t} \tag{1.45}$$

with the synaptic response function

$$S_Y(\lambda) = \frac{e^{-\lambda d^Y}}{(1 + \lambda \tau_r^Y)(1 + \lambda \tau_d^Y)} \tag{1.46}$$

Finally, δr_X can be computed as

$$\delta r_X = R_X(\lambda) \delta I_X(t) e^{\lambda t} \tag{1.47}$$

with

$$\delta I_X(t) = J_{XE} \delta s_E(t) - J_{XI} \delta s_I(t) \tag{1.48}$$

The neuronal response function $R_X(\lambda)$ is defined by:

$$R_X(\lambda) = \frac{r_{X,0}}{\sigma_X(1+\lambda\tau_X)} \frac{\frac{\partial U}{\partial y}(y_t^X, \lambda\tau_X) - \frac{\partial U}{\partial y}(y_r^X, \lambda\tau_X)}{U(y_t^X, \lambda\tau_X) - U(y_r^X, \lambda\tau_X)} \tag{1.49}$$

with

$$U(y,\lambda) = \frac{e^{y^2}}{\Gamma\left[\frac{1+\lambda}{2}\right]} M\left(\frac{1-\lambda}{2}, \frac{1}{2}, -y^2\right) + \frac{2ye^{y^2}}{\Gamma\left[\frac{\lambda}{2}\right]} M\left(1-\frac{\lambda}{2}, \frac{3}{2}, -y^2\right) \tag{1.50}$$

Where M is a confluent hypergeometric function.

After solving equation (1.47) for δr_X, we find the eigenvalue equation:

$$F_{EE}(\lambda)(1+F_{II}(\lambda)) - F_{II}(\lambda) - F_{EI}(\lambda)F_{IE}(\lambda) = 1 \tag{1.51}$$

with

$$F_{XY}(\lambda) = J_{XY} R_X(\lambda) S_Y(\lambda) \tag{1.52}$$

The eigenvalues λ are found by solving equation (1.51) numerically.

The equilirium firing rates are stable when all the corresponding eigenvalues have negative real parts. If at least one eigenvalue has a positive real part, the system is unstable.
These equations and analyses will be used in Chapter 3.

We have seen with this "mean-field" analysis, that it is possible to study a high-dimensional stochastic network by averaging over its degrees of freedom, so that the understanding is made easier. Thus, at an higher abstraction scale, other models similarly consider a continuum limit to model large networks.

1.4 Spatial continuum

1.4.1 Overview

At many locations in the brain, one can consider that large groups of cells display similar features at least approximately. These properties make it relevant to describe these populations with a mean activity rather than the detailed spike trains of each neuron. For instance, the Kuramoto model is used to approximate the dynamics of a population of N neurons with phase oscillators [136].
For that purpose, the description of neural activity is considered in the spatial continuum limit.

This consideration began with a characterization of the proportion of activated neurons per unit of time for a given volume. It was used to model the way large scale brain activity is initiated and propagated [26]. This work has then been extended [99], and in 1972 the so-called neural rate models were introduced by Wilson and Cowan [239, 240]. These models describe the activity dynamics in large homogeneous groups of spiking neurons, and are named rate models, neural masses, or theories of population dynamics.

Still in the 1970s, the neural field framework was introduced, in particular by Wilson and Cowan [239, 240], Nunez [178] and Amari [9]. These equations model the spatiotemporal evolution of coarse-grained variables such as the synaptic or firing rate activity in large neural populations [51]. These models can display different dynamics, such as periodic patterns (spatially and temporally) [70], localised areas of activity named bumps [128], travelling waves [72], spatiotemporal canards [15] and so on. These models have been used to investigate a wide range of neural mechanisms, such as short-term memory processes [137], visual hallucinations [34], or EEG rhythms [117].

1.4.2 Examples: a firing rate and a neural field model

1.4.2.1 A firing rate model with adaptation

We here detail the rate equations developed in [116, 197], that express as a firing rate model the spiking network situation of the subsection 1.3.2 for interacting excitatory (E) and inhibitory (I)

neural populations. This model describes r_X, the firing rate of the population X averaged over the neurons in X, as a function of time. r_E is the average rate of the excitatory neurons population and r_I is the average rate of the excitatory neurons population, their evolutions are defined by:

$$\tau_E \frac{dr_E}{dt} = -r_E(t) + \phi_E(I_E(t) - a(t) + \sigma\xi_E(t)) \tag{1.53}$$

and

$$\tau_I \frac{dr_I}{dt} = -r_I(t) + \phi_I(I_I(t) + \sigma\xi_I(t)) \tag{1.54}$$

where τ_X is the time constant of population X, the final term $\sigma\xi_X(t)$ describes a Ornstein-Uhlenbeck process with zero mean and standard deviation σ. ϕ is the transfer function:

$$\phi_X(x) = g_X[x - \theta_X]_+ \tag{1.55}$$

with rectification $[z]_+ = z$ if $z > 0$ and 0 otherwise.

$I_X(t)$ is a recurrent input defined as:

$$I_X(t) = J_{XE} r_E(t) + J_{XI} r_I(t) \tag{1.56}$$

The synaptic couplings J_{XY} describe the strength of the connection from population Y to X. They verify $J_{XE} > 0$ (excitatory), $J_{XI} < 0$ (inhibitory).

The dynamics of the adaptation current $a(t)$ (the rate equivalent of the after hyperpolarization current in equation (1.31) of the spiking network model) is given by:

$$\tau_a \frac{da}{dt} = -a(t) + \beta r_E(t) \tag{1.57}$$

Fixed points and stability With the external noisy input $\sigma\xi_X(t)$ neglected, and in the case where rates evolve much faster than the adaptation, the E and I nullclines of equations (1.53) (1.54) are defined as the points where $\frac{dr_E}{dt} = 0$ and $\frac{dr_I}{dt} = 0$:

$$r_{E0} = g_E[J_{EE} r_{E0} - J_{EI} r_I - a_0 - \theta_E]_+ \tag{1.58}$$

$$r_{I0} = g_I[J_{IE} r_{E0} - J_{II} r_{I0} - \theta_I]_+ \tag{1.59}$$

with

$$a_0 = \beta r_{E0} \tag{1.60}$$

The intersection of the nullclines define the fixed points r_{E0} and r_{I0}.

The stability of these fixed points can be determined by linearization of the dynamics. It is possible to study it by adding a small perturbation to the equilibrium firing rate, $r_X = r_{X0} + \delta r_X e^{\lambda t}$ and to compute the eigenvalues λ of the system by solving the resulting equations at first order in δr_X s. Formally, this boils down to compute the Jacobian matrix J of the system at the fixed points. Indeed, with $\vec{\delta r} = \begin{pmatrix} r_E - r_{E0} \\ r_I - r_{I0} \end{pmatrix}$, we have after the linearization:

$$\frac{d\vec{\delta r}}{dt} = J\vec{\delta r} \tag{1.61}$$

with

$$J = \begin{pmatrix} \frac{\partial G_E}{\partial r_E}(r_{E0}, r_{I0}) & \frac{\partial G_E}{\partial r_I}(r_{E0}, r_{I0}) \\ \frac{\partial G_I}{\partial r_E}(r_{E0}, r_{I0}) & \frac{\partial G_I}{\partial r_I}(r_{E0}, r_{I0}) \end{pmatrix} \tag{1.62}$$

with G_E, G_I the right-hand-sides of respectively the (1.53) and (1.54) equations.

To find the eigenvalues λ one solves equation (1.61) and get $\vec{\delta r} = \epsilon e^{\lambda t}$. Solving for λ can be done by solving the characteristic equation of J, $|J - \lambda I| = 0$, where I is the identity matrix.

The equilirium firing rates are stable when all the corresponding eigenvalues have negative real parts. If at least one eigenvalue has a positive real part, the system is unstable.
These equations and analyses will be used in Chapter 3.

1.4.2.2 A neural field with synaptic depression and smooth firing response

A neural field model introduces the space dimension with a space-dependent function $w(x-y)$ which defines the connectivity between two neurons at locations x and y. We then focus on a bump study in a piecewise smooth neural field with synaptic depression, developed by Kilpatrick and Bressloff (2010) [126, 127]. The equation of the neural field representing the local activity of a population of neurons at position x and time t, $u(x,t)$, is given by:

$$\tau \frac{\partial u}{\partial t}(x,t) = -u(x,t) + \int_{-\infty}^{\infty} dy w(x-y) q(y,t) f(u(y,t) - \kappa) \tag{1.63}$$

τ is the membrane time constant. The second term on the right-hand side is the synaptic input, where f is the firing rate function, and κ the firing rate threshold. The synaptic weights between neurons at positions x and y is denoted by $w(x-y)$. In the classic equation of neural fields, $q(y,t) = 1$ and the firing rate function f is a heaviside function. In Kilpatrick and Bressloff (2010) [126, 127], the authors study a smooth firing rate function, and introduce synaptic depression.

Indeed, the factor $q(x,t)$ represents a fraction of available presynaptic resources, which evolves according to

$$\frac{\partial q}{\partial t}(x,t) = \frac{1 - q(x,t)}{\alpha} - \beta q(x,t) f(u(x,t) - \kappa) \tag{1.64}$$

Here, synaptic resources reduce at a rate βf, and recover with the timescale α.

With f defined as a heaviside function Θ, a stationary bump solution $(U(x), Q(x))$ can be defined in the activated area $R[U] = (-a, a)$, with a the half-width of the bump.

$$U(x) = \int_{-a}^{a} Q(y) w(x-y) dy \tag{1.65}$$

$$Q(x) = 1 - \frac{\alpha\beta}{1+\alpha\beta} \Theta(U(x) - \kappa) \tag{1.66}$$

See figure 1.4 (A) for a plot of a bump profile with the so-called mexican hat kernel, $w(x-y) = e^{-|x-y|} - Ae^{-|x-y|/\sigma}$. The bump boundary conditions can be written as

$$U(\pm a) = \kappa \tag{1.67}$$

Because of the discontinuity in $Q(x)$, see figure 1.4 (A), the local stability cannot be easily determined with a linearization of the Heaviside function in equations (1.63) (1.64). A regular method in neural field analysis is to compute the associated Evans function, but here this approach has been shown to improperly evaluate the stability domains [127]. Thus, linear stability analysis is here carried out by adding a small perturbation to the bump, which would shift the bump boundaries.

Concretely, the variables $u(x,t)$ and $q(x,t)$ can be written as $u(x,t) = U(x) + \epsilon\psi(x,t)$ and $q(x,t) = Q(x) + \epsilon\phi(x,t)$ in equations (1.63) (1.64) (for $\epsilon \ll 1$), which gives:

$$\begin{aligned} \frac{\partial \psi(x,t)}{\partial t} = -\psi(x,t) + \frac{1}{\epsilon} \int_{-\infty}^{\infty} w(x-y) Q(y) \left[\Theta(U(y) + \epsilon\psi(y,t) - \kappa) - \Theta(U(y) - \kappa)\right] dy \\ + \int_{-\infty}^{\infty} w(x-y) \phi(y,t) \Theta(U(y) + \epsilon\psi(y,t) - \kappa) dy \end{aligned} \tag{1.68}$$

$$\begin{aligned} \frac{\partial \phi(x,t)}{\partial t} = -\frac{\phi(t)}{\alpha} - \frac{\beta}{\epsilon} Q(x) \left[\Theta(U(x) + \epsilon\psi(x,t) - \kappa) - \Theta(U(x) - \kappa)\right] \\ - \beta\phi(x,t) \Theta(U(x) + \epsilon\psi(x,t) - \kappa) \end{aligned} \tag{1.69}$$

The perturbations of the bump boundary $\epsilon\Delta_{\pm}(t)$ are written in the threshold conditions

$$u(a+\epsilon\Delta_+(t),t)=\kappa=u(-a+\epsilon\Delta_-(t),t) \tag{1.70}$$

After expansion to first order in ϵ in equation (1.70) and identification with the expression $u(x,t)=U(x)+\epsilon\psi(x,t)$, it is found that $\Delta_\pm\approx\pm\psi(\pm a,t)/|U'(a)|$.

To smooth out the discontinuities in equations (1.68) and (1.69), the field $\Phi(x,t)$ can be introduced [127],

$$\Phi(x,t)=\int_{-a+\epsilon\Delta_+}^{a+\epsilon\Delta_-}w(x-y)\phi(y,t)dy \tag{1.71}$$

Then $\psi(x,t)$ and $\Phi(x,t)$ are written in a separable form as $\psi(x,t)=\psi(x)e^{\lambda t}$ and $\Phi(x,t)=\Phi(x)e^{\lambda t}$. Here to ensure the fact $\Phi(\pm a,t)$ sign is constant, λ must be real. Then the resulting equation is solved for $\Phi(x)$, which gives the eigenvalue equation

$$\begin{aligned}(\lambda+1)\psi(x)=&\gamma w(x+a)\psi(-a)G(\psi(-a))\left(1-\frac{\beta\Theta(\psi(-a))}{\lambda+\alpha^{-1}+\beta}\right)\\&+\gamma w(x-a)\psi(a)G(\psi(a))\left(1-\frac{\beta\Theta(\psi(a))}{\lambda+\alpha^{-1}+\beta}\right)\end{aligned} \tag{1.72}$$

With $\gamma^{-1}=|U'(\pm a)|$ and

$$G(X)=\begin{cases}1 \text{ if } X>0\\(1+\alpha\beta)^{-1} \text{ if } X<0\end{cases} \tag{1.73}$$

The discrete eigenvalues spectrum can be found by considering $x=\pm a$ and fixing the signs of $\psi(\pm a)$. This leads to three cases, see figure 1.4 (C): (Left) $\psi(\pm a)$ opposite signs (shifts), (Middle) $\psi(\pm a)>0$ (expansions), and (Right) $\psi(\pm a)<0$ (contractions). The exact results for λ are not detailed here, but the stability domains are shown in figure 1.4 (B) for the so-called mexican hat kernel. However we should keep in mind that since this analysis is based on real eigenvalues only, these results are only sufficient conditions for the bump's instability.

A similar analysis can be studied with spike frequency adaptation [126, 127] . This process corresponds to an adaptation current increase, and can be implemented in the neural field model by introducing a dynamic threshold $\kappa(x,t)$ into the firing rate function:

$$\tau\frac{\partial u}{\partial t}(x,t)=-u(x,t)+\int_{-\infty}^{\infty}dyw(x-y)f(u(y,t)-\kappa(y,t)) \tag{1.74}$$

$$\frac{\partial\kappa}{\partial t}(x,t)=-(\kappa(x,t)-\kappa_0)+\eta f(u(x,t)-\theta) \tag{1.75}$$

Here, when $u(x,t)$ is above the parameter θ, the threshold $\kappa(x,t)$ increases from its initial value κ_0 to $\kappa_0+\eta$. These equations and analyses for synaptic depression and spike frequency adaptation will be used in Chapter 4.

1.5 Conclusion

This introduction aimed at displaying a rapid overview of the modelling approaches in computational neuroscience at different spatial levels of abstraction: single-cell and synapse, network and continuum limit. Figure 1.1 summarizes the main methods presented in this chapter by order of level of abstraction. I have focused during this thesis on models which allowed mathematical analyses, by personal choice.
A more in depth attention was paid to models that have been used and further developed during this thesis: the calcium-based spike-timing-dependent plasticity (chapter 2), the leaky integrate-and-fire network (chapter 3), the rate (chapter 3) and neural field with adaptation (chapter 4) models. The following chapters will present the different projects of the thesis, organized following this increasing level of spatial abstraction.

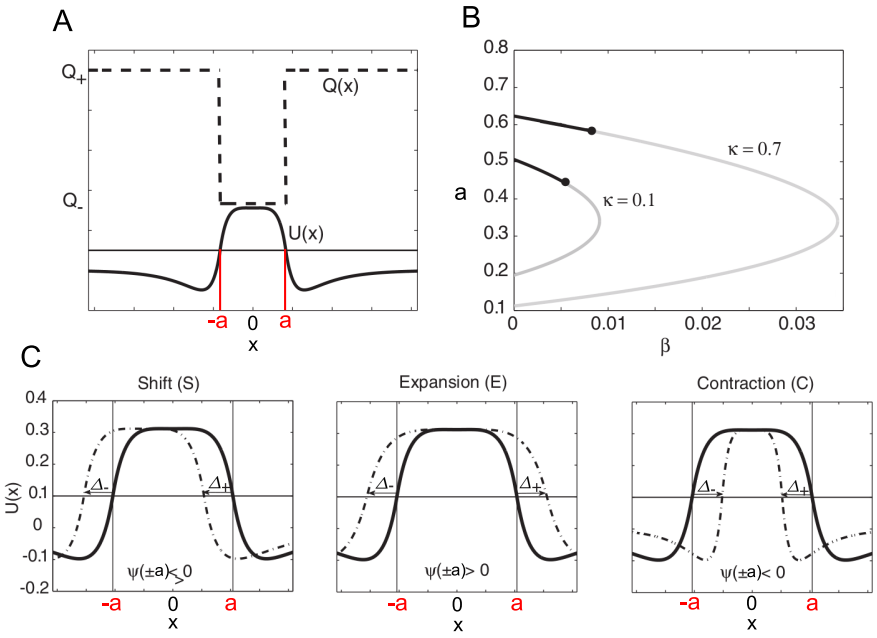

Figure 1.4: Stationary bump and stability analysis in a network with synaptic depression, adapted from Bressloff (2012) [33]. A mexican hat connectivity kernel has been used for $w(x-y)$. **(A)** Bump stationary solution of width $2a$ centered around 0, $U(x)$ is represented with a solid curve and $Q(x)$ with a dashed line. **(B)** Plots for different values of κ, presenting the bump width a as a function of β, the amplitude of synaptic depression. These curves were determined using equation (1.67). Unstable domains (gray lines) are determined by the piecewise smooth stability method presented above. Numerically stable bump domains are represented with a solid line. **(C)** Schemas of a shift (Left), expansion (Middle) and contraction (Right) perturbation.

Chapter 2

A model for input-timing-dependent plasticity

2.1 Experimental context to study corticostriatal and thalamostriatal plasticities

2.1.1 From STDP to ITDP

The basal ganglia are a group of subcortical nuclei in the brains of vertebrates. They are strongly connected with the cerebral cortex, the thalamus, and the limbic system. Basal ganglia are implicated in the detection of external signals and the establishment of suitable behaviours through motivation and reward. In particular, cortex-thalamus-basal ganglia loops play a key role in the adaptive control of behavior and in procedural learning [243]. This latter refers to the ability to acquire motor and cognitive skills progressively and automatically [134]. The main input nucleus of the basal ganglia, the striatum, integrates glutamatergic signals from the cerebral cortical and thalamic nuclei, then transfers the information to the basal ganglia's output areas. The striatal-projecting neurons (the medium-sized spiny neurons, MSNs) play the role of similarity sensors between patterns of cortical and thalamic activity [67]. MSNs are contacted by cortical afferents on dendritic spines, and by thalamic afferents on dendritic shafts [214].

The neurobiological mechanisms of this integration process remain largely undetermined. To characterize them, researchers Marie Vandecasteele, Elodie Perrin, Nicolas Gervasi and Laurent Venance (CIRB, Collège de France, Paris) investigated the plasticity rules at the corticostriatal (CS) and thalamostriatal (TS) synapses and how they combined on their striatal target, the MSNs.
Indeed, CS long-term plasticity is a fundamental mechanism to form habits based on goal-directed behaviours [244, 187]. To better characterize the implication of the striatum and thalamus in procedural learning, it is fundamental to understand TS plasticity, which has been less studied than CS plasticity, and the interactions between the two synaptic processes.

A paper published by the Venance group (Mendes et al. (2020) [164]) analyzed the spike-timing-dependent plasticity, STDP (see the general introduction chapter 1), at both the CS and TS synapses. They investigated the CS and TS synaptic plasticity and their interactions at a single neuron level with patch-clamp recordings, with a brain slice preparation. They also developed a calcium-based mathematical model of the coupled CS and TS plasticity that is derived from the Graupner and Brunel STDP model [98] presented in subsection 1.2.2. Their findings pointed out the key role of precise timing in cortical and thalamic activity for the memory engram of striatal synapses. Thalamic inputs would have an important influence on the CS plasticity map, in particular they could induce LTD in CS-STDP plasticity [164], and might play a role in enabling flexible behaviour for procedural learning.

Although the STDP is a Hebbian learning rule mimicking physiological realities, the naturalistic

validity of this protocol has been questioned [149, 150]. For instance, the injection of somatic current that is used to generate postsynaptic spikes does not mimic any physiological event. STDP is a good experimental paradigm to study Hebbian plasticity, but it would be interesting to develop more physiological protocols.

Contrary to STDP which requires the injection of current to the postsynaptic neuron, in ITDP experiments the postsynaptic neuron is not directly manipulated since only the synaptic inputs are stimulated and induce sub- or suprathreshold responses [144], see figure 2.1 (B). The temporal correlation of afferent inputs determines the plasticity in ITDP. Thalamic (t_{TS}) and cortical (t_{CS}) stimulations are separated by a delay Δt. We define this delay as $\Delta t = t_{\mathrm{TS}} - t_{\mathrm{CS}}$.
Typically $|\Delta t| = 15$ ms, and for each experiment, pairings were repeated 100 times with a 1 Hz frequency.

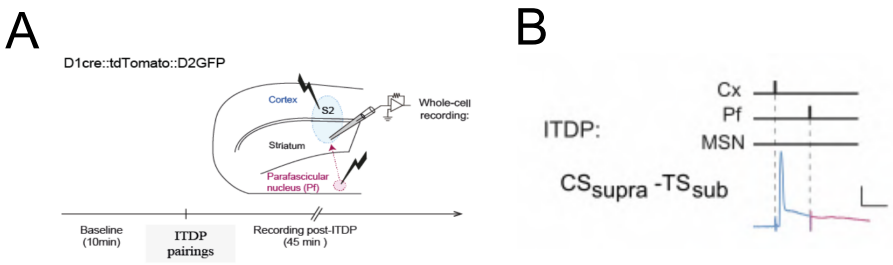

Figure 2.1: ITDP protocol for corticostriatal (CS) and thalamostriatal (TS) synaptic plasticities, adapted from Perrin (2022) [186]. **(A)** Schema of the brain slice with the positions of stimulating electrodes: the secondary somatosensory cortex (S2) and the parafascicular nucleus of the thalamus (Pf). The recording location is the dorsolateral striatum. After baseline stimulations, the ITDP protocol is applied, then CS and TS changes are recorded during 50 mn. **(B)** An example of an ITDP protocol, here a "CS supra then TS sub" protocol. The cortical stimulation happens before the thalamic stimulation. The resulting striatal excitatory postsynaptic potential (EPSP) is represented below. In all other cases stimulations can also be suprathreshold (supra) or subthreshold (sub), spaced with $|\Delta t| = 15$ ms. For each experiment, pairings were repeated 100 times with a 1 Hz frequency.

2.1.2 ITDP experiments

During her thesis, Elodie Perrin carried out ITDP experiments at corticostriatal and thalamostriatal synapses for 16 conditions, see figure 2.1 (A). Indeed stimulations can be suprathreshold (supra) or subthreshold (sub), TS then CS ($\Delta t < 0$) or CS then TS ($\Delta t > 0$), spaced with $|\Delta t| = 15$ ms or $|\Delta t| = 100$ ms (control). These experiments allowed to better understand the interplay of these two plasticities. Their results indicating the plasticity modifications (LTP, LTD, or nothing) are summarized in figure 2.2.

As mathematical models were created for STDP (see the general introduction chapter 1), we developed a model for ITDP based on similar principles. Computational modelling would allow to better grasp the underlying neurobiological mechanisms, but also it could help predict plasticity evolutions in other experiments where plasticity measurements cannot be achieved, such as in vivo experiments. Indeed after the fit of our model on ex vivo ITDP data, we try to apply it to behavioural experiments on mice carried out by Marie Vandecasteele, where only cortical and thalamic spike trains were accessible.

2.1.3 Motor training and motor adaptation effects

Another experiment was carried out to study CS and TS plasticities during a motor adaptation task. The protocol consisted in training mice on a motor task, which is walking back and forth on a regular horizontal scale, for 10 days. The 11th day, the scale was changed to a scale with missing

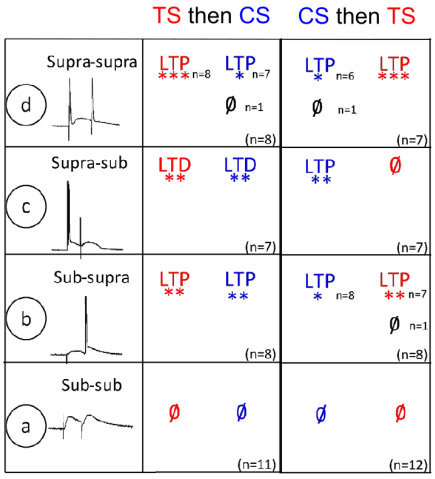

Figure 2.2: Experimental results of the ITDP experiments, for the D1 (part of the striatum) MSNs neurons. CS and TS synapses can be either potentiated (LTP), depressed (LTD) or do not change (Ø). These data will be used to fit the parameters of our computational model.

bars, see figure 2.3. During these motor tasks, local field potential (LFP) signals in cortical and thalamic neurons were recorded. The LFP corresponds to the electric potential in the extracellular space around neurons, recorded with electrodes [64]. From that signal, it is possible to infer action potentials emitted by the neurons surrounding locally the recording electrodes, through spike sorting algorithms [6, 37] Our role would be then to determine whether LTP, LTD, or nothing is expected to happen with such recorded spike trains as inputs in our fitted model, since the synaptic weight measurements cannot be achieved in vivo, but only ex vivo or in vitro.

The final purpose of these experiments is to determine the functional role of each input to the MSNs (cortical or thalamic) in learning. For instance, thalamocortical synapses have been hypothesized as sending "reset" messages when the animal encounters a situation not according to the learned task [166, 30].

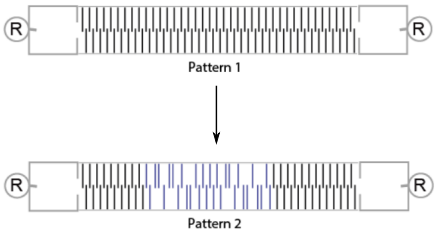

Figure 2.3: Experimental setup of the horizontal scale experiment, to study CS and TS plasticities in a motor adaptation task, adapted from Perrin (2022) [186]. First, mice are trained with the first pattern during 10 days (30 passages each day). Then, the 11th day after 5 passages on the first scale pattern, the second pattern is used for 5 passages. During these tasks, LFP signals in the cortex and in the thalamus are recorded.

Two types of data were given to us:

- A LFP signal with 2 channels, downsampled at 1.25 kHz
- Spike trains, 3 from the cortex and 4 from the thalamus. They were extracted from the "total" LFP signal with 2×32 channels at 20 kHz.

For now, this experiment is not finished and future more precise recordings will be carried out. In this chapter we analyzed the first experimental samples we have.

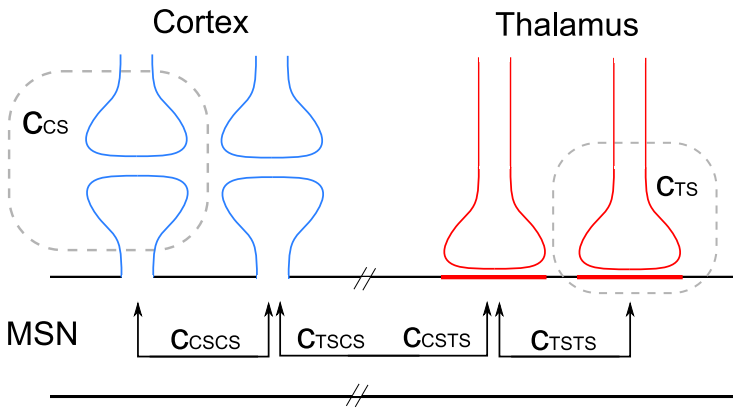

Figure 2.4: Schematic representation of the two-compartment (CS and TS) model, inspired by a schema in Mendes et al. (2020) [164]. MSNs are contacted by cortical afferents on dendritic spines, and by thalamic afferents on dendritic shafts. The total calcium concentration is a result of the different contributions c_X, c_{XX} and c_{XY}.

2.2 Presentation of the model and data analysis methods

2.2.1 Computational model of ITDP fitted with experimental data

The model is inspired by STDP models from Graupner and Brunel (2012) [98] and from Mendes et al. (2020) [164], with the differences mentioned above which characterize ITDP. Figure 2.4 presents schematically the main elements of the model.

Each type of synapse (CS and TS) has a synaptic efficacy $\rho_{X_i}(t)$, where $X = \{\mathrm{CS}, \mathrm{TS}\}$ and $i \in \{1, ..., n\}$ with n the number of synapses of a given compartment (CS or TS). ρ_{X_i} has two stable states, up or down, and one unstable. Switches occur between these states according to the fluctuations of the total concentration of calcium ions $c_X^{\mathrm{tot}}(t)$. Mathematically, $\rho_{X_i}(t)$ is assumed to satisfy the stochastic differential equation derived from Graupner and Brunel (2012) [98]:

$$\begin{aligned}\tau_X d\rho_{X_i} = [-\rho_{X_i}(1-\rho_{X_i})(\rho_X^* - \rho_{X_i}) + \gamma_{p_X}(1-\rho_{X_i})\Theta(c_X^{\mathrm{tot}}(t) - \theta_{p_X}) \\ - \gamma_{d_X}\rho_{X_i}\Theta(c_X^{\mathrm{tot}}(t) - \theta_{d_X})]dt + dN_{X_i}(t)\end{aligned} \tag{2.1}$$

The t dependency of ρ have not been noted in the equation for an easier comprehension.
τ_X denotes the typical time of the synaptic efficacy evolution, the parameter ρ_X^* denotes the switching point between those trajectories eventually converging to the upstate ($\rho_{X_i} > \rho_X^*$) and those converging to the downstate ($\rho_{X_i} < \rho_X^*$).

When calcium concentration exceeds the potentiation threshold θ_{p_X}, ρ_{X_i} increases at a rate denoted γ_{p_X}. Similarly, depression steps in when $c_X^{\mathrm{tot}}(t)$ exceeds a threshold θ_{d_X} and contributes to reduce the synaptic efficacy at rate γ_{d_X}.

Finally the term $dN_X(t)$ is assumed to be a calcium-dependent Gaussian noise. It is defined, with $\eta_{X_i}(t)$ a Gaussian white noise, by:

$$dN_{X_i}(t) = \sigma_X\sqrt{\tau_X}\sqrt{\Theta(c_X(t) - \theta_{p_X}) + \Theta(c_X(t) - \theta_{d_X})}\eta_{X_i}(t) \tag{2.2}$$

The total change in synaptic strength W_X was estimated from the proportion U and D of synapses that are respectively potentiated (from stable state 0 to 1) and depressed (from stable state 1 to 0) after ITDP.

$$W_X\left(\frac{1-D}{1-U}\right) = a + \frac{b}{1 + e^{-s\left(\frac{1-D}{1-U} - d\right)}} \tag{2.3}$$

with $d = \frac{1}{s}\log\left(\frac{\Delta - e^s}{1-\Delta}\right)$, $b = (\text{LTP} - \text{LTD})(1 + e^{-sd})$, $a = \text{LTP} - b$ and $\Delta = \frac{\text{LTP}-\text{LTD}}{\text{LTP}-1}$, where LTD represents the maximal depression, LTP represents the maximal potentiation, and s is a parameter controlling the sensitivity of synaptic changes.

There are four cases depending on whether CS and TS stimulations are subthresholds (sub) or suprathresholds (supra).
In case of two sub stimulations, to reproduce the sublinear EPSP summation, c_X^{tot} is modeled as a quadratic sum: $c_X^{\text{tot}} = \sqrt{c_X^2 + c_{XX}^2 + c_{XY}^2}$. In case of two supra stimulations: $c_X^{\text{tot}} = c_X + c_{XX} + c_{XY}$. If the X stimulation is supra and the Y stimulation is sub: $c_X^{\text{tot}} = c_X + c_{XX} + c_{XY}$. Finally if the X stimulation is sub and the Y stimulation is supra: $c_X^{\text{tot}} = \sqrt{c_X^2 + c_{XX}^2} + c_{XY}$.

where c_X is the amplitude of the calcium peaks after an external spike on a synapse of a X compartment,

$$\frac{dc_X}{dt} = -\frac{1}{\tau_{Ca_X}} c_X + C_X \sum_{k=1}^{K} \delta(t - t_X^k - D_X) \tag{2.4}$$

c_{XX} is the amplitude of the calcium peaks after an external spike on another synapse of a X compartment,

$$\frac{dc_{XX}}{dt} = -\frac{1}{\tau_{Ca_X}} c_{XX} + C_{XX} \sum_{k=1}^{K} \delta(t - t_X^k - D_X - D_{XX}) \tag{2.5}$$

and with c_{XY}, the amplitude of the calcium peaks after an external spike on another synapse of a Y compartment,

$$\frac{dc_{XY}}{dt} = -\frac{1}{\tau_{Ca_Y}} c_{XY} + C_{XY} \sum_{k=1}^{K} \delta(t - t_X^k - D_Y - D_{XY}) \tag{2.6}$$

If a stimulation is suprathreshold, $C_X = C_X^{\text{supra}}$, otherwise if the stimulation is subthreshold, $C_X = C_X^{\text{sub}}$. Same variations apply for C_{XX} and C_{XY} amplitudes.
Please note that each synapse has a different synaptic efficacy ρ_{X_i}, due to different initial conditions.

The former equations can be solved,

$$c_X(t) = C_X \exp\left(-\frac{t - t_X^0 - D_X}{\tau_{\text{Ca}_X}}\right) \tag{2.7}$$

if $t - t_X^0 - D_X > 0$, $c_X(t) = 0$ otherwise. Similar formulas apply for C_{XX} (with $D_X + D_{XX}$) and C_{XY} (with $D_Y + D_{XY}$).

We find the analytical transition probabilities formulas in Graupner and Brunel (2012) [98] supplementary materials, presented in introduction (equations (1.17) to (1.22)). The equations adapted to our model are:

$$U(\rho_{X_0}) = \frac{1}{2}\left(1 + \text{erf}\left(-\frac{\rho_{X_*} - \overline{\rho_X} + (\overline{\rho_X} - \rho_{X_0})e^{-nT/\tau_{X_{\text{eff}}}}}{\sqrt{\sigma_\rho^2(1 - e^{-2nT/\tau_{X_{\text{eff}}}})}}\right)\right) \tag{2.8}$$

$$D(\rho_{X_0}) = \frac{1}{2}\left(1 - \text{erf}\left(-\frac{\rho_{X_*} - \overline{\rho_X} + (\overline{\rho_X} - \rho_{X_0})e^{-nT/\tau_{X_{\text{eff}}}}}{\sqrt{\sigma_{\rho_X}^2(1 - e^{-2nT/\tau_{X_{\text{eff}}}})}}\right)\right) \tag{2.9}$$

with

$$\overline{\rho_X} = \frac{\Gamma_{X_p}}{\Gamma_{X_p} + \Gamma_{X_d}} \tag{2.10}$$

$$\sigma_{\rho_X}^2 = \frac{\sigma^2(\alpha_{X_p} + \alpha_{X_d})}{\Gamma_{X_p} + \Gamma_{X_d}} \tag{2.11}$$

$$\tau_{X_{\text{eff}}} = \frac{\tau}{\Gamma_{X_p} + \Gamma_{X_d}} \tag{2.12}$$

$\Gamma_{X_a} = \gamma_{X_a} \alpha_{X_a}$, with a=p or d.

$$\alpha_{X_a} = \frac{1}{nT} \int_0^{nT} \Theta[c_X^{\text{tot}} - \theta_a] dt \tag{2.13}$$

Thanks to these analytical transition probabilities, we can estimate our parameters in a much faster way than with the total numerical simulation. We adjusted our model with experimental results of ITDP experiments provided by Laurent Venance and Nicolas Gervasi, thanks to a Covariance Matrix Adaptation Evolutionary Strategy (CMA-ES) algorithm [1]. This algorithm is used for derivative-free global optimization (see pygmo online documentation [2]). The resulting parameters are presented in table 2.1. Once we get the parameters, we used them in the numerical simulation for 20 synapses (equations (2.1) to (2.6)). Results are presented in figure 2.7.

2.2.2 Motor task experiment recordings analysis, to determine for each cortical or thalamic spike if it is associated with a sub- or suprathreshold MSN response

The LFP signals are recorded either from S2 (cortex) or from Pf (thalamus), two areas that send inputs to the striatum. To use the in vivo extracted cortical and thalamic spike trains as inputs in our model (to infer in vivo CS and TS plasticities), the type of induced MSN response (sub or supra) must be determined for each spike.
For that purpose, it is necessary to localize when many cortical or thalamic neurons spike at the same time. Indeed, a large input of collective firing is needed to induce a suprathreshold response in MSNs, see figure 2.5. Striatal and cortical recordings in Mahon (2001) [154] show that MSN firing can occur with the largest EPSPs, which were systematically coincident with large amplitude electroencephalography (EEG) patterns (spindle waves) in the cortex. A similar reasoning can be applied to the LFP signals in the experiment of Perrin.
Therefore, the analysis of the LFP signal could determine if there is an oscillatory behaviour at a particular frequency correlated with spikes emission. Then, the signal could be filtered to only get that frequency.

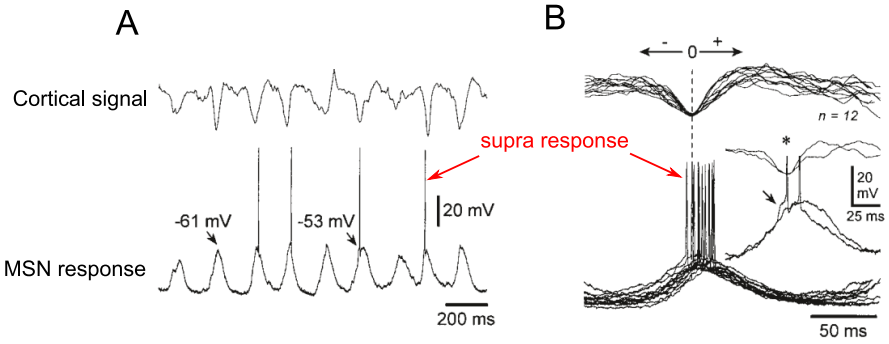

Figure 2.5: MSNs supratheshold depolarizations coincide with large amplitude EEG spindle waves, adapted from Mahon (2001) [154]. We can observe on both figures the correlation between a suprathreshold response in a MSN and an EEG motif (spinle wave). **(A)** A cortical EEG (top) and spontaneous intracellular activity of a MSN (bottom) were recorded at the same time. **(B)** Cortical EEGs (top) and related suprathreshold synaptic depolarizations (bottom) are superimposed.

Thus, if a spike occurs in a collective firing phase ("supra pattern"), it is likely to induce a suprathreshold response in the striatum. Otherwise, an associated subthreshold response would be more probable. In the model, the spikes that would coincide with a "supra pattern" in the filtered LFP would be associated with calcium amplitudes C_X^{supra}, C_{XX}^{supra}, C_{XY}^{supra} and c_X^{tot} summation for a supra stimulation. Other spikes apart from these patterns would be associated with calcium amplitudes C_X^{sub}, C_{XX}^{sub}, C_{XY}^{sub} and c_X^{tot} summation for a sub stimulation.
To identify this possible correlation, several methods can be used: the spike-triggered averaging, the

autocorrelogram, and the distribution of phases.

- The spike-triggered average is the average stimulus (here LFP, noted $X(t)$) preceding a spike. This method is used to determine the response characteristics of a neuron, through the spikes generated when a time-varying stimulus is received. To compute it, the stimulus in the time window preceding each spike is extracted, and the resulting stimuli are averaged [205]. If the stimulus has a zero mean, these response properties can be estimated by computing the average of the spike-triggered average.

$$A = \frac{1}{N}\sum_{i=1}^{N} X(t_i) \tag{2.14}$$

  where t_i is the time of the ith spike, $X(t_i)$ represents the stimulus presented during the temporal window preceding that time, and N is the total number of spikes.

  In our study our time window was centered around the spike time, with limits ± 1 s.

- The correlation between a signal and a delayed version of itself is known as autocorrelation. It is frequently employed in signal processing, for example to locate missing frequencies in inferred signals, or to detect periodic signals that are hidden by noise [101].

  The definition of the autocorrelation function between times t_1 and t_2 is

$$R_{XX}(t_1, t_2) = E[X(t_1)X(t_2)] \tag{2.15}$$

  In our study, our time window was centered around the spike time, with limits ± 1 s. For each spike, we consider all inter-spike intervals in this time window. Then we compute the distribution of these autocorrelations.

- Data generated from EEG recordings show that brain dynamics is noisy, nonstationary, nonlinear, and can exhibit temporal discontinuities. The Hilbert transform (HT), a linear operator like the FFT, is useful for studying nonstationary signals because it expresses frequency as a rate of change in phase, allowing the frequency to shift with time. Indeed, brain recordings often display several time-varying frequencies [86]. In our study, we filtered the LFP signal (X_{filter}) for theta bands (5-12 Hz), beta (15-35 Hz) and gamma (40-100 (52-98 because of noise at 50 Hz in this experiment)). Then for each spike at t_i we compute ϕ, by applying a hilbert transform to determine which phase of the filtered LFP corresponds, and an angle function to get the phase angle:

$$\phi = \text{angle}(\text{HT}(X_{\text{filter}}(t_i))) \tag{2.16}$$

  Finally, we computed the distribution of these phase angles ϕ.

2.3 Fit of the model to ex vivo ITDP data to infer corticostriatal and thalamostriatal plasticities from in vivo LFP recordings

2.3.1 Computational model fit

We present the outcomes of the fitted model as an illustration, whose parameters resulting from the calibration are presented in table 2.1.
In the control conditions $|\Delta t| = 100$ ms, since the two stimulations are spaced by a large time interval, the calcium concentration (Ca) traces are relatively independent so that the effect of the nonlinear summation is limited, see figure 2.6 (A). This way, the maximum of the Ca traces never reaches any plasticity threshold (θ_{p_X} and θ_{d_X}) and the evaluation of the synaptic weights W_X endures no change, see figure 2.6 (B).

Table 2.1: Parameters used for the ITDP model. Fitted parameters were found using CMA-ES algorithm with experimental data.

Parameter	Value	Definition
Fixed parameters		
s	2	slope parameter
LTP	2.5	maximal potentiation value
LTD	0.5	maximal depression value
Fitted parameters		
τ_{CS}	140 s	time const. for synaptic efficacy eq., CS
τ_{TS}	140 s	time const. for synaptic efficacy eq., TS
ρ^*_{CS}	0.234	switching point for synaptic efficacy eq., CS
ρ^*_{TS}	0.270	switching point for synaptic efficacy eq., TS
$\gamma_{p_{\mathrm{CS}}}$	858	LTP rate, CS
$\gamma_{p_{\mathrm{TS}}}$	952	LTP rate, TS
$\gamma_{d_{\mathrm{CS}}}$	694	LTD rate, CS
$\gamma_{d_{\mathrm{TS}}}$	735	LTD rate, TS
$\theta_{p_{\mathrm{CS}}}$	24.9	LTP threshold, CS
$\theta_{p_{\mathrm{TS}}}$	25	LTP threshold, TS
$\theta_{d_{\mathrm{CS}}}$	22.6	LTD threshold, CS
$\theta_{d_{\mathrm{CS}}}$	22.9	LTD threshold, TS
σ_{CS}	1.12	noise const., CS
σ_{TS}	1.12	noise const., TS
$\tau_{\mathrm{Ca_{CS}}}$	0.0212 s	time const. for calcium conc. eq., CS
$\tau_{\mathrm{Ca_{TS}}}$	0.0542 s	time const. for calcium conc. eq., TS
$C^{\mathrm{supra}}_{\mathrm{CS}}$	15.9	Amplitude for synaptic calcium conc. eq., CS, supra
$C^{\mathrm{supra}}_{\mathrm{TS}}$	22.5	Amplitude for synaptic calcium conc. eq., TS, supra
$C^{\mathrm{supra}}_{\mathrm{CSCS}}$	4.56	Amplitude for calcium conc. eq., CS $\rightarrow$ CS, supra
$C^{\mathrm{supra}}_{\mathrm{TSTS}}$	0.648	Amplitude for calcium conc. eq., TS $\rightarrow$ TS, supra
$C^{\mathrm{supra}}_{\mathrm{CSTS}}$	22.2	Amplitude for calcium conc. eq., TS $\rightarrow$ CS, supra
$C^{\mathrm{supra}}_{\mathrm{TSCS}}$	15.3	Amplitude for calcium conc. eq., CS $\rightarrow$ TS, supra
$C^{\mathrm{sub}}_{\mathrm{CS}}$	7.68	Amplitude for calcium conc. eq., CS, sub
$C^{\mathrm{sub}}_{\mathrm{TS}}$	15.0	Amplitude for calcium conc. eq., TS, sub
$C^{\mathrm{sub}}_{\mathrm{CSCS}}$	2.20	Amplitude for calcium conc. eq., CS $\rightarrow$ CS, sub
$C^{\mathrm{sub}}_{\mathrm{TSTS}}$	0.432	Amplitude for calcium conc. eq., TS $\rightarrow$ TS, sub
$C^{\mathrm{sub}}_{\mathrm{CSTS}}$	14.8	Amplitude for calcium conc. eq., TS $\rightarrow$ CS, sub
$C^{\mathrm{sub}}_{\mathrm{TSCS}}$	7.40	Amplitude for calcium conc. eq., CS $\rightarrow$ TS, sub
D_{CS}	0.00765 s	Delay for calcium conc. eq., CS
D_{TS}	0.00774 s	Delay for calcium conc. eq., TS
D_{CSCS}	0.0131 s	Delay for calcium conc. eq., CS $\rightarrow$ CS
D_{TSTS}	0.0106 s	Delay for calcium conc. eq., TS $\rightarrow$ TS
D_{CSTS}	0.000874 s	Delay for calcium conc. eq., TS $\rightarrow$ CS
D_{TSCS}	0.000623 s	Delay for calcium conc. eq., CS $\rightarrow$ TS

For the $|\Delta t| = 15$ ms conditions, typical Ca traces show a rapid rise shortly after the stimulation, followed by an exponential decay, see figure 2.7 (A). In general, CS and TS calcium concentration evolutions display little difference. That is coherent with the experimental data showing similar platicity results in both types of synapses in most conditions. The only case where CS and TS synapses exhibit different plasticities is when a CS stimulation inducing a suprathreshold response in MSNs is followed by a TS stimulation inducing a subthreshold response with a delay $\Delta t = t_{TS} - t_{CS} = +15$ ms, see figure 2.2 (CS then TS column, supra-sub line). In this situation, no plasticity is noticed in TS synapses while LTP is observed in CS synapses. The simulation of this condition displays that the maximal amplitude between the CS and TS Ca traces are noticeably distinct, see figure 2.7 (A) (CS then TS column, supra-sub line). While the TS Ca maximum stays slightly below the thresholds, the CS one rises above the LTP threshold $\theta_{p_{\mathrm{CS}}}$. Since the synaptic efficacy depends on the average fraction of time spent above a given threshold, see equation (2.13), this effect contributes to potentiation, see equation (2.1). The repetition of the same organization of stimulations leads to $W_{\mathrm{TS}} = 1$, i.e. no plasticity in TS synapses, and $W_{\mathrm{CS}} = \mathrm{LTP}$, i.e. LTP in CS synapses, see figure 2.7 (B) (CS then TS column, supra-sub line).

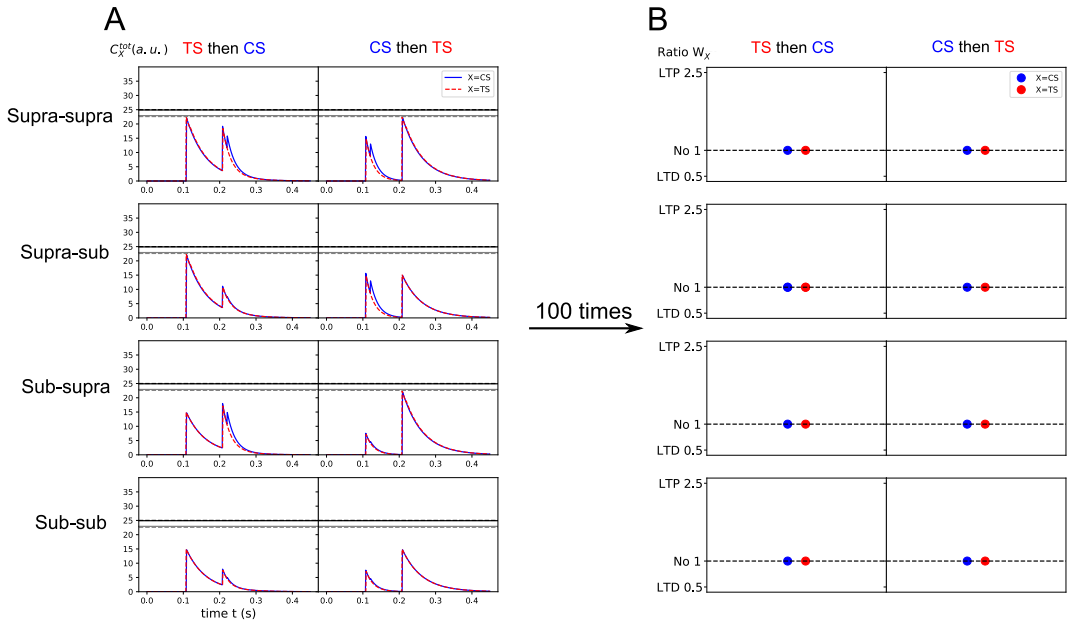

Figure 2.6: Results of numerical implementations of the model with the parameters fitted on experimental data for control conditions ($|\Delta t| = 100$ ms), supra or sub stimulations, for TS then CS ($\Delta t < 0$) or CS then TS ($\Delta t > 0$) pairings. In all cases no plasticity occurs, in accordance with experimental controls. The different conditions are organized following the presentation of figure 2.2, for an easy comparison between numerical and experimental results. **(A)** Calcium concentrations of CS (blue) and TS (dotted red) synapses. Black lines are LTP thresholds (solid line for $\theta_{p_{\mathrm{CS}}}$ and dotted line for $\theta_{p_{\mathrm{TS}}}$), gray lines represent LTD thresholds (solid line for $\theta_{d_{\mathrm{CS}}}$ and dotted line for $\theta_{d_{\mathrm{TS}}}$). Synapses can be potentiated when calcium traces rise above LTP threshold θ_{p_X}. Synapses can be depressed when calcium traces rise above LTD threshold θ_{d_X} and stay under LTP threshold θ_{d_X}. **(B)** After a 100 times repetition of the process, followed by a waiting period, the plasticity ratios W_X are computed. For each panel W_{CS} are on the left side and W_{TS} are on the right side. These numerical plasticity outcomes reproduce correctly the experimental control conditions.

For all $|\Delta t| = 15$ ms conditions, the outcomes W_X values of our model reproduced correctly the experimental results: LTP, LTD, or nothing (see figure 2.7 (B) for numerical results that can be compared to the experimental data in figure 2.2).

2.3.2 Application to predict corticostriatal and thalamostriatal plasticities in mice performing motor learning and motor adaptation tasks (LFP frequency analysis results)

To use the in vivo extracted cortical and thalamic spike trains as inputs in our model (to infer in vivo CS and TS plasticities), it is necessary to identify whether these spikes are associated with sub- or suprathreshold MSN responses. For that purpose, the identification of collective cortical or thalamic firing behaviours could establish the distinction between sub and supra for a given spike. Indeed a supratheshold MSN response could happen if a large number of cortical or thalamic neurons fire at the same time.
Therefore, we analyzed the LFP signals (one recorded in the thalamus and one recorded in the cortex) coupled with a sample of spike trains (4 recorded in the thalamus and 3 recorded in the cortex) by computing the spike-triggered average, the autocorrelogram and the phases distribution for beta, gamma and theta frequency ranges. Figure 2.8 presents an example of such analysis for a thalamic LFP recording and spike train. The spike-triggered average (figure 2.8 (A)) displays an oscillatory behaviour around 0 s, with a frequency around 8.3 Hz which is in the range of theta rythms (5-12 Hz). Consistently, the phase distribution for the LFP filtered for theta frequencies (figure 2.8 (C, left)) highlights a more important phase, compared to phase distributions for the LFP filtered for beta and gamma frequencies (figure 2.8 (C, middle and right)). The autocorrelogram (figure 2.8 (B)) also highlights slight oscillations, but which would need to be more precisely quantified.

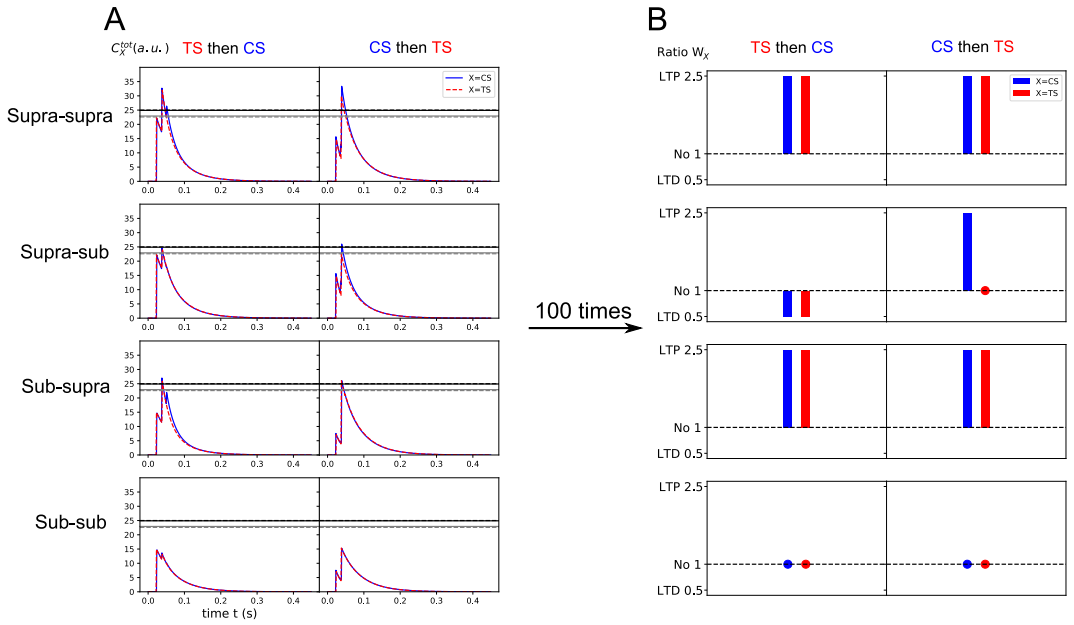

Figure 2.7: Results of numerical implementations of the model with the parameters fitted on experimental data for all conditions with $|\Delta t| = 15$ ms, supra or sub stimulations, for TS then CS ($\Delta t < 0$) or CS then TS ($\Delta t > 0$) pairings. The different conditions are organized following the presentation of figure 2.2, for an easy comparison between numerical and experimental results. **(A)** Calcium concentrations of CS (blue) and TS (dotted red) synapses. Black lines are LTP thresholds (solid line for $\theta_{p_{\mathrm{CS}}}$ and dotted line for $\theta_{p_{\mathrm{TS}}}$), gray lines represent LTD thresholds (solid line for $\theta_{d_{\mathrm{CS}}}$ and dotted line for $\theta_{d_{\mathrm{TS}}}$). Synapses can be potentiated when calcium traces rise above LTP threshold θ_{p_X}. Synapses can be depressed when calcium traces rise above LTD threshold θ_{d_X} and stay under LTP threshold θ_{d_X}. **(B)** After a 100 times repetition of the process, followed by a waiting period, the plasticity ratios W_X are computed. For each panel W_{CS} are on the left side and W_{TS} are on the right side. These numerical plasticity outcomes reproduce correctly the experimental ITDP measurements presented in figure 2.2.

All in all, these analyses point out that there is an oscillatory behaviour at a particular frequency, that is many neurons fire synchronously. Such large concentrated inputs could lead to suprathreshold responses in the MSNs [154]. Thus, the identification of supratheshold conditions makes possible the use of experimental recordings as inputs in our computational model, which has not been achieved yet due to the lack of experimental data.

2.4 Discussion

ITDP experiments have pointed out a significant role of the thalamus in corticostriatal plasticity, which is consistent with former STDP studies on the same circuits [164]. To better understand this plasticity process, we developed an ITDP computational model which successully reproduced the experimental results for the 16 conditions on CS and TS plasticities. However some points would need to be improved. It seems that the LTP (θ_{pX}) and LTD (θ_{dX}) thresholds are too similar, it would be important to further investigate whether improvements could be achieved in that direction. Similarly the model does not seem robust enough since the calcium concentration amplitudes, see figures 2.6 and 2.7, are only slightly below or above thresholds θ_{pX}, θ_{dX} (depending on the condition). Thus, little variations $\delta\Delta t$ could significantly change the resulted plasticity. The fit of the model would need to include $\delta\Delta t$ variations to improve the robustness of the model. Another point is that this model has no spatial structure, it could be interesting in the future to consider it. Actually the distance between CS and TS synapses seems to play an important role in plasticity, since it impacts the calcium dynamics [100].

Another experiment was then to train mice on a motor learning task, which involves the striatum,

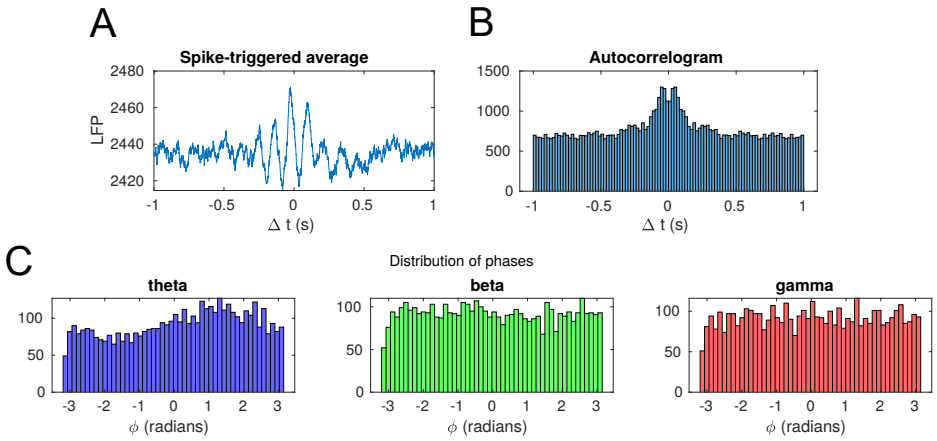

Figure 2.8: Thalamic LFP correspondance with a thalamic spike train analysis reveals oscillations. **(A)** The spike-triggered average displays an oscillatory behaviour around 0 s, with a frequency around 8.3 Hz which is in the range of theta rythms. **(B)** The autocorrelogram highlights slight oscillations. **(C)** Phase distribution for a filtered LFP for theta (left), beta (middle) and gamma (right) bands. The phase distribution for the LFP filtered for theta frequencies highlights a more important phase, compared to phase distributions for the LFP filtered for beta and gamma frequencies.

and record the LFP signals to infer spikes in cortical and thalamostriatal neurons. Our role would be then to determine whether LTP, LTD or nothing is expected to happen with such spike trains (since LTP or LTD cannot be measured in vivo). The final purpose of these experiments is to determine the functional role of each input to the MSNs (cortical or thalamic) in learning. For instance, thalamocortical synapses have been hypothesized as sending a "reset" message when the animal encounters a situation not according to the learned task [166, 30].
In order to apply our computational model to in vivo recorded cortical and thalamic spike trains as inputs, it must be determined whether they are associated with sub- or suprathreshold MSN responses. This can be done through the LFP analysis linked with spike trains, to identify collective cortical or thalamic firing behaviours which could induce suprathreshold MSN responses. The analysis of a few samples gave encouraging signs that this distinction between sub and supra can be identified, but signals lack precision. More recordings will be carried out by the experimentalists in a near future with a more performant electrode (more channels). These new data will be analyzed the same way we did in this chapter, and could be used in our model. The model's outcomes will then be compared with the ex vivo ITDP measurements that will be carried out on sacrificed mice 24 hours after the last motor adaptation task.

We have seen in this chapter a model at a cell and synapse scale. When considering more cells interacting through multiple synapses, it is useful to reduce a bit more the complexity of the cell and synaptic dynamics description. We will see in the next chapter a modelling study at a network level.

Chapter 3

Modulation of neural collective behaviours by astrocytes

3.1 Neuronal synchronization functions and interplay with astrocytes

Neurons receive and emit action potentials, that often display synchronized behaviours. Interestingly, while we have seen in the last chapter that the synchronization between spike times at a cellular scale carries important information, the synchronization at a network scale would diminish the complexity of the information received by each neuron [16]. Therefore, it does not seem that large-scale synchronization could constitute a form of time-coded information [87]. Instead, the specific features of synchronization behaviours, such as beta rythms between 12.5 and 30 Hz, point towards a functional function for the processing of neural information [68].

Several cognitive phenomena were linked to neural network synchronization, such as memory formation [16], directed attention [167], and sensory inputs processing [18]. Furthermore, impairments in synchronization can be observed in some pathological states, such as epiletic seizures [118].

More recently, it has been highlighted that neuronal synchronization phenomena could be modulated by astrocytes [182, 10] (these effects will be further specified in the sections below). Because of the fact that an astrocyte is affected by a large number of synapses, gliotransmission may also contribute in the effect of neuronal synchronization. An improved understanding of the synchronization process could be achieved through analysis of bidirectional interactions between astrocytes and neuronal cells [156].

In this chapter, we study how astrocytes could modulate collective behaviours such as Up-Down oscillation dynamics in section 3.2 and epileptic seizures in section 3.3. We modeled the first issue with a rate model, and since synchronization patterns depend not only on the dynamical properties of individual oscillators but also on the underlying structural connectivity [247], we developed an integrate-and-fire network used for both sections. These two different models have been analyzed through equilibrium and stability analysis.

3.2 A rate and a spiking model to study cortical Up-Down dynamics modulation by astrocytes

The following study has been published: Blum Moyse, L., & Berry, H. (2022). Modelling the modulation of cortical Up-Down state switching by astrocytes. *PLoS Computational Biology, 18*(7), e1010296. *https://doi.org/10.1371/journal.pcbi.1010296*. The section below is extracted with a few adaptation from this article.

3.2.1 Experimental studies report a possible role of astrocyte dynamics in Up-Down states generation

Collective behaviors are characterized by the emergence of a coherent group behavior on the basis of simple interactions between the individuals of the group. Understanding the relationship between the properties of the individuals and the coordinated behavior at the population level usually demands theoretical approaches, for instance from theoretical physics [46, 103, 44]. Among the numerous forms of collective behaviors reported in the brain, Up-Down dynamics are characterized by spontaneous switches between periods of intense firing of the whole neuronal population (Up state) and periods of silence (Down state), even in the absence of external inputs [218, 56, 54, 212].

The cellular and network mechanisms at the origin of cortical Up-Down dynamics are still not well understood. For a large part, the phenomenon seems intrinsic to the cortical networks since it has been observed in cortical slices [54] and survives *in vivo* when the connections between cortex and thalamus, its main source of inputs, are lesioned [218]. A number of theoretical studies have proposed intrinsic mechanisms to explain cortical Up-Down dynamics, i.e., mechanisms that originate from the neurons themselves [20, 50, 108, 24]. These proposals usually postulate some sort of activity-dependent negative feedback of the firing rate, according to which individual neurons tend to decrease their firing rate after sustained periods of firing, and to increase it after sustained periods of silence. In the simplest cases, this negative feedback can rely on a slow adaptation current [50, 219, 224, 42] or short term plasticity [108, 24], for instance.

However, the existence of a rhythm generation mechanism intrinsic to the neurons of the network does not mean that the input from other brain regions cannot play a role. Several experimental studies have evidenced that oscillatory inputs from the thalamus do strongly impact or even trigger cortical Up-Down dynamics [194, 59, 143]. In agreement with these observations, several theoretical studies have been proposed to study Up-Down dynamics in the framework of the interplay between an intrinsic activity-dependent negative feedback of the firing rate and an external input to the network [110, 147, 116].

Recently, astrocytes have been identified by experimental studies as a new potential actor of population oscillations in the brain [142, 22, 40]. Astrocytes are non-neuronal neural cells that, together with oligodendrocytes, ependymal cells and microglia form the glial cells [115, 230]. Astrocytes can ensheath synaptic elements, thus forming a "tripartite" synapse where signalling information can flow between the presynaptic neuron, the postsynaptic neuron and the astrocyte [185, 14]. Indeed, at the tripartite synapse, astrocytes integrate neuronal activity as a complex transient signal of their intracellular Ca^{2+} concentration [199, 211]. In addition, astrocytic intracellular Ca^{2+} signals can, at least under certain conditions, trigger the release by the astrocyte of neuroactive molecules called gliotransmitters that may in turn modulate neuronal information transfer [203, 177]. The existence in physiological conditions of such a bilateral signalling between neurons and astrocytes is still debated among experimental neuroscientists, in particular regarding the impact of gliotransmitters on neurons [204, 76]. But if confirmed, it could explain the accumulated experimental evidence of the implication of astrocytes in information treatment in the brain [180, 102, 203].

Recently, a series of experimental studies has suggested that astrocytes are another intrinsic mechanism for the generation of Up-Down dynamics in cortical networks [189, 190]. In cortical slices, they have observed that increasing the calcium activity of a single astrocyte is enough to roughly double the probability to observe an Up state in the surrounding neurons, with no change of the amplitude nor the duration of these Up states [189]. In vivo experiments further showed that increasing calcium activity in a local population of astrocytes was temporally correlated to a shift of the local population of neurons to the Up-Down regime [190].

In spite of these significant experimental observations, the mechanism by which astrocytes modulate Up-Down cortical dynamics is still unknown. In particular, it is not understood how the modulation by astrocytes interact or rely on the other identified mechanisms of Up-Down state generation in the neurons. Here, we propose a mathematical model to explore the possible mechanisms by which astrocytes control the emergence of Up-Down dynamics of their surrounding neuronal network populations. To that aim, we extended the model proposed by [116] for Up-Down dynamics in a network of excitatory and inhibitory cortical neurons with a population of astrocytes. This provided us with theoretical tools to understand how the release of gliotransmitters by the astrocytes alters the dynamics of neuronal network towards the emergence of Up-Down dynamics.

3.2.2 Neuron-astrocytes computational models, equilibrium and stability analyses

3.2.2.1 Rate model

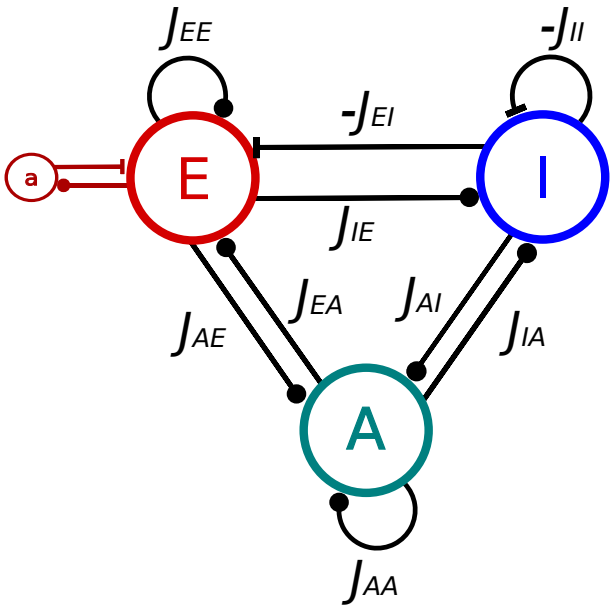

Figure 3.1: **Interactions between the three populations of the model.** E for excitatory neurons, I for inhibitory neurons and A for astrocytes. a represents the adaptation mechanism of E cells. Lines terminated with a full circle represent positive interactions whereas those terminated with a bar represent inhibition (of I cells on E and I, and adaptation a on E cells). J_{XY} represent the synaptic strength from the Y population toward the X population. In case of inhibition these terms are negative.

The model of Jercog et al. (2017) [116] presented in the subsubsection 1.4.2.1 of the first chapter was designed to study the emergence of Up-Down dynamics in a neural network composed of an excitatory population E connected to an inhibitory population I in a all-to-all manner. Here, we extended it to account for the impact of astrocytes on the network (figure 3.1).

Astrocytes express a variety of receptors at their membranes, that bind the neurotransmitters or neuromodulators released by the presynaptic elements at the tripartite synapse, including glutamate, GABA, acetylcholine or dopamine [185, 230, 61]. Through these receptors, neuronal activity is integrated inside the astrocyte, which eventually converges in a complex signal of astrocytic intracellular Ca^{2+} [199, 211]. In response to this Ca^{2+} transient, astrocytes can, at least under certain conditions, release in the synapse a variety of molecules, referred to as "gliotransmitters". Upon binding to the pre or postsynaptic element of the tripartite synapse, gliotransmitters can in turn hyperpolarize or depolarize the neuronal membrane [204, 203, 177]. Interestingly, whereas the astrocytic cytosolic calcium transients are very slow events, especially in the soma (around 10-20 sec on average), gliotransmitter release events are much faster (around 1 sec) [190, 28].

According to this oversimplifying birds-eye view of neuron-astrocyte interactions, the astrocytic response to presynaptic neuronal activity is similar to the process of neuronal integration: presynaptic neuronal activity is integrated in astrocytes as a calcium trace that triggers a peak-like release of gliotransmitters that in turn affects postsynaptic membrane voltage. The major differences are i) integration time-scales and gliotransmitter release dynamics in astrocytes are different from electrical signalling in neurons and ii) the equivalent of inhibitory/depolarizing neuronal inputs that decrease the membrane potential does not seem to exist for astrocytic Ca^{2+}. To model astrocyte activity, we thus opted for same formalism of rate equations (1.53) or (1.54), but with different time scales and expressed the rate of gliotransmitter release by the astrocyte as

$$\tau_A \frac{dr_A}{dt} = -r_A(t) + \phi_A(I_A(t) + \sigma\xi_A(t)) \tag{3.1}$$

with the constraint $\tau_A \gg \tau_I$ and $\tau_A \gg \tau_E$. To our knowledge, there are no a priori reasons to

consider that external inputs to the cortical network under study are restricted to a given subtype of brain cells, either excitatory neurons, inhibitory neurons or astrocytes. Therefore, we fed an oscillatory external input was to all cell populations, including astrocytes (variable ξ_A above).

Whereas one expects positive values for the firing threshold θ_X of neurons in equation (1.55) (i.e. neurons remain silent below a threshold of their input), we will favor negative values for θ_A, in order to account for the spontaneous calcium activity of astrocytes [230].

We now can give a definition for the three internal recurrent inputs:

$$I_X(t) = J_{XE} r_E(t) + J_{XI} r_I(t) + J_{XA} r_A(t) \tag{3.2}$$

with now $X = \{E, I, A\}$. The synaptic couplings J_{XY} (with $X, Y = \{E, I, A\}$), describe the strength of the connection from population Y to X. They verify $J_{XE} > 0$ (excitatory), $J_{EI} < 0$, $J_{II} < 0$ (inhibitory) and $J_{AX} \geq 0$ (i.e. both E and I increase the rate of gliotransmitter release in astrocytes).

A fixed-point and linear stability analysis of the rate model defined by equations (1.53) to (1.55) and (3.1) (3.2) is provided below, in subsubsection 3.2.2.1. The values of the parameters in the equations above are given in Table 3.1.

Table 3.1: **Parameters used for the rate model equations** (1.53) **to** (1.55) **and** (3.1) (3.2)**.**

Parameter	Value	Definition	Parameter	Value	Definition
τ_E	10 ms	time const., E	τ_I	2 ms	time const., I
τ_A	20 ms	time const., A	τ_a	500 ms	time const., adaptation
θ_I	25	threshold, I	θ_A	-3.5	threshold, A
J_{EE}	5 s	strength, E $\to$ E	J_{EI}	-1 s	strength, I $\to$ E
J_{II}	-0.5 s	strength, I $\to$ I	J_{IE}	10 s	strength, E $\to$ I
J_{AA}	0.1 s	strength, A $\to$ A	J_{EA}	1 s	strength, A $\to$ E
J_{IA}	0.5 s	strength, A $\to$ I	g_E	1 Hz	gain, E
g_I	4 Hz	gain, I	g_A	1 Hz	gain, A
σ	$3.5\sqrt{2}$	noise std	θ_E	$\in [-10, 20]$	threshold, E
β	$\in [0, 10]$s	strength, adaptation	J_{AE}	0.5 s	strength, E $\to$ A
J_{AI}	0.5 s	strength, I $\to$ A			

Fixed points and linear stability analyses

Noiseless model. We start with the rate model defined by equations (1.53) to (1.55) and (3.1) (3.2), and first neglect the external noisy input. In this case, the nullclines of the system are given by

$$r_E = g_E[I_E - a - \theta_E]_+ \tag{3.3}$$

$$r_I = g_I[I_I - \theta_I]_+ \tag{3.4}$$

$$r_A = g_A[I_A - \theta_A]_+ \tag{3.5}$$

$$a = \beta r_E \tag{3.6}$$

Note that because of the rectification functions in equations (3.3) to (3.5), the values of the rates at a fixed point cannot be negative. The rate model equations (1.53) to (1.55) and (3.1) (3.2) being a piecewise-smooth system, a rigorous analysis of the stability of its fixed points would require dedicated analysis methods [66]. Here, we leave this analysis for further work and assume that all fixed points remain far from the switching manifolds where the arguments of the rectification functions change signs and proceed to linear stability analysis in each of the respective regions.

A Down or silent state can be characterized as a fixed-point where both neuronal populations are silent, i.e. $r_E = r_I = 0$ spks/s. equations (3.6) means that adaptation a also vanishes in such a Down state. The rectification functions of equations (3.3) and (3.4) impose $\theta_E \geq 0$ and $\theta_I \geq 0$ for the Down fixed-point to exist. Indeed $\theta_E < 0$ would mean from equation (3.3) that $r_A < 0$ at the fixed-point (since $r_E = 0$ spks/s), which is not compatible with equation (3.5). Hence the Down state exists only if $\theta_E \geq 0$ or $\theta_I \geq 0$. If, in addition $\theta_A \geq 0$, the Down state is $(r_E, r_I, r_A, a) = (0, 0, 0, 0)$. Assuming that all the rectification functions in equations (1.53) (1.54) (3.1) vanish in the neighborhood of the fixed point, we find that this Down state is stable by linear stability analysis (eigenvalues of the Jacobian:$\{-1/\tau_E, -1/\tau_I, -1/\tau_A, -1/\tau_a\}$).

In the case $\theta_A < 0$ (still with $\theta_I \geq 0$ and $\theta_E \geq 0$), we assume that the argument of the rectification function in equation (3.1) is strictly positive, while the rectification functions in equations (1.53) and (1.54) vanish. The nullcline for r_A, equations (3.5) then becomes $r_A = g_A(J_{AA}r_A - \theta_A)$. Therefore, there still is a positive Down fixed-point $(r_E, r_I, r_A, a) = (0, 0, -g_A\theta_A/(1 - g_AJ_{AA}), 0)$ but only for:

$$\theta_E > -g_AJ_{EA}\theta_A/(1 - g_AJ_{AA}), \tag{3.7}$$

as well as $\theta_I > -g_AJ_{IA}\theta_A/(1 - g_AJ_{AA})$ and $g_AJ_{AA} < 1$. Close to this fixed-point, the Jacobian matrix reads

$$\begin{pmatrix} -1/\tau_E & 0 & 0 & 0 \\ 0 & -1/\tau_I & 0 & 0 \\ 0 & 0 & (g_AJ_{AA} - 1)/\tau_A & 0 \\ \beta & 0 & 0 & -1/\tau_a \end{pmatrix} \tag{3.8}$$

so stability is granted whenever $g_AJ_{AA} < 1$, i.e as soon as the equilibrium value for r_A exists.

To find an Up state fixed-point with non-zero rates we follow [116] and substitute the value of the adaptation at equilibrium $a = \beta r_E$, assuming that the arguments of all the rectification functions of equations (1.53) (1.54) (3.1) are strictly positive. This yields:

$$r_E = \frac{h_E\theta_E + f_{EI}\theta_I + f_{EA}\theta_A}{|M|}, \tag{3.9}$$

$$r_I = \frac{f_{IE}\theta_E + (h_I - \beta J'_{AA})\theta_I + (f_{IA} + J_{IA}\beta)\theta_A}{|M|} \tag{3.10}$$

and

$$r_A = \frac{f_{AE}\theta_E + (f_{AI} + J_{AI}\beta)\theta_I + (h_A - \beta J'_{II})\theta_A}{|M|} \tag{3.11}$$

with

$$J'_{XY} = J_{XY} - \frac{1}{g_X}, \tag{3.12}$$

$$h_X = J'_{YY}J'_{ZZ} - J_{YZ}J_{ZY}, \tag{3.13}$$

$$f_{XY} = J_{XZ}J_{ZY} - J_{XY}J'_{ZZ}, \tag{3.14}$$

and

$$|M| = J_{AE}f_{EA} + J_{AI}(f_{IA} + J_{IA}\beta) + J'_{AA}(h_A - \beta J'_{II}) \tag{3.15}$$

One condition for the UP state fixed-point to exist is that the right hand side of equations (3.9) (3.10) (3.11) are positive. Given our reference parameters (table 3.1), the condition on r_I, i.e., $r_I > 0$ is the most restrictive condition. In other words, when θ_E and β are varied, equation (3.10) is the first one to become positive. Moreover, with our reference parameters, it turns out that the determinant $|M| < 0$. The condition for the existence of the Up state fixed-point thus becomes

$$\beta < \frac{f_{IE}\theta_E + h_I\theta_I + f_{IA}\theta_A}{J'_{AA}\theta_I - J_{IA}\theta_A}. \tag{3.16}$$

since $J'_{AA}\theta_I - J_{IA}\theta_A < 0$ with our reference parameters (table 3.1).

Considering that in the neighborhood of the Up fixed-point, all the rectification functions of the model are positive, the Jacobian matrix reads

$$\begin{pmatrix} \frac{-1+g_E(J_{EE}-\beta)}{\tau_E} & \frac{g_EJ_{EI}}{\tau_E} & \frac{g_EJ_{EA}}{\tau_E} \\ \frac{g_IJ_{IE}}{\tau_I} & \frac{-1+g_IJ_{II}}{\tau_I} & \frac{g_IJ_{IA}}{\tau_I} \\ \frac{g_AJ_{AE}}{\tau_A} & \frac{g_AJ_{AI}}{\tau_A} & \frac{-1+g_AJ_{AA}}{\tau_A} \end{pmatrix}.$$

It is possible to obtain analytical expressions for the eigenvalues of this matrix, however these expressions are too complex to be really useful, even to determine their signs. We therefore estimated their values numerically to explore stability of the Up fixed-point, with numerical estimation of the sign of the real part of the eigenvalues of the matrix. Note finally that in regions where both the Up state and the Down state fixed-points are stable, the existence of a third, unstable and intermediate fixed-point can be evidenced by numerical analysis.

The effect of noise on the model. The addition of noise however complicates the above picture. In particular, spontaneous Up-Down transitions can occur even in the region where the Down state is stable and the Up state unstable, through a dynamical regime whereby noise triggers the Down to Up switches and adaptation triggers the reverse Up to Down transitions. In [116], it is proposed that this subregion can be estimated to start when the Up state is unstable under the sole influence of adaptation, a condition that can be deduced from equation (3.16) with $\beta = 0$:

$$\theta_E < -\frac{h_I\theta_I + f_{IA}\theta_A}{f_{IE}} \tag{3.17}$$

Likewise, the symmetrical regime exists in the region where the Up state is stable and the Down state unstable, for which Up-to-Down transitions are triggered by noise and Down-to-Up switches by adaptation. [116] proposes to delineate this region by the situation where adaptation in the Up-state is large enough to counterbalance the effect of θ_E, i.e. $\beta r_E + \theta_E > 0$, where r_E is given by equation (3.9), which yields

$$\beta > \frac{-\theta_E(J_{AE}f_{EA} + J_{AI}f_{IA} + J'_{AA}h_A)}{f_{EI}\theta_I + f_{EA}\theta_A + (h_E - J'_{AA}J'_{II} - J_{AI}J_{IA})\theta_E} \tag{3.18}$$

3.2.2.2 Stochastic spiking network model

We also modeled the three-population $\{E, I, A\}$ system of figure 3.1 by expressing it as a stochastic spiking network model instead of the firing rate framework of subsubsection 3.2.2.1. Following the same principle as above, where we used a classical neuron rate equation to model astrocyte gliotransmitter release, we used here leaky integrate and fire equations to model both neuronal membrane potential and the release of gliotransmitters by astrocytes. Hence, the membrane potential of the two populations of neurons reads:

$$\tau_E \frac{dV_i^E}{dt} = -(V_i^E - V_L) + I_{rec,i}^E(t) + I_{ext,i}^E(t) - \kappa_a I_{a,i}(t) \tag{3.19}$$

$$\tau_I \frac{dV_i^I}{dt} = -(V_i^I - V_L) + I_{rec,i}^I(t) + I_{ext,i}^I(t) \tag{3.20}$$

and similarly, we model gliotransmitter release from the astrocytes as:

$$\tau_A \frac{dG_i^A}{dt} = -(G_i^A - G_L^A) + I_{rec,i}^A(t) + I_{ext,i}^A(t) \tag{3.21}$$

with $i \in \{1, ..., N_X\}$. G_i^A is thus a phenomenological dimensionless variable that integrates the neuronal and astrocytic inputs to astrocyte i. According to the integrate-and-fire principle, whenever the membrane voltage of a neuron of population X exceeds its threshold θ_X at time t, a spike is emitted and the membrane voltage is reset to V_r^X. Similarly, when G_i^A exceeds the threshold G_{th}, astrocyte i emits a gliotransmitter release event, and G_i^A resets to G_r. Gliotransmitter release events and spikes are then integrated in the corresponding synaptic variable s_X (see equations (1.29) and (1.30)).

For the simulations of the spiking model, we assumed the following connectivity rules:

- full connectivity for neuron-to-neuron connections and for astrocyte-to-astrocyte connections. The latter emulates the organization of astrocytes as a syncytium. This biological concept corresponds to the idea that all astrocytes of a local region are somehow interconnected together into single functional network [230].
- only a fraction (10%) of the E or I neurons are subjected to gliotransmission from the astrocytes. These neurons are chosen at random (uniform distribution).
- 50 % of the astrocytes, chosen uniformly at random, receive inputs from the E or I neurons.

The latter two connectivity rules account from the observation that only part of the synapses of a given brain region are tripartite synapses contacted by astrocytes. The exact fraction seems to be quite variable from one region to the other, from 10 % to 90 % [230]. Therefore, our choice corresponds to a lower range of parameters.

One specificity of the original spiking model of Jercog et al. (2017) [116] is to account for synaptic variables by a single pair of variables u_X, s_X for each population, which can thus be considered as

population variables instead of individual cell variables. Their equations (1.29) (1.30) were presented in the subsection 1.3.2 of the first chapter.

Here we follow this model and define the recurrent input to each population $X = \{E, I, A\}$ as a population-level input as:

$$I^X_{rec,i}(t) = C^{XE}_i J_{XE} s_E(t) + C^{XI}_i J_{XI} s_I(t) + C^{XA}_i J_{XA} s_A(t) \tag{3.22}$$

where the A $\rightarrow$ E connectivity $C^{EA}_i = 1$ for 10% of the E neurons i (chosen uniformly at random) and 0 for the others (the same for C^{IA}_i). For the (E, I) $\rightarrow$ A connectivity, we used $C^{AE}_i = C^{AI}_i = 1$ for 50% of the astrocytes (chosen uniformly at random) and 0 for the others. All the others connectivities ($C^{EI}_i, C^{EE}_i, C^{IE}_i, C^{II}_i, C^{AA}_i$) were set to 1 (all-to-all connectivity).

Note that signal transmission in astrocytes is much slower than in neurons since it is based on reaction-diffusion (calcium signalling) instead of the propagation of an action potential [190, 28, 230]. To account for this important difference in timescales, we used transmission delays that were on the order of milliseconds for neurons ($[0, 1]$ ms) but on the order of seconds for astrocytes ($[0.5, 1.5]$ s, see Table 3.2).

In addition, the excitatory neurons displayed an after hyperpolarization (AHP) current. Its equation (1.31)is presented in the subsection 1.3.2 of the first chapter. The external input current $I^X_{ext,i}(t) = \sigma^X \sqrt{\tau_X} \eta_i(t)$ is a Gaussian white noise term.

Initial conditions were set as $V^X_i = V_r + (V_{th} - V_r)\eta_i$ and $G^A_i = G_r + (G_{th} - G_r)\eta_i$, where η_i is a random value with uniform distribution between 0 and 1. Unless indicated, we simulated the spiking network model using $N_E = 4{,}000$ excitatory neurons, $N_I = 1{,}000$ inhibitory neurons and $N_A = 2,000$ astrocytes. Each of these 2,000 astrocytes thus impacts 400 excitatory and 100 inhibitory neurons by gliotransmitter release, whereas half of them are individually impacted by the activity of the totality of the 4,000 E and 1,000 I neurons.

The values of the parameters in the equations above are given in Table 3.2. A fixed-point and linear stability analysis of the spiking model defined by equations (3.19) to (3.22), and (1.29) to (1.31), is provided below, in subsubsection 3.2.2.2.

Table 3.2: **Parameters used for the spiking model equations** (3.19) **to** (3.22)**, and** (1.29) **to** (1.31)**.**

Parameter	Value	Definition	Parameter	Value	Definition
τ_E	20 ms	time const., E	τ_I	10 ms	time const., I
τ_A	160 ms	time const., A	τ_a	500 ms	time const., adaptation
$\underline{\tau_E}$	1 ms	time const., u_E	$\underline{\tau_I}$	1 ms	time const., u_I
$\underline{\tau_A}$	1 ms	time const., u_A	J_{EE}	1.4 mV	strength, E $\rightarrow$ E
J_{EI}	-1.4 mV	strength, I $\rightarrow$ E	J_{II}	-1 mV	strength, I $\rightarrow$ I
J_{IE}	1.25 mV	strength, E $\rightarrow$ I	J_{AA}	0.16	strength, A $\rightarrow$ A
J_{AE}	0.053	strength, E $\rightarrow$ A	J_{EA}	22 mV	strength, A $\rightarrow$ E
J_{IA}	4.4 mV	strength, A $\rightarrow$ I	J_{AI}	0.058	strength, I $\rightarrow$ A
β	1 ms	time const., adaptation	κ_a	600	strength, adaptation
σ_E	3 mV	noise std, E	σ_I	3 mV	noise std, I
σ_A	3	noise std, A	V_r	14 mV	reset membr. pot.
G_r	9	reset gliotrans. release	V_{th}	20 mV	spike-threshold
G_{th}	13	gliotrans. release thresh.	τ^E_d	23 ms	decay time, E
τ^I_d	1 ms	decay time I	τ^A_d	2 ms	decay time, A
τ^E_r	8 ms	rise time, E	τ^I_r	1 ms	rise time, I
τ^A_r	8 ms	rise time, A	$d^E_{\min}$	0 ms	min. delay, E
$d^I_{\min}$	0 ms	min. delay, I	$d^E_{\max}$	1 ms	max. delay, E
$d^I_{\max}$	0.5 ms	max. delay, I	$d^A_{\min}$	500 ms	min. delay,A
$d^A_{\max}$	1.5 s	max. delay, A	V^E_L	7.6 mV	leak potential, E
V^I_L	6.5 mV	leak potential, I	G^A_L	7	leak gliotrans. rate, A

Fixed points and linear stability analyses

Analysis of the spiking model defined by equations (3.19) to (3.22), and (1.29) to (1.31), was carried out as follows. The nullclines of the population averaged rates are obtained from the equilibrium firing rate ($r_{X,0}$), which is given by the self consistent mean-field equation [38]:

$$r_{X,0} = \frac{1}{\tau_X}\left[\int_0^\infty \frac{dy}{y} e^{-y^2}(e^{2yy_t^X} - e^{2yy_r^X})\right]^{-1} \tag{3.23}$$

with

$$y_r^X = \frac{V_r - I_{X,0}}{\sigma_X} \qquad y_t^X = \frac{V_{th} - I_{X,0}}{\sigma_X} \tag{3.24}$$

and with the currents:

$$I_{E,0} = V_{L,E} + I_{rec,E} - \kappa_a \beta r_{E,0} \tag{3.25}$$

$$I_{I,0} = V_{L,I} + I_{rec,I} \tag{3.26}$$

$$I_{A,0} = V_{L,A} + I_{rec,A} \tag{3.27}$$

$$I_{rec,X} = C_{XE}N_E J_{XE} r_{E,0}\underline{\tau_E} + C_{XI}N_I J_{XI} r_{I,0}\underline{\tau_I} + C_{XA}N_A J_{XA} r_{A,0}\underline{\tau_A} \tag{3.28}$$

where C_{XY} is the connectivity (0.1 for astrocyte to neuron connection, 0.5 for neuron to astrocytes, 1.0 otherwise). Note that we replaced $I_{a,0} = \beta r_{E,0}$. These self-consistent equations are solved by finding the intersection between the right and the left side of equation (3.23). The fixed points are the intersections of the three surfaces $r_{E,0}$, $r_{I,0}$ and $r_{A,0}$. The stability of these fixed points is determined with the sign of the eigenvalue λ [38, 197, 141]. Solving the system

$$\begin{cases} \delta r_E = F_{EE}(\lambda)\delta r_E + F_{EI}(\lambda)\delta r_I + F_{EA}(\lambda)\delta r_A \\ \delta r_I = F_{IE}(\lambda)\delta r_E + F_{II}(\lambda)\delta r_I + F_{IA}(\lambda)\delta r_A \\ \delta r_A = F_{AE}(\lambda)\delta r_E + F_{AI}(\lambda)\delta r_I + F_{AA}(\lambda)\delta r_A \end{cases} \tag{3.29}$$

for the perturbations around the fixed-point, δr_E, δr_I and δr_A, one gets the condition (omitting the dependences on λ for readability):

$$\begin{aligned} &(F_{EE}-1)(F_{II}-1)(F_{AA}-1) + F_{EI}F_{IA}F_{AE} + F_{EA}F_{IE}F_{AI} \\ &-(F_{EE}-1)F_{IA}F_{AI} - F_{EI}F_{IE}(F_{AA}-1) - F_{EA}(F_{II}-1)F_{AE} = 0 \end{aligned} \tag{3.30}$$

with

$$F_{XY}(\lambda) = J_{XY}R_X(\lambda)S_Y(\lambda) \tag{3.31}$$

and the synaptic response function $S_Y(\lambda)$

$$S_Y(\lambda) = \frac{e^{-\lambda d^Y}}{(1+\lambda\tau_r^Y)(1+\lambda\tau_d^Y)} \tag{3.32}$$

In this equation, $R_X(\lambda)$ is the neuronal response function defined as

$$R_X(\lambda) = \frac{r_{X,0}}{\sigma_X(1+\lambda\tau_X)} \frac{\frac{\partial U}{\partial y}(y_t^X, \lambda\tau_X) - \frac{\partial U}{\partial y}(y_r^X, \lambda\tau_X)}{U(y_t^X, \lambda\tau_X) - U(y_r^X, \lambda\tau_X)} \tag{3.33}$$

with

$$U(y,\lambda) = \frac{e^{y^2}}{\Gamma\left[\frac{1+\lambda}{2}\right]} M\left(\frac{1-\lambda}{2}, \frac{1}{2}, -y^2\right) + \frac{2ye^{y^2}}{\Gamma\left[\frac{\lambda}{2}\right]} M\left(1-\frac{\lambda}{2}, \frac{3}{2}, -y^2\right) \tag{3.34}$$

with M is a confluent hypergeometric function. Stability is assessed by solving equation (3.30) for λ numerically. The fixed point is stable when its real part is negative.

3.2.2.3 Parameter estimation

The experimental data available for parameter estimation of the two models above exhibit strong variability. In [116], for instance, the numbers used to quantify the experimental measurements (distribution of duration of Up or Down phases, CV of the firing rates) vary significantly from one repetition of the experiment to the other. Over the seven repetitions of the same experiments (their Figure 2A and B), the mean duration of the Up phases varies from 0.24s to 0.73s, for example. With other experimentalists, using other experimental setups, and recording on different cortical regions, the variability would probably be even larger. Therefore, the classical methodologies for parameter

estimation would at best allow to match one specific repetition of a given experiment, where our objective here is to get a more generic overview of this system. Therefore, we have opted for an ad hoc method to set the values of the parameters. When available, we have set the initial guess for the parameters to rough estimates from the literature. For instance, the quantification of propagation delays of calcium waves in 3D astrocytes made in [28] sets an order of magnitude of around 1 to 2 sec for the maximal delay of astrocytes $d^A_{\max}$. For the other parameters, we used bifurcation studies like those shown below to locate regions of the parameter space in which model simulations are approximately in agreement with the variation range of the main experimental quantities of [116]. The results are given in table 3.1 and table 3.2.

3.2.2.4 Automatic segmentation of Up and Down phases

We quantified the statistics of Up and Down phases in rate model or spiking network simulations on the basis of the mean firing rate time series. In spiking network simulations, we first computed the mean population rate from the raster plot, using a sliding window of 10 ms and counting the total number of spikes emitted by all neurons (excitatory and inhibitory) in the window. Automatic segmentation of the firing rate time series into Up phases and Down phases was achieved by smoothing the sampling rate using a sliding window of $+/-$ 50 points around each data point and replacing each data point by the median over the window. Transition of the smoothed data curve through a threshold of 1.0 Hz from below was considered a switch from a Down to a Up state, whereas transition from above signaled a reverse switch, from Up to Down state. The first and last phases of a simulation were systematically discarded and not accounted for in the statistics.

3.2.3 Modelling the modulation of cortical Up-Down state switching by astrocytes

3.2.3.1 Rate model

We first illustrate the dynamics of the rate model described in subsubsection 3.2.2.1 by the simple numerical simulations of figure 3.2. In the absence of astrocytes (i.e. with $J_{IA} = J_{EA} = J_{AI} = J_{AE} = 0$ s, figure 3.2a), the model with the parameters of the figure is silent: the firing rate of the inhibitory neurons r_I vanishes, and that of the excitatory neurons, r_E, is also zero most of the time, except for small fluctuations due to external noise. Accordingly, adaptation is essentially off. We then added gliotransmission between excitatory neurons and astrocytes in figure 3.2b keeping all other parameters identical to figure 3.2a. Adding gliotransmission drastically changes the dynamics that now exhibits spontaneous transitions between long periods of silence for all neuronal populations and shorter periods of high firing rates for the excitatory and inhibitory neurons (around 10 and 5 Hz, respectively). In other words, astrocyte activity in the rate model switches the dynamics from silent to a Up-Down oscillatory dynamics, in agreement with experimental observations *in vivo* [190]. During an Up state, adaptation slowly increases and eventually triggers the Up-to-Down transition that ends the Up state.

Note that the average values of r_E, r_I and r_A during the Up and Down states in the simulation of the figure match the values predicted by the stability analysis in subsubsection 3.2.2.1. In particular, this analysis states that in the Down fixed-point, one expects $r_A = -g_A\theta_A/(1 - g_A J_{AA})$ while the neuronal rates vanish. In agreement, the rate of gliotransmitter release by the astrocytes r_A remains elevated during the Down states of figure 3.2b, even though the neurons are silent.

To analyze further these simulation results, figure 3.3 summarizes the fixed-point and linear stability analysis in subsubsection 3.2.2.1 in the (β, θ_E)-parameter plan. In the absence of noise, figure 3.3A, the system behavior is determined by two straight lines: the Down steady-state exists (and is stable) only on the right hand side of the line defined by equation (3.7) whereas the Up steady-state exists for the half-plan below the line defined by equation (3.16). This defines two regions of mono-stability, one where the Up state is the only fixed-point (U-region) and the other where the Down state in the only one (D-region). The region where both the Up state and the Down state exist is a region of bistability ("Bist." in the figure) where the dynamics converges to the Up or the Down state depending on the initial conditions. Finally, in the region where neither the Up nor the Down fixed-points exist, the arguments of the rectification functions regularly switch from positive to negative

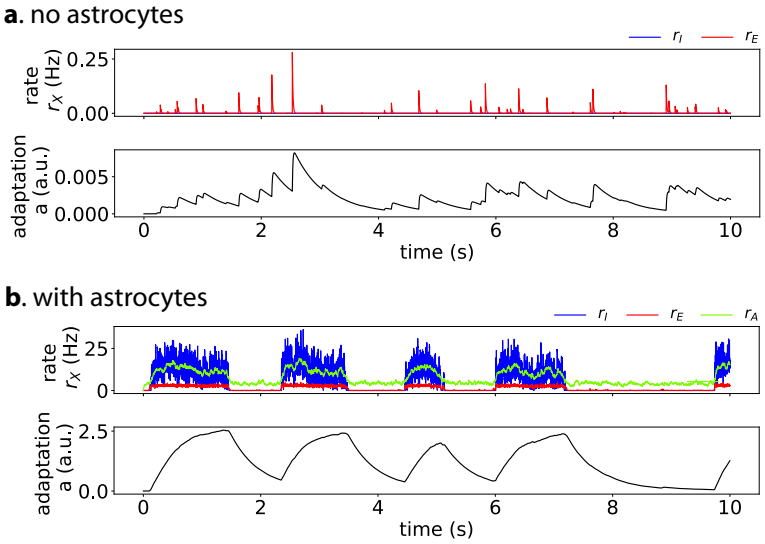

Figure 3.2: **Astrocytes in the rate model of subsubsection 3.2.2.1 switch the dynamics from silent to Up-Down.** (A) In the absence of astrocytic impact on the neurons ($J_{EA} = J_{AE} = J_{IA} = J_{AI} = 0$ s) the neurons are in a silent state with vanishing firing rates r_E (*red*) and r_I (*blue*) and adaptation a (*black*), corresponding to a Down-state fixed point. Please note the difference of y-scale between panels (A) and (B). (B) When gliotransmission between astrocytes and neurons is accounted for ($J_{EA} = 1$, $J_{IA} = J_{AI} = J_{AE} = 0.5$ s), *with no change of the other parameters*, the dynamics switches to Up-Down dynamics. All other parameters given in Table 3.1.

and back. This yields a regime of oscillations ("Osc"-region), that is a specific manifestation of the non-smooth character of the model.

With noise (figure 3.3B-C), spontaneous Up-Down transitions are expected to occur in the bistable and oscillatory regions of the noiseless system, but also in sub-regions of its U- and D-regions (see subsubsection 3.2.2.1). Altogether, this defines three dynamical regimes: low values of β and θ_E are predicted to give rise to a regime of perpetual high firing rates, i.e. a stable Up state. Conversely, large values of the excitatory neuron threshold θ_E are expected to yield a silent regime, or Down state, where neuronal firing rates vanish. Between those two regions, the system is predicted to switch spontaneously between periods of high population rates and periods or collective silence, i.e. $U \leftrightarrow D$ dynamics. A theoretical estimation for the frontier between the U and the $U \leftrightarrow D$ region with noise is given by equation (3.18) (figure 3.3, *dashed black lines*). Comparing with the percentage of the simulation-time spent in the Up state shows that in all the cases illustrated in figure 3.3B-C this expression indeed correctly positions the D-region on the plan, although it strongly underestimates its size. Likewise equation (3.17) (figure 3.3, *dashed green lines*) indeed indicates the transition between the D and the $U \leftrightarrow D$ regions, although, here again, the predicted size of the D region is strongly underestimated.

Remarkably, this frontier between $U \leftrightarrow D$ and D is very sensitive to modifications of gliotransmission couplings (the J_{XA}s and J_{AX}s): the presence of astrocytes indeed pushes this frontier to larger values of θ_E. The cyan star in figure 3.3B-C locates the parameter values used in figure 3.2. Without astrocytes, the star is located on the right hand side of the frontier between the $U \leftrightarrow D$ and the D region, thus explaining the silent state of figure 3.2a. With the addition of gliotransmission, the frontier moves rightwards, so that now, the star is located inside the $U \leftrightarrow D$ region. This explains the Up-Down regimes of figure 3.2B and C.

Taken together, these results indicate that astrocyte activity can indeed switch the network dynamics from silence to the Up-Down regime by altering the phase diagram of the dynamics. The effect of gliotransmission on the model dynamics is not drastic, in particular gliotransmission does not change the nature or the number of bifurcation points in the system. However, it displaces the frontiers separating dynamical regimes, thus allowing the expression of Up-Down dynamics for a larger range of values of the firing threshold of the excitatory neurons.

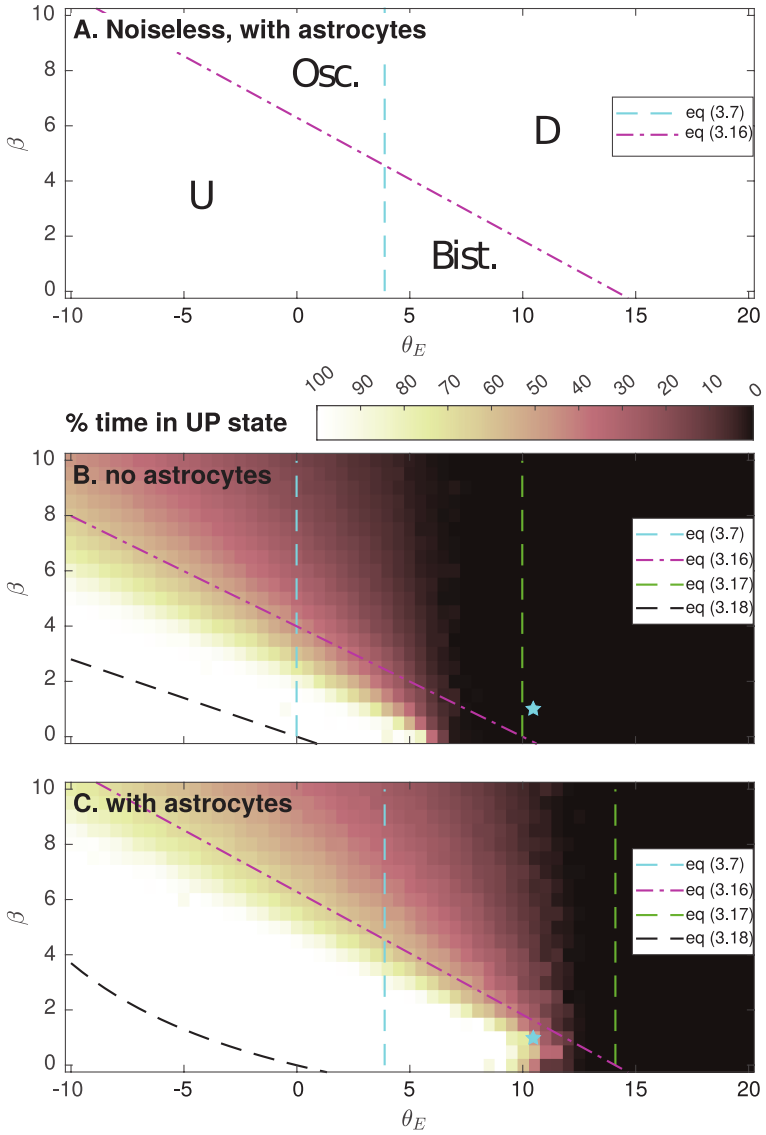

Figure 3.3: **Prediction of the dynamical regimes of the model.** Diagram as a function of the adaptation strength β and the threshold of the excitatory neurons θ_E. (A) In the absence of noise, the deterministic model exhibits two regions of monostability: the "U"-region where the Up state fixed-point is the only one, and the "D"-region where the Down state fixed-point is the unique fixed-point. Both fixed-points coexist in the bistable region "Bist." whereas the dynamics oscillates in the "Osc." region. Those regions are precisely delimited by equation (3.7) and equation (3.16). (B-C) With noise, three main regimes are predicted: a purely Up state in the bottom left part of the plan, a purely Down state in the right part of the plan and spontaneous transitions between Up and Down states in-between ($U \leftrightarrow D$). The color-code indicates the percentage of time spent in the Up state during a simulation. (C) Simulations were carried out with astrocytes ($J_{EA} = 1$, $J_{IA} = J_{AI} = J_{AE} = 0.5$ s), or (B) in their absence ($J_{IA} = J_{AI} = J_{EA} = J_{AE} = 0$ s). The cyan star locates the parameters of figure 3.2, which shows in particular that gliotransmission pushes the frontiers of the Up-Down region further to the right, effectively switching the dynamics to the Up-Down regime. Equation (3.17) and equation (3.18) are theoretical estimates of the frontiers between $U \leftrightarrow D$ and D or $U \leftrightarrow D$ and U. All other parameters given in Table 3.1.

3.2.3.2 Stochastic spiking network model

To assess the above mechanisms in a more biophysically realistic circuit, we next expressed the circuit of figure 3.1 as a stochastic spiking network model, with leaky integrate-and-fire neurons and astrocytes (subsubsection 3.2.2.2). Using the same illustration as for the firing rate model above, we start in figure 3.4 with a network devoid of astrocytes, i.e. for which $J_{AE} = J_{AI} = 0$ and $J_{EA} = J_{IA} = 0$ mV. The neurons exhibit a very short firing phase at the beginning of the

stimulation due to our choice of random initial conditions but quickly converges back to a silent state.

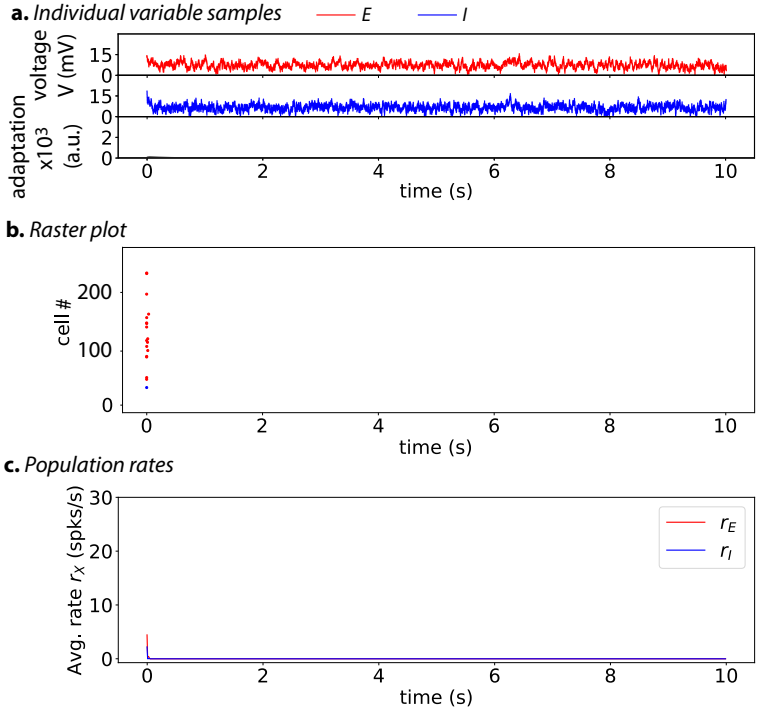

Figure 3.4: **Without astrocytes ($J_{AE} = J_{AI} = 0$ mV, $J_{IA} = J_{EA} = 0$ mV), the stochastic spiking network of subsubsection 3.2.2.2 is in a silent state.** (A) Membrane voltages of two randomly chosen cells, one excitatory (*red*) neuron, one inhibitory (*blue*) neuron, as well as the average AHP current (*black*). (B) The spike rastergram that locates with points the spike times of a randomly-chosen subset of the neurons (one neuron = one row), and (C) the corresponding mean population rates are shown using the same color-code. The short initial burst of activity is due to the initial conditions where every cell is initiated randomly between its resting potential and the spiking threshold. $N_E = 4,000$ excitatory neurons, $N_I = 1000$ inhibitory neurons. Other parameters given in Table 3.2.

Adding gliotransmission between astrocytes and neurons strongly affects the dynamics (figure 3.5): periods of nearly complete neuronal silence now spontaneously switch to periods of high collective neuronal firing, during which roughly all neurons fire on the order of 2 to 15 spikes. The raster plot of figure 3.5B also suggests the factors that trigger Down-to-Up transitions: Up states are systematically initiated by a strong firing activity in the subset of excitatory neurons that are contacted by the astrocytes (neurons numbers 50 to 70 in the raster plot). This first wave of excitation then is transmitted to the whole populations of neurons (E and I), thus forming an Up state.

Hence, our biophysical model of stochastic spiking neurons confirms that astrocyte activity can switch the neuronal network from silent to Up-Down dynamics. During the Up states, the mean population firing rate of the spiking network is similar to te one exhibited by the firing rate model, i.e. around 10 Hz for inhibitory neurons and 5 Hz for excitatory ones (compare figure 3.5C with figure 3.2B), confirming the good match between the rate and spiking models despite the dissimilarity of their spatiotemporal scales. The distributions of the duration of the Up and Down states are estimated in figure 3.5D. For Down states the distributions is peaked around 0.5 seconds whereas it is much broader for Up states, with a large part of the durations comprised between 0.5 and 1.3 seconds. On average, the Down states are twice shorter than the Up states: 459 ± 336 ms for the Down states *versus* $1,031 \pm 575$ ms for the Up.

However, unlike the neurons that collectively synchronize their firing as successive Up and Down phases, the rate of gliotransmission events by astrocytes does not exhibit strong evidence of alternation between distinct activity phases (figure 3.5, *green*). The membrane potential of the individual neurons is strongly bimodal, fluctuating around a lower mean value during Down phases and around

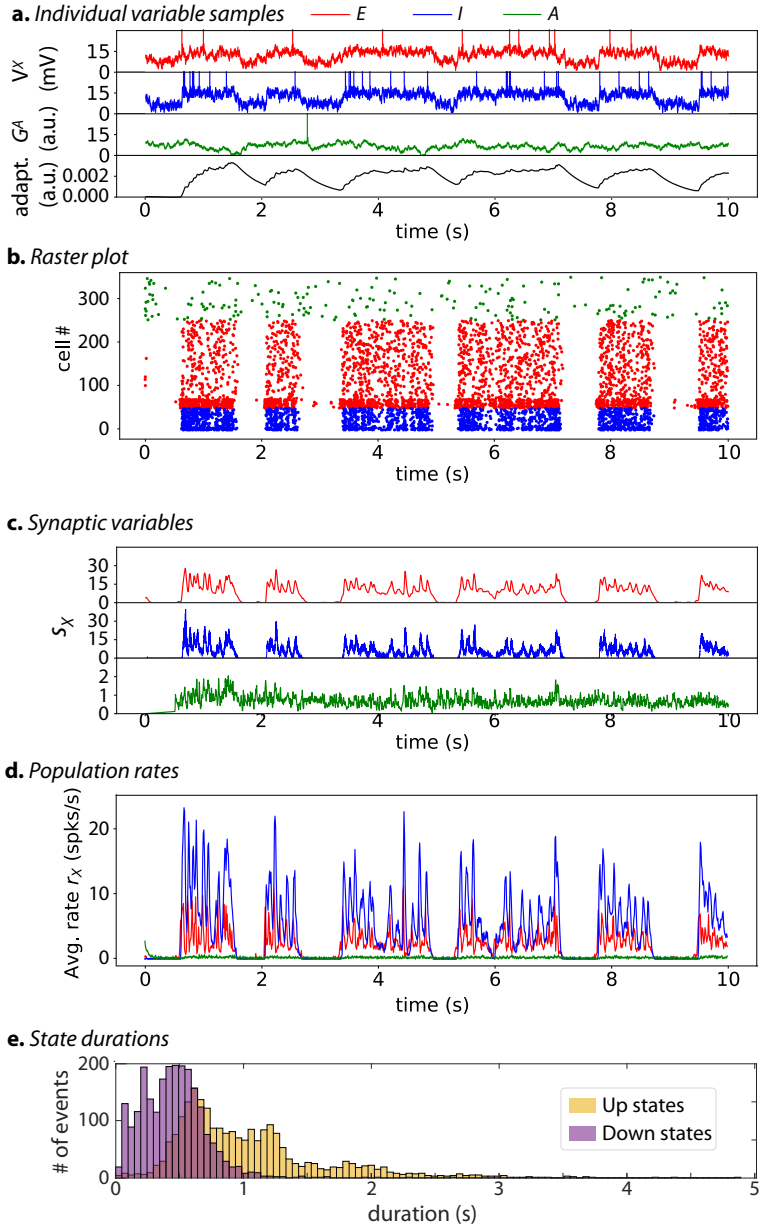

Figure 3.5: **With astrocytes, ($J_{AE} > 0$ mV, $J_{AI} > 0$ mV), the stochastic spiking network switches to a Up-Down dynamic regime.** (A) Membrane voltages of three randomly chosen cells, one excitatory (*red*) neuron, one inhibitory (*blue*) neuron and the astrocyte (*green*) as well as the average AHP current (*black*). (B) The spike rastergram, (C) corresponding synaptic variables s_X and (D) mean population rates are shown with the same color-code. (E) Distribution of Up (orange) and Down (purple) state durations for E and I cells (based on 200 independent simulations of 20 sec each, resulting in a total of 2273 Up states and 2356 Down). For each simulation, $N_E = 4000$ excitatory neurons, $N_I = 1000$ inhibitory neurons and $N_A = 2000$ astrocytes. Other parameters given in Table 3.2. For readability, the first phase of the simulation, characterized by a short very active up state, was discarded.

a larger mean during Up phases, on top of which spikes are emitted (figure 3.5A, *blue, red*). In strong contrast, the dynamics of the gliotransmitter release variables G_i^A is devoid of such alternations, rather appearing to fluctuate around a single, stationary mean (figure 3.5A, *green*). This opposition is also visible in the raster plot (figure 3.5B): the neuronal spikes are strongly synchronized and their presence almost totally restricted to the Up phases, whereas the astrocytic gliotransmitter release events are emitted at an intermediate frequency, but with no clear variation of frequency between Up and Down phases. The evolution of the population synaptic variables, the s_Xs of equations (1.29) (1.30) (3.22), provides another evidence that the neuronal and astrocytic dynamics are different (figure 3.5C): the astrocytic variable s_A (*green*) fluctuates around a low but constant

mean, independently of the Up and Down phases of the neurons that strongly condition the neuronal synaptic variables s_E (*red*) and s_I (*blue*). Of course, the reason why the astrocytic release events are hardly synchronized along the Up and Down phases contrarily to the spiking activity of the neuronal populations is the difference of timescales for information transmission in those cells: on the order of millseconds for neurons versus seconds for astrocytes (the $d^X_{\min}$ and $d^X_{\max}$ of Table 3.2).

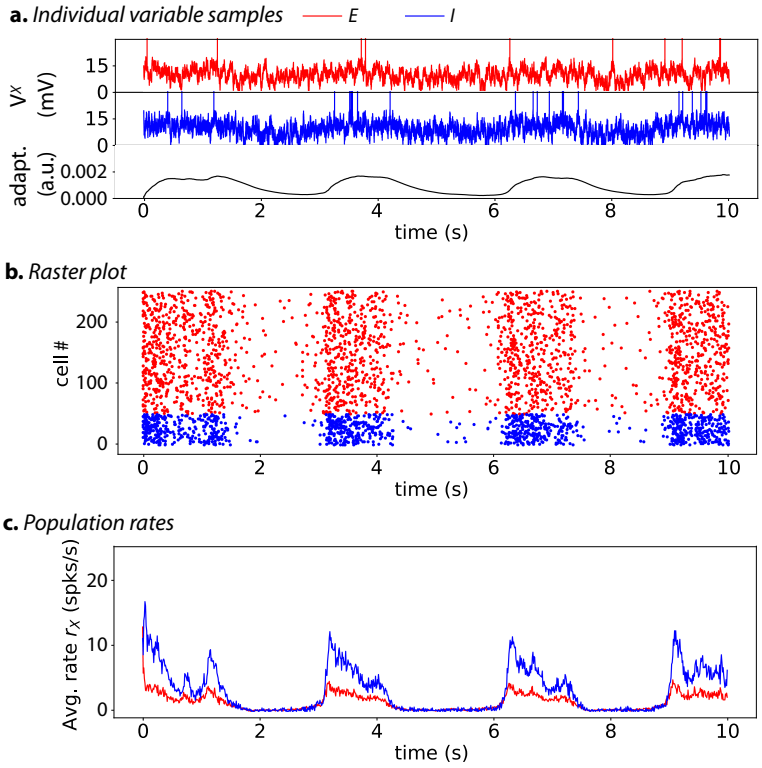

Figure 3.6: **Without astrocytes ($J_{AE} = J_{AI} = 0$ mV, $J_{IA} = J_{EA} = 0$ mV) but with large amplitude of the stochastic external input (σ_X =5 mV), the stochastic spiking network of subsubsection 3.2.2.2 exhibits spontaneous transitions between Up and Down states, i.e. an Up-Down regime.** However the difference between the phases is less marked than the dynamics observed with astrocytes. (A) Membrane voltages of two randomly chosen cells, one excitatory (*red*) neuron, one inhibitory (*blue*) neuron, as well as the average AHP current (*black*). (B) The spike rastergram and (C) the corresponding mean population rates are shown using the same color-code. All parameters are identical to those of figure 3.4, except for the amplitude of the noise to the neurons $\sigma_E = \sigma_I = 5$ mV. $N_E = 4000$ excitatory neurons, $N_I = 1000$ inhibitory neurons.

Therefore, in the simulations of figure 3.5, astrocytes provide the neurons with a constant, basal level of gliotransmission events that fuels their spontaneous collective alternation between Up and Down firing phases. Nevertheless, this background stochastic level of astrocytic input to the neurons is more than an additional random external input to the neurons. To show this, we went back to the spiking model without astrocytes of figure 3.4 and increased the random external input to the neurons. Figure 3.4 showed that the network is silent with the default value of the standard deviation of the random external input noise, σ_X= 3 mV (table 3.2). Increasing σ_X to 5 mV does give rise to an Up-Down regime with spontaneous alternation of Up and Down phases (figure 3.6). However, the difference between the resulting Up and Down phases is much less marked than in the Up-Down regimes with astrocytes: the subliminal individual membrane voltages are nomore clearly bimodal (figure 3.6A), and the difference between firing rates in Up and Down phases is much lower, with a significant firing activity during Down phases (figure 3.6B,C).

Moreover, the range of external input amplitudes that give rise to Up-Down regimes without astrocytes is much more narrow than with astrocytes. Mean-field fixed-point and linear stability analysis of the stochastic spiking network model is shown in figure 3.7 (see subsubsection 3.2.2.2). Two bifurcation diagrams are compared: in figure 3.7a, astrocytes are absent, like in the simulations of figure 3.4, whereas figure 3.7b shows the same diagram when astrocytes are present, like in figure 3.5. These bifurcation diagrams show the evolution of the fixed points and their stability when one varies

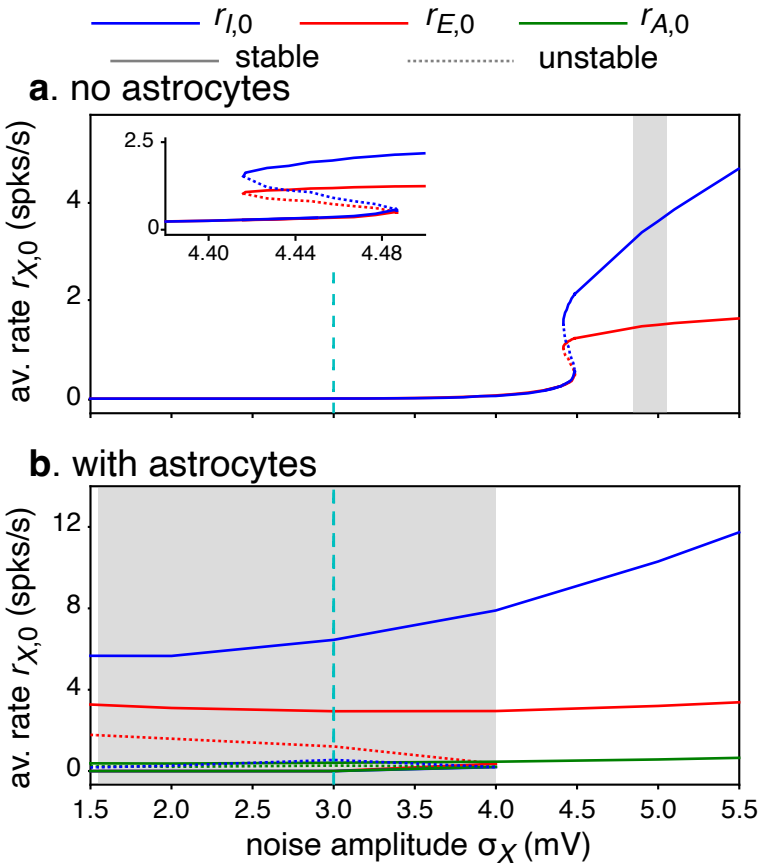

Figure 3.7: **Linear stability analysis of the spiking network model.** (A) Without or (B) with astrocytes along the intensity of the noisy external input to the neurons σ_X. In both cases, a bistable region is observed, ended by a saddle-node bifurcation for large σ_X. However, the bistable region is drastically reduced in the absence of astrocytes, as evidenced by the width of the gray-shaded region, that locates the range of σ_X values for which Up-Down regimes are observed in numerical simulations of the network. These bifurcation diagrams show the evolution of the stable (solid lines) and unstable (dotted lines) fixed points of the equilibrium rates $r_{E,0}$ (*red*), $r_{I,0}$ (*blue*) and $r_{A,0}$ (*green*). In (A), the insets show a zoom out around the bistability region without astrocytes. See subsubsection 3.2.2.2 for details on linear stability analysis. The dashed cyan vertical line indicates the β value used for numerical simulations in figure 3.4 and figure 3.5. Other parameters are given in Table 3.2. Note in particular that the diagram was obtained using $\sigma_E = \sigma_I \equiv \sigma_X$ and keeping a constant $\sigma_A = 3$.

the amplitude of the external noisy input, i.e. the standard deviation of the stochastic input to the E and I neurons, σ_X. Without astrocytes, the diagram shows a stable fixed-point corresponding to a low firing rate for low σ_X values and a second stable fixed-point yielding a larger firing rate at large σ_X values. In a narrow range of σ_X values ($[4.4, 4.5]$ mV), the two stable fixed points co-exist, together with a third intermediate unstable one (dashed line), thus evidencing a region of bistable dynamics (magnified in the inset). We also indicate with a gray-shaded region the parameter range where simulations of the spiking model evidence spontaneous transitions between Up and Down phases (like in figure 3.6). The prediction of the mean-field analysis is not very precise regarding the location of the bistability region, which is probably a finite-size effect related to the finite number of neurons and astrocytes in the simulations. However, the theoretical analysis agrees very well with the narrowness of the bistability region observed in simulations, which confirmes that noise-induced Up-Down regimes with the parameter values of Table 3.2 are observed only for a limited range of input intensities in the absence of astrocytes. In particular, this range is very far from the value $\sigma_X = 3$ mV used in the previous simulations, explaining the silent state figure 3.4.

Astrocytes modify the bifurcation diagram (figure 3.7B): the values of the firing rates of the neurons in the Up and Down stable fixed-point are roughly the same as without astrocytes, but the range of σ_X values for which bistability and Up-Down regimes are observed is incomparably larger, extending

to much lower values. In particular, the bistability region now includes the value $\sigma_X = 3$ mV, thus the Up-Down regime observed in figure 3.4. Note also that the bifurcation analysis predicts that the rate of emission of gliotransmission events by the astrocytes should be very similar either in the Up or the Down state, in strong opposition to the neuronal firing rates. This explains the observation that the gliotransmission emission rate in figure 3.5 did not vary much between Up and Down phases: all variables do follow the bistable dynamics of the whole system, but the branches of stable fixed-points for the astrocytes are much closer to each other than those for the neuronal firing rates.

Hence, as for the firing rate model studied in subsubsection 3.2.3.1 above, adding astrocytes in the spiking model does not drastically alter the nature or number of bifurcations, but relocates the bistability region in the parameter space so that a point in the parameter space that is out of the bistability region without astrocytes can find itself inside the bistability region by the addition of astrocytes, thus exhibiting Up-Down regime.

As a final remark, all the above results were obtained with $J_{AI} > 0$, i.e. a scenario where the firing activity of the inhibitory neurons directly increases the probability of gliotransmitter release by the astrocytes. However, we checked that the absence of this specific interaction does not jeopardize the validity of our conclusions here. We show in figure 3.8 the results obtained with the rate model (figure 3.8A) or the spiking network model (figure 3.8B) when the strength of I $\rightarrow$ A interactions vanishes ($J_{AI} = 0$), while keeping all the other parameters as in Table 3.1 or Table 3.2. This figure evidences a handful of changes compared to the scenario $J_{AI} > 0$ illustrated above, but the simulation results are still very similar (compare figure 3.8A with figure 3.3 with or figure 3.8B with figure 3.5), so that the conclusions drawn above are still valid in the absence of I $\rightarrow$ A interactions.

3.2.4 Discussion

Up-Down cortical dynamics have primarily been observed during sleep or anesthesia. However, similar dynamical regimes have also been reported in the cortex during quiet wakefulness [188, 151] or during a task [200, 69]. Therefore making sense of these dynamics is important for our understanding of brain operations in general, not only during sleep or anesthesia. The cellular mechanisms that support the emergence of spontaneous Up to Down and Down to Up transitions in the cortex are however still unclear. The hypothesis that these transitions could be controlled by a mechanism intrinsic to the neurons of the considered cortical region has been explored by a number of theoretical or computational studies [20, 50, 108, 24]. However recent experimental studies reported the implication of other types of intrinsic brain cells, in particular astrocytes [190, 189, 202].

These results motivated us to propose our rate model equations (1.53) to (1.55) and (3.1) (3.2). The main novelties here are *i*) to introduce the impacts of astrocytes in the dynamics of neuronal networks in the Up-Down regime and *ii*) to account for the influence of astrocytes using a rate equation with a similar mathematical structure as the firing rate equation of the neurons. Modelling the gliotransmitter release activity of astrocytes using a rate equation similar to the firing rate equation of the neurons enabled us to preserve the mathematical tractability of the model. We acknowledge that using equation (3.1) or equation (3.21) is a strongly simplified modelling of gliotransmission. However, it has the advantage of preserving the main biological ingredients of gliotransmission while keeping the model simple enough for the analytical study of its stability. We believe that the possibility to rely simulation results on an underlying sound theoretical analysis was important for the present article, and this is the reason why we have chosen to keep these population synapses.

In our numerical simulations, the addition of gliotransmission from astrocytes was sufficient to transform a neural network prepared in the Down, silent state into a dynamical regime of spontaneous alternations between Up and Down states. The inclusion of astrocytes in our model therefore provided us with the opportunity to explore how astrocytes alter the dynamics of the neuronal firing rates in a way that switches them to the Up-Down alternation regime. A major conclusion from our model is that gliotransmission probably does not have a drastic effect on the underlying dynamics of the network. Adding gliotransmission does not modify the number nor the type of the observed bifurcations, it only alters the values of the parameters at which these bifurcations occur. As a result, gliotransmission can transform a silent neural network model into a network exhibiting Up-Down dynamics, with no change of the neuron-related parameters, and no alterations of the neural mechanisms that control the transitions between Up and Down phases. Moreover, our model suggests that the fundamental differences of signal integration in neurons versus astrocytes may

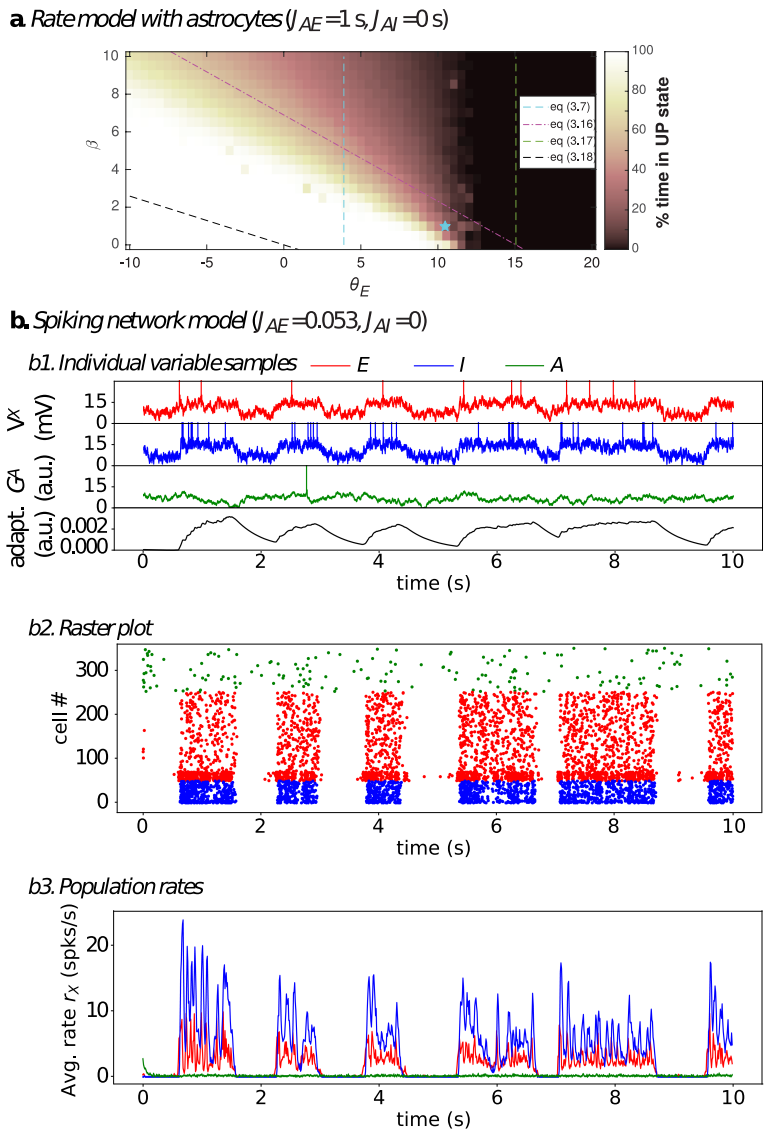

Figure 3.8: Results of the rate model of equations (1.53) to (1.55) and (3.1) (3.2) (A) or the spiking network model of equations (3.19) to (3.22), and (1.29) to (1.31) (B) obtained in the presence of astrocytes, but with $J_{AI} = 0$ mV, i.e. with no direct effect of inhibitory neurons on astrocytic gliotransmitter release. All parameters were as indicated in Table 3.1 or Table 3.2, except for the value of J_{AI} that was set to 0. Refer to figure 3.3C and figure 3.5 for the color-codes and parameters of panels (A) and (B), respectively.

be crucial in the emergence of Up-Down regimes. In particular, the signaling delay in our spiking network model was kept three orders of magnitude larger in astrocytes compared to neurons, i.e. seconds versus milliseconds. This difference of timescales turned out to be crucial for the network dynamics illustrated in figure 3.5 where a stationary background of astrocytic gliotransmission events triggers spontaneous transitions between synchronized Up and Down phases of neuronal firing.

The main limitation of our models are the simplification assumptions that we made to express the impact of astrocytes on the neural network model. The modelling literature proposes mathematical descriptions of the process of gliotransmitter release from astrocytes that are much more complex or accurate than the simple phenomenological expressions used here, see e.g., [61] for a recent account. However the price to pay for the added complexity would be a restriction of the available mathematical understanding of the system dynamics. Future numerical simulation works will be needed to assess whether the inclusion of such more complex descriptions comes with changes of the main conclusions of the present study. We also adopted the modelling choice made by [116] for their spiking model where the synapse dynamics are modelled using a single population variable, integrating the spikes emitted by the whole population into a single variable that can then be fedback to the other cells. This choice limits the range of modelling exploration regarding connectivity. It

forbids models where the inputs received by an astrocyte is restricted to a subset of the neurons or, conversely, those where gliotransmission from an astrocyte targets only a subset of the synapses of a neuron. On the other hand, though, this modelling choice greatly facilitates theoretical (mean-field) analysis of the stochastic network model. We leave for future works the study of models that would incorporate the main ingredients of our models above, but with real individual synapses and / or more realistic sparse neuron-neuron connectivity [219]. This would make it possible to associate a spatial embedding to the network thus enabling the study of slow wave propagation [42] or to compare Up-Down regimes during sleep with those observed during anasthesia [224].

Experimental reports indicate that astrocytes form roughly 20 to 40 % of all glial cells [230]. On the other hand, estimates of the ratio between glial cells and neurons in human cortex varies from 1.5 to more than 2 in humans [230]. Altogether, those numbers yield an astrocyte:neuron number ratio in the human cortex that ranges from 1:3 to 1:1. The numbers chosen for our simulations of the spiking network model are in good agreement with these experimental reports, with an astrocyte:neuron number ratio of 1:2.5. Additional comparisons can be made with the in vivo experiments reported in [116] from multichannel silicon microelectrode recordings in the somatosensory cortex of urethane-anesthetized rats. As explained in subsubsection 3.2.2.3, we have set parameter values so that the model simulations exhibit behaviors similar to the experiments of [116]. We now give a more detailed account of the match between model and data. The distributions of Up or Down phase duration in the experiment shown in figure 2A of [116] are broad, with Down phases lasting from less than 100 ms to 1.5 s and Up phases reaching larger maximal values, up to 2 s. Our simulation results exhibit similar broad distributions, at least for Up states, a consequence of the large variability of the Up state durations (figure 3.5D). The coefficient of variations from the in vivo experiment of figure 2A [116] were 0.61 and 0.70, for Up and Down phases, respectively, to be compared with 0.56 and 0.73 for our simulations. The mean values of the phase durations are also very well replicated by our simulations: 1.03 and 0.46 s for Up and Down phases, respectively, vs 0.65 and 0.38 in the experiment of [116], figure 2A. The instantaneous population rate during Up phases in these in vivo experiments is around 4 to 6 Hz in [116] (their Figure 1C), a value that is similar to the population rate of excitatory neurons in our simulations (figure 3.5D). Taken together, we thus conclude from those quantitative comparisons that our simulation results exhibit Up and Down phases that agree well with available experimental data.

The main experimentally-testable prediction made by our work is arguably the possibility of a dynamical regime where the astrocytic gliotransmitter release events are only weakly synchronized to the succession of Up and Down phases of the neuron firing state. In this regime the population frequency of gliotransmitter release events does not change much in Up phases compared to Down phases. Experimental testing of this prediction would consist in measuring simultaneously the activity of a local population of neurons using e.g., multi-channel silicon microelectrodes while monitoring the gliotransmitter events from astrocytes from the same local area. Gliotransmitter release events are difficult to monitor experimentally, even with glutamate-sensitive fluorescent reporters (see e.g., fig. 7D in [190]). Monitoring intracellular calcium activity could constitute a good proxy to locate glutamate release events by astrocytes. However, recent experimental studies have challenged the relation between calcium signals recorded from astrocyte cell bodies from those initiated in the fine processes, that are expected to contact the synapses [199, 211, 28]. Therefore, experimental testing of the above dynamical regime would probably need the measure of local calcium signals, within the fine astrocyte processes that form the so-called "gliapil". At any rate, this predicted dynamical regime is supported by activity-dependent release of gliotransmitters by astrocytes, which existence and impact on the neurons in physiological conditions is still debated among experimental neuroscientists [204, 76]. Therefore, according to the work presented here, experimental observation of astrocytes releasing gliotransmitters at a roughly constant rate while neurons undergo successive Up and Down firing phases, should be interpreted as an argument in favor of the existence of gliotransmission, and not against it.

Synchronized neural activities are important characteristics for an healthy brain function, which occur within a wide range of spatiotemporal scales. But anormal synchronized behaviours can be observed in some neurological disorders [118].

3.3 How are astrocytes involved in epileptic seizures?

3.3.1 Epileptic seizures could result from impaired network synchronization linked with astrocytic dysfunctions

One of the main disorders in which altered neuronal interactions play a crucial role is epilepsy. This disease is characterized by the presence of regular and unpredictable seizures [206]. A seizure is defined as a "transient of signs and/or symptoms due to abnormal excessive or synchronous neuronal activity in the brain" [79].

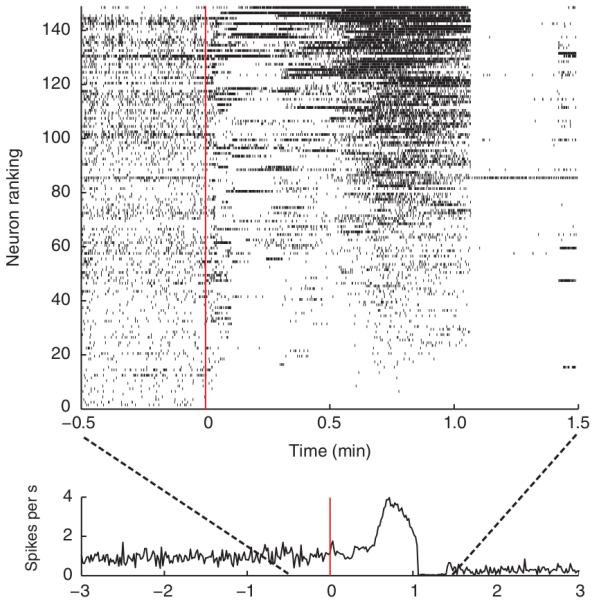

Figure 3.9: Example of a recorded seizure: spike rastergram and the corresponding mean firing rate, adapted from Truccolo et al. (2011) [226]. **(A)** Rastergram. Neurons are vertically sorted according to their mean firing rate during the seizure. Neural firing rates become more synchronized at the end of the seizure. Its termination happens abruptly, and is followed by a long silent period (around 20 s). **(B)** The mean firing rate is stationary before the seizure onset, then rise significantly.

Figure 3.9 presents an example of an experimental recording (rastergram and mean spike rate) of a seizure. It is interesting to note that desynchronization has been observed before the onset of seizures or shortly after, and high levels of synchronization were recorded at the end of seizures (which could induce or facilitate the termination) [118].

Within this network synchronization perpsective, a particular attention has been paid to coexisting synchronous and asynchronous oscillations in networks of identical coupled oscillators, named chimera states [13, 155, 25]. It has been shown that these chimera states could coalesce into a globally synchronous motion in finite size networks [242, 139]. This process has been suggested to be a possible mechanism for the onset of the seizure, but it is still unclear what causes this rapid collapse.

Among the different factors that could be responsible for the synchronization behaviour alteration in seizures, it appears that astrocyte dysfunctions could play a role. Indeed astrocyte alterations in K+ buffering, astrocyte immune responses, gap junctions, glutamate uptake, or astrocyte signaling have all been suggested to be linked with human or experimental epilepsy [206, 55, 184]. This latter effect is studied in this chapter to investigate another aspect of modulation by astrocytes of neural synchronization.

Indeed, we have seen in section 3.2 that neurons and astrocytes can interact in particular through bidirectional glutamate exchanges, which has for consequence that astrocytes can modulate the neuronal activity synchronization. Therefore, dysfunctions in that signalling system could make the neuron-astrocyte network more excitated, which may perturbate neuronal synchronization and favor seizures.

Here we propose a neuron-astrocyte network with a modular connectivity, adapted from our precedent work. The organization of cells in clusters is here considered to be in more accordance with biological reality and to take into account that a seizure could be a collapse of activity patterns.
A small-world like network has also been developed, its results will be briefly presented as they do not display any seizure-like event. However, they represent an interesting extension to the former study of Up-Down dynamics modulation.

3.3.2 Modular and small-world connectivity

The integrate-and-fire model described in the previous section 3.2 had no spatial structure, the synaptic connections were described as mean synapses (i.e. a single synaptic variable s_X for all cells in the population X). In addition to facilitate analytical analysis, this feature allowed to strongly decrease computational costs. But in the context of spatially-explicit neuron positions, this modelling option cannot be used and we had to employ individual synapses (i.e. one synaptic variable $s_{X,i}$ per neuron). Since this came with a huge increase in computational costs, we coded the model in C++ using parallel computing in collaboration with Jonathan Rouzaud-Cornabas. This optimized code allowed us to simulate large networks with discrete synapses.
The synaptic variables $s_{X,i}$ and $u_{X,i}$ are now unique for each post-synaptic cell.

$$\tau_r^X \frac{du_{X,i}}{dt} = -u_{X,i} + \underline{\tau_X} \sum_k \sum_{j=1}^{N_X} C_{ij}^{XY} \delta(t - t_j^k - d_j^k) \tag{3.35}$$

$$\tau_d^X \frac{ds_{X,i}}{dt} = -s_{X,i} + u_{X,i} \tag{3.36}$$

For $i \in \{1, ..., N_X\}$.
The structure is defined by the connectivity matrices C^{XY}. Clusters of cells with equal sizes are defined, with connections between cells within a cluster, between neighbour clusters (inter-cluster local connection) and remote ones (shortcuts). To build the 9 connectivity matrices between the 3 populations (E, I and A cells), we begin to build a ring lattice on which cells are arranged following a recurrent pattern, see figure 3.10. For a cell labeled i, with i from 0 to $N-1$, the value i mod 7 determines which type of cell it is. The following algorithm is applied to this lattice:

1. Construct a regular ring lattice, with N nodes, each node labeled $i \in 0 \dots N-1$.
   If (i mod 7 = 1, 2, 5 or 6), then i defines an E cell (notation $i \in E$)
   If (i mod 7 = 0), then i defines an I cell (notation $i \in I$)
   If (i mod 7 = 3 or 4), then i defines an A cell (notation $i \in A$)

2. Construct a graph where each node is connected to K neighbours, $K/2$ on each side. That is, there is an edge (i, j) if and only if [234],

$$0 < |i - j| \bmod \left(N - 1 - \frac{K}{2}\right) \leq \frac{K}{2} \tag{3.37}$$

   If $i \in A$ and $j \in A$, then $K = K_A$
   If ($i \notin A$ and $j \in A$) or ($i \in A$ and $j \notin A$),

      If i mod 10 = 0, then $K = K_{NA}$

      Else $K = 0$

   Else $K = K_N$

3. Construct the clusters. For p from 0 to D,

      If ($i \in A$ and $j \notin A$), then for each i there is a connection with all j cells between $Np/D + N/(2D)$ and $N(p+1)/D$

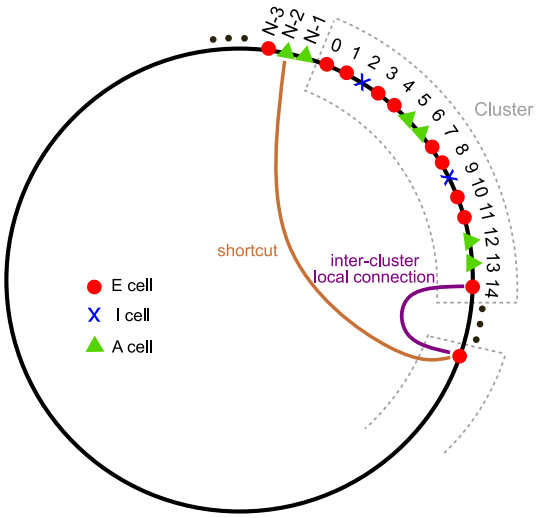

Figure 3.10: Schematic plot of the network structure. The nodes (cells) are numbered from 0 to N-1, and their number determines to which population they belong, excitatory neurons (E), inhibitory neurons (I) or astrocytes (A). See more details of these rules in the text. Cells are organized in clusters with connections within a cluster, between adjacent clusters, and shortcuts connecting remote ones. Each element of the network is defined in a different step of the algorithm, indicated in brackets.

If ($i \notin A$ and $j \in A$), then no connections

Else for each i there is a connection with all j cells between Np/D and $N(p+1)/D$

4. For every node $i = 0, \ldots, N-1$ take every connection, and rewire it with probability β_{rw}. Rewiring is done by replacing (i, j) with (i, k) where k is chosen uniformly at random from all possible nodes.

Afterwards, connectivity matrices C^{XY} are extracted, see figure 3.11.
The complexity of this algorithm is due to the mix between different topological components (small-world part to connect neighbour cells in step 2, clusters in step 3, and rewiring in step 4), as well as the different interactions between the three cell populations, defined in step 1. Indeed the relative number of connections and the connectivity rules between the populations are computed so that the properties of the original spiking model presented in section 3.2 are preserved. Before rewiring:

- within a cluster, apart from recurrent connections, there is a full connectivity for neuron-to-neuron connections and for astrocyte-to-astrocyte connections (step 3, third condition).
- The inter-cluster local connections between neurons (step 2 with $K = K_N$) concerns a small number of connections, see figure 3.11, so that it represents a negligible variation in the mean number of connections per neuron.
- only a fraction (10%) of the E or I neurons are subjected to gliotransmission from the nearest astrocytes (step 2 with $K = K_{NA}$), uniformely distributed across clusters.
- 50 % of the astrocytes in each cluster receive inputs from the E or I neurons of the same cluster (step 3, if $i \in A$ and $j \notin A$).

Finally, the rewiring process preserves the total number of connections (step 4).

The introduction of this topology represents the main modification of the original model (see section 3.2). But some modifications in individual cell dynamics have also been introduced, see table 3.3. First, J_{XY} have been rescaled to maintain the properties of the dynamics with the smaller number of connections per neuron in this model. Furthermore, J_{AE} value was a bit increased compared to the rescaled value. The increase of astrocyte inputs strength enhances the general excitability of the system, which may lead to a seizure-like event.
Moreover, the after hyperpolarization current was removed ($\kappa_a = 0$). Since interestingly it appeared to be unnecessary to induce Up to Down transitions in the modular network, we decided for simplification purposes to study the model behaviour without adaptation. The effect of adaptation in

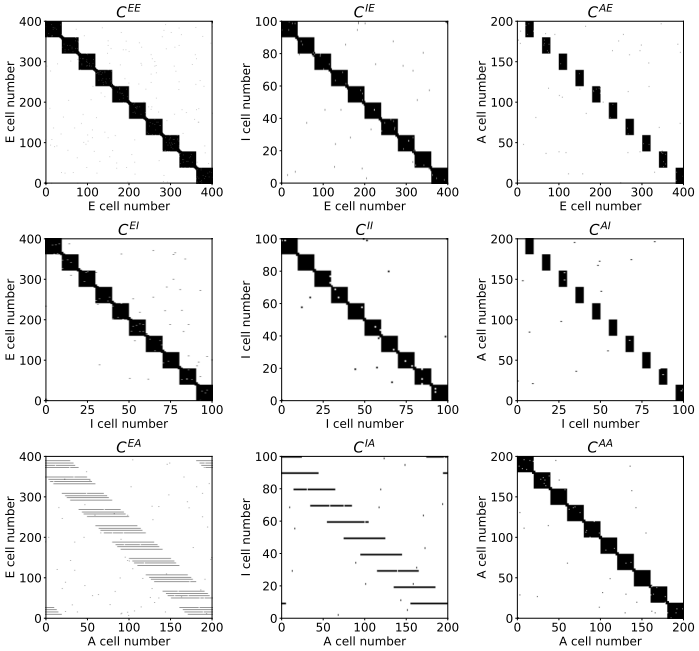

Figure 3.11: Connectivity matrices C^{XY} between all populations. The network is organized in 10 clusters with connections between neighbour clusters and shortcuts conneting remote clusters. The proportions of connections between cell populations of the former section 3.2 have been preserved. Neurons are almost all connected inside a cluster, and astrocytes receive inputs from half the neurons in their cluster, while they contact 10% of the neurons.

this network would need to be further characterized in the future.

The initial conditions for astrocyte gliotransmitter release were fixed lower than the mean, that is instead of $G_i^A = G_L^A + (G_{th} - G_r)\eta_i$, it is

$$G_i^A = G_L^A + \frac{3}{4}(G_{th} - G_r)\eta_i \tag{3.38}$$

With η_i a random value with a uniform distribution between 0 and 1.
These initial conditions were chosen to study the impact of a possible increase of astrocytes excitation (from the under-excitated initial conditions to a mean value) on the overall dynamics. To observe the transient dynamics before the transition towards a more excitated state (see figure 3.13), the maximal transmission delay of astrocyte was extended (from 1.5 s to 3 s).

Comparison with a small-world network To study whether a transition to a seizure-like event could emerge for different networks, a small-world like topology was examined. The resulting connectivity matrices (see figure 3.12) were obtained using an algorithm similar to the one previously described.

As for the modular network, some modifications in individual cell dynamics have been introduced for the synaptic weights J_{XY}, the after hyperpolarization current has been removed and the maximal delay transmission for astrocyte has been extended, see table 3.4. The initial conditions for astrocyte gliotransmitter release were also fixed lower than the mean, see equation (3.38).

3.3.3 Modular excitatory, inhibitory neuron and astrocyte network exhibits spontaneous seizure-like events, contrary to the small-world network

The separation of the model into segragated clusters induces localized patterns of neural Up-Down activity, see the rastergram in figure 3.13 (A) before $t = 7.5$ s. We can observe a synchronization between the pattern of different clusters, some can be in a concomitant Up or Down phase at the

Table 3.3: **Parameters used for the modular spiking model which differ from those used in the model of section 3.2 or have been introduced**

Parameter	Value	Definition
J_{EE}	140 mV	strength, E $\rightarrow$ E
J_{EI}	-140 mV	strength, I $\rightarrow$ E
J_{IE}	125 mV	strength, E $\rightarrow$ I
J_{II}	-100 mV	strength, I $\rightarrow$ I
J_{AE}	8	strength, E $\rightarrow$ A
J_{EA}	220 mV	strength, A $\rightarrow$ E
J_{AI}	5.8	strength, I $\rightarrow$ A
J_{IA}	44 mV	strength, A $\rightarrow$ I
J_{AA}	16	strength, A $\rightarrow$ A
κ_a	0	strength, adaptation
$d^A_{\max}$	3 s	max. delay, A
K_N	20	Mean degree for neurons receiving neuron connections
K_A	20	Mean degree for astrocytes receiving astrocyte connections
K_{NA}	175	Mean degree for neurons receiving astrocyte connections
β_{rw}	0.01	Rewiring parameter

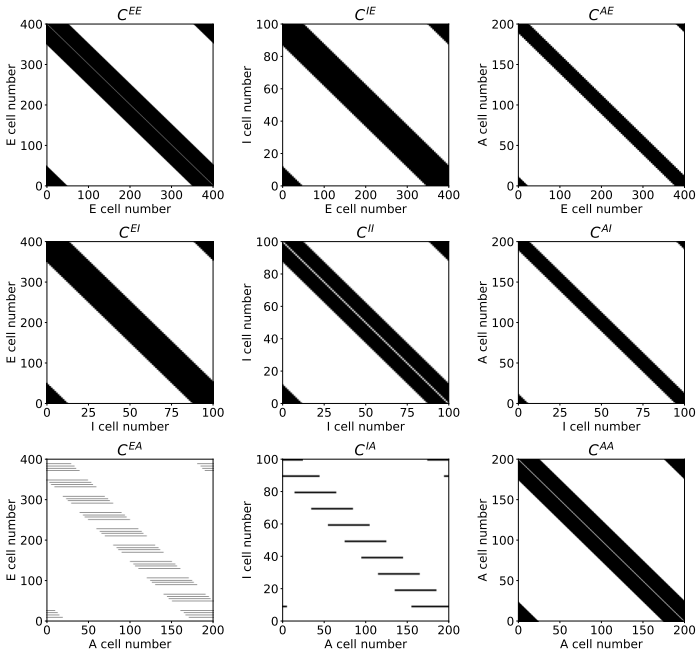

Figure 3.12: Connectivity matrices C^{XY} between all populations for a small-world like organization for neurons. Cells are connected with their nearest neighbors and a few shortcuts connect remote cells. The proportions of connections between cell populations of the former section have been preserved.

same time. Unlike the neurons, the rate of gliotransmission events by astrocytes does not exhibit strong evidence of alternation between distinct activity phases, as in the previous section 3.2.
An interesting phenomenon occurs around $t = 7.5$ s. We observe a generalized silent period of approximately 1 s for all neural clusters. Afterthat, some neural areas began to spike heavily, which is then followed by an important rise in gliotransmission. After this seizure-like onset, we can observe more neural and astrocyte areas being " recruited" in this excessive firing. This effect is well seen on the mean population rates, see figure 3.13 (B), after the silent period and the onset around $t = 7.5$ s, the mean rate in each cell population increases progressively.

This transition would be due to a slight increase in the astrocyte gliotransmitter release, since initial conditions were fixed lower than the mean.
Without astrocytes, the neural network remains in a silent state (figure not represented here).

Table 3.4: **Parameters used for the small-world like spiking model which differ from those used in the model of section 3.2 or have been introduced**

Parameter	Value	Definition
J_{EE}	70 mV	strength, E $\rightarrow$ E
J_{EI}	-70 mV	strength, I $\rightarrow$ E
J_{IE}	62.5 mV	strength, E $\rightarrow$ I
J_{II}	-50 mV	strength, I $\rightarrow$ I
J_{AE}	0.8	strength, E $\rightarrow$ A
J_{EA}	220 mV	strength, A $\rightarrow$ E
J_{AI}	0.58	strength, I $\rightarrow$ A
J_{IA}	44 mV	strength, A $\rightarrow$ I
J_{AA}	1.6	strength, A $\rightarrow$ A
κ_a	0	strength, adaptation
$d^A_{\max}$	3 s	max. delay, A
K_N	180	Mean degree for neurons receiving neuron connections
K_A	85	Mean degree for astrocytes receiving astrocyte connections
K_{NA}	175	Mean degree for neurons receiving astrocyte connections
β_{rw}	0.01	Rewiring parameter

No seizure like-event was observed in a small-world like network Contrary to the dynamics in the modular network, no seizure transition was observed in the small-world like network for similar individual cell parameters, see figure 3.14.
However, the Up-Down dynamics is preserved. While it is less synchronized than in the previous section 3.2, with some kind of spatial segregation in cell activities, it is less clustered than for the modular network (figure 3.13).

3.3.4 Discussion

Over 50 million individuals worldwide suffer epilepsy, the third most prevalent neurological condition. Approximately 30 to 40 percent of epilepsy patients experience drug-resistant seizures, a number that has remained mostly consistent over the past ten years despite major attempts to create new antiepileptic medications [161]. Therefore, further research needs to be carried out to identify the mechanisms underlying seizure generation. Here, I have used a network perspective to approach this phenomenon, in agreement with previous models centered at synchronization dynamics [118] or chimera states collapse [13, 242]. These phenomena may in part be modulated by astrocytes dysfunctions, which have been shown to have a role in the synchronization of neural networks in epilepsy [206, 55, 184]. Studies on the impact of astrocytes alterations in epilepsy could represent new therapeutic perspectives [124].

These observations motivated us to propose a modular neuron-astrocyte network to understand whether astrocytes effect on synchronization could lead to a seizure-like event. This work is still under development but provides first tracks on the link between astrocytes and seizures. We have seen that patterns of Up-Down dynamics arise in a clustered connectivity. After a short period of global silence, this activity can converge into a full-spiking pattern when gliotransmission reaches a certain level, which should be specified in the future.

An important limit of our work is that once a seizure-like event has begun, our network cannot go back to its initial condition. The conditions for seizure termination have indeed been less investigated both experimentally [201, 248, 168] and theoretically [135] than those for the seizure onset. In our model, this termination may maybe occur through astrocyte regulation of synaptic depression and facilitation [62].
But an important future axis of this study would be to add a spatial-dependency to the connectivity, in particular to investigate calcium waves in astrocytes. Indeed it is not clear whether calcium waves could induce seizure-like events [107] or be triggered by them [17].

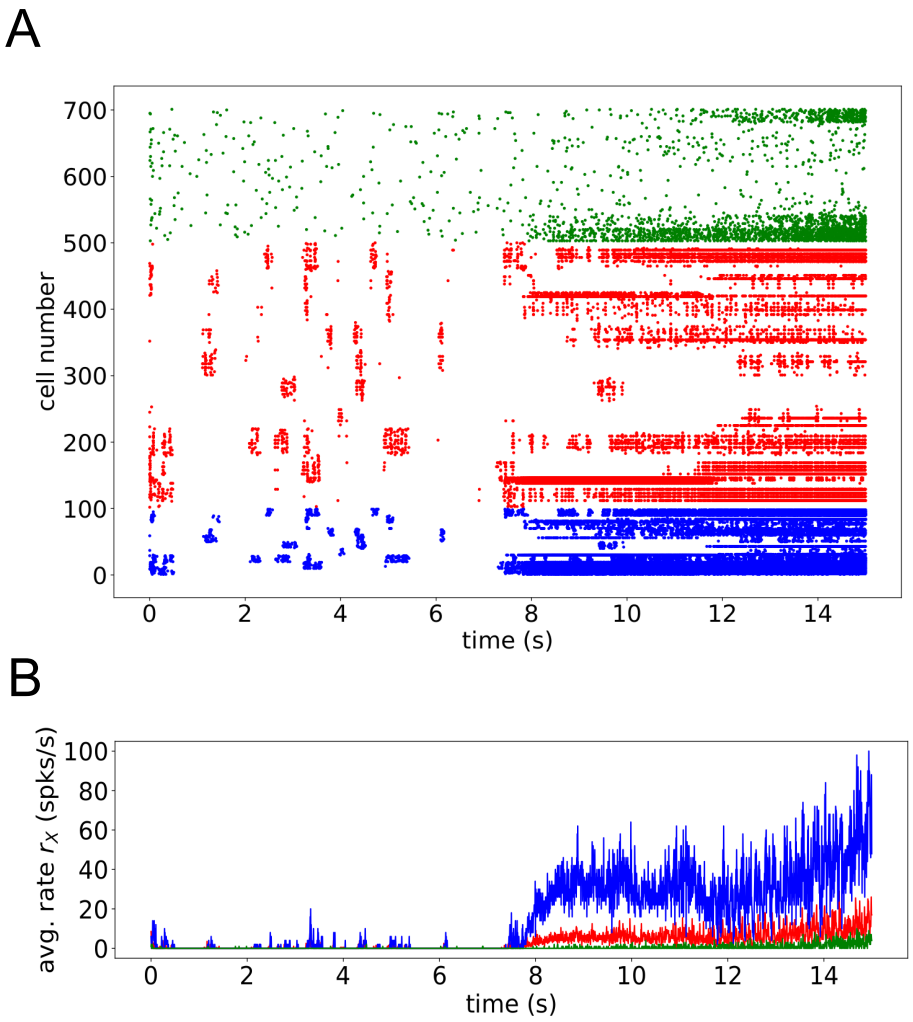

Figure 3.13: Spontaneous coalescence of cluster-activities into a seizure-like event. The initial conditions for astrocyte gliotransmitter release were fixed lower than the mean. **(A)** Spike rastergram with the color code: green for astrocytes, red for excitatory neurons and blue for inhibitory neurons. Before $t = 7.5$ s, we can observe a synchronization between the different clusters, some can be in a same Up or Down phase. Unlike the neurons, the astrocyte activity does not exhibit an Up-Down dynamics (as observed in section 3.2). After $t = 7.5$ s, we observe a global silent short duration, before a massive firing behaviour begins in some cells, for most clusters. **(B)** mean population rates with the same color code. The mean firing increases abruptly after a short silent period, as observed in the rastergram.

3.4 General conclusion

In this chapter we simulated and analyzed an integrate-and-fire and a rate model to study Up-Down dynamics, and the same integrate-and-fire model was adapted in a preliminary study on astrocyte role on seizure-like events in epilepsy. A key element of this framework is the simplicity of the gliotransmission modelling used here, which has the advantage of preserving the main biological ingredients of gliotransmission while keeping the model simple enough for the analytical study of its stability.

We hope that this model could be adapted to explain other types of synchronization behaviour, such as neural oscillations [233, 71]. We wish also to adapt it with a realistic spatial structure, which in particular could allow us to model calcium waves propagation [78]. Another future axis we wish to investigate would be to adapt this model to characterize the mechanisms of action of candidate drugs.

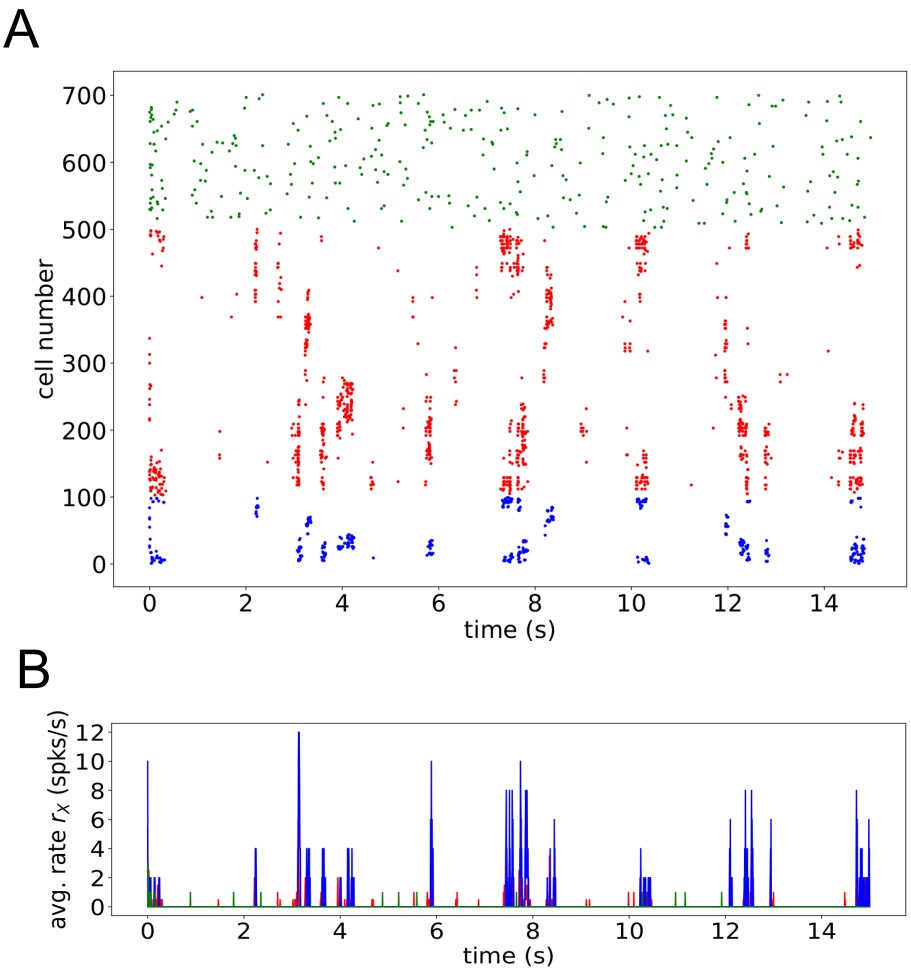

Figure 3.14: Up-Down dynamics in a small-world like network. A global synchronized behaviour can be observed but also some clusters of activity. The initial conditions for astrocyte gliotransmitter release was fixed lower than its mean. **(A)** Spike rastergram, **(B)** mean population rates with the same color code, green for astrocytes, red for excitatory neurons and blue for inhibitory neurons.

We have worked in this chapter with cell networks, but also with rate models. This framework is useful for large populations modelling. We will see in the next chapter another type of spatial continuum model, suitable for tissue-level description.

Chapter 4

Modelling systems memory consolidation with neural fields

4.1 Systems memory in computational cognitive neuroscience

How cognition emerges from biological processes in the brain is a question addressed by cognitive neuroscience. Historically, studies of patients with cognitive impairments induced by brain damages have played a important role in the establishment of the discipline [41].
Important research areas in cognitive neuroscience include higher mental processes, perception, and memory storage. Research in this latter field has for example identified several types of memory, a declarative (explicit) form concerned with facts and events and a procedural (implicit) form concerned with the knowledge about perceptual and motor procedures [7].

When studying memory storage, it is convenient to consider two scales: the molecular problem of memory [123], which investigates how memories are encoded, and the systems problem of memory, which studies where memories are located [171]. This latter category deals with issues such as which neural systems underly procedural memory (amygdala and emotional memory, cerebellum and memory for motor acts, striatum and habits memory), or declarative memory [7]. For the latter an important issue is its dependency to the medial temporal system. Indeed, a key feature of declarative memory is that the medial temporal lobe is involved in memory storage and retrieval for a limited period of time [83].

This phenomenon has been modeled by artificial neural networks (connectionist models) [215, 160, 122, 162, 8, 104, 113], which allowed a greater comprehension of the process. However to our knowledge, in these models, some neurobiological mechanisms that could be pertinent – and which will be discussed in the following section – have been ignored. We tried here to approach this issue with a more biological-grounded modelling framework, by using neural fields. We believe that this type of model could be suitable for systems memory issues. So far, models of neural fields have already been used in computational cognitive neuroscience to study learning and memory in sensory cortices [175], with self-organizing maps [133]. In spite of the fact that the modelling of systems memory organization occurs at a larger spatial scale since it connects different brain areas, we propose to restrict the model to the different representations of a same memory in the different brain areas. The neural field model we propose in this part connects interacting maps of representations.

4.2 A neural field framework to model the standard consolidation theory

The following study is a preprint that will be soon submitted to the Journal of Theoretical Biology: Blum Moyse, L., & Berry, H. (2023). Modelling memory consolidation at a systems level with neural fields. The section below is extracted with a few adaptation from this article.

4.2.1 Introduction to standard consolidation theory and neural fields

4.2.1.1 Standard consolidation theory

Memories are believed to be biologically encoded as physical traces in the brain, or engrams. It is assumed that these engrams are formed through the strengthening of synaptic connections in neuronal ensembles, i.e. populations of neurons involved in a memory representation or a computational task [120]. The process through which recently encoded memories are converted into more stable long-term stored information is referred to as consolidation [130]. This term includes two mechanisms that occur at distinct spatial and time scales; synaptic and systems consolidation. Synaptic consolidation is achieved through fast mechanisms (a few hours), like long-term potentiation (LTP) [159]. The most common form of LTP is qualified as Hebbian, it strengthens synapses between neurons that fire simultaneously, which stabilizes a memory trace. ITDP, which was studied in chapter 2, is an example of a mode of synaptic consolidation. These processes are embodied in the wider changes invoked by systems consolidation. This second type of consolidation describes the gradual reorganization of memory patterns across different brain areas, which can endure weeks, months, or even years [130].

Systems consolidation theories were introduced following neuropsychological observations of memory impairments in patients with medial temporal lobe (MTL) damages. The MTL includes the hippocampus and adjacent neocortical areas (perirhinal, entorhinal, parahippocampal) [216]. These lesions induce anterograde amnesia for declarative memories. Anterograde amnesia refers to the inability to form new memories. This disability concerns in most cases declarative memories, memories that can be consciously recalled [215, 216]. These studies introduced the idea that there exist different memory systems associated with different brain areas. MTL injuries are also responsible for temporally-graded retrograde amnesia for declarative memories. Temporally-graded retrograde amnesia refers to a forgetting of memories encoded in the past, where the loss is more important for recent events. Interestingly the wider the damages were, the more ancient the erased memories were. This amnesia goes from 1-2 years when lesions are restricted to the hippocampus (a part of the MTL), to a situation where all past memories are forgotten when damages include the whole MTL and surrounding cortical regions. These studies indicate that recent declarative memories would initially depend on the MTL, before being transferred to a durable storage place, possibly cortical areas. Since then, many animal studies have examined the impact of hippocampal and cortical lesions on memory [83].

These different studies led Marr to propose the first computational model describing systems consolidation in 1971 [158]. In this model, it is suggested that a new event is quickly encoded in the hippocampus and that with time this memory will be progressively "transferred" to the neocortex, through repetitive replays of the patterns during sleep. Following this pioneering work, several interesting connectionist models have conceptualized the features of the standard consolidation theory and highlighted results coherent with neuropsychological observations [215, 160, 122, 162, 8, 104, 113]. These ideas have led to a contemporary model of systems memory consolidation, often referred to the standard consolidation theory (SCT) [235, 215] or the standard model of systems consolidation[1] , see figure 4.1 (a). According to this theory, a new experience and its several features are first encoded in different associative cortical modules. This information is then quickly transmitted and integrated by the hippocampus, which forms a compressed memory trace. This hippocampal pattern will be repeatedly reactivated offline, which will activate the corresponding neocortical representations. Indeed the reactivation of memory patterns can occur during "offline" states, typically during sleep, or during "online" states, when an experience, or retrieval cue, is related to this existing memory. These replays result in a gradual strengthening of neocortical connections, which leads to a pattern incorporated with pre-existing neocortical representations and solid enough to be independent of the hippocampus. These representations are supposed then to decay rapidly in the hippocampus while then can remain for years in the neocortex. On the one hand, the hippocampus learns quickly online, and is essential for the offline slow learning of the neocortex. According to connectionist modelling, this progressive neocortical learning would allow to prevent catastrophic interference and replacement of existing neocortical patterns with new ones [160, 198]. On the other hand, the encoded memories are rapidly erased in the hippocampus, while they are long-term in the neocortex. The

[1] We focus on the widespread standard consolidation theory here, although interesting alternative views exist, such as the multiple trace theory or the trace transformation theory, which will be addressed in the discussion.

clearance of hippocampal memories would be important because of its limited storage capacity [238].

At this point, the reader may wonder which neurobiological mechanisms are at stake to explain the differences in learning speed and memory stability between the hippocampus and the neocortex. To our knowledge, these aspects have not yet been addressed in the previous models of SCT.

Indeed previous models proposed larger learning rates for hippocampal or cortico-hippocampal connections than for neocortical ones [215, 160, 122, 162, 8, 104, 113]. However, it seems unlikely that variations in LTP speeds induce learning differences of the order of several days or weeks [148]. Instead, this discrepancy could be explained by structural plasticity (i.e. plasticity of the synaptic wiring) [48]. Indeed the hippocampus counts many pre-existing connections. So stimulations can rapidly strengthen these synapses. This fast encoding is unlikely to happen in the much larger neocortical networks. The high number of cells involves the fact that a pre-existing connection between two neocortical neurons has a low probability to exist. But a new stabilized connection can be formed through hippocampal replays. There is a turnover of synapses, new ones are created and weak ones disappear. If two neocortical neurons become connected through this "random" process, then the repetitive hippocampal reactivations would strengthen this new connection. This incremental process would result in memories slowly consolidated in associative cortical modules [85, 148].

In parallel with their reinforcement, little is understood about the clearance of memories [60]. While regular hippocampal memories erasure seems to be a required aspect of SCT models[160, 83], implemented as larger forgetting rates for hippocampal or cortico-hippocampal connections than for neocortical ones [215, 160, 122, 162, 8, 104, 113], its neurobiological origin has been little investigated. An interesting hypothesis is that the dentate gyrus (DG) in the hippocampus, a brain area where neurogenesis occurs throughout life, would be involved in the gradual erasure of hippocampal memories [84, 131]. This effect can be explained by the perturbation of hippocampal network stability as newborn neurons integrate progressively (over several weeks) since these newborn cells are highly excitable. To restore network homeostasis, offsetting mechanisms are engaged. Under these processes, excitability of pre-existing neurons is lowered or their synapses weakened (synaptic scaling), which hinders progressively the reactivation of hippocampal engrams. It is important to note that the erasure is not likely to happen directly through the replacement of the neurons in the engram, since it seems that they would persist for longer times [145]. This model has been implemented in hippocampal networks, where the addition of new neurons to the DG layer induced memory degradation [63, 163, 236]. It seems that the fate of a memory is determined by the balance between the consolidation and decay processes: if a memory is never reactivated, it gradually disappears. Contrary to those in the hippocampus, neocortical memories, once consolidated, could perdure through online replays via retrieval cues. Indeed it is important to note that a retrieval cue will stimulate only a part of the neocortical pattern. That is why the neocortex is dependent on the hippocampus to retrieve its whole pattern at the beginning, while when all connections are established this neocortical engram can be retrieved independently (see figure 4.2).

To summarize, the standard consolidation theory describes the interactions between a fast-learner, fast-forgiver hippocampus whose repetitive memory replays allow a progressive consolidation of patterns in a slow-learner, long-term neocortex. This theory has been developed in some connectionist models [215, 160, 122, 162, 8, 104], which addressed various founding questions surrounding memory organization. However to our knowledge, in these models, little attention has been paid to the neurobiological mechanisms underlying the differences in encoding speeds and durability between the two brain areas. As presented above, the slow learning of the neocortex could be due to its large size. This would imply a long necessary time to bind distant areas, as opposed to a more "compact" hippocampus. But once established, the neocortical connections can be maintained through retrieval cues. These reactivations providing long-term existence would be prevented for hippocampal memories, due to a local decrease of excitation in reaction to the integration of highly excitable newborn DG neurons. To assess whether these proposed mechanisms could lead to SCT, we developed a computational model to follow the temporal dynamics of memory reorganization.

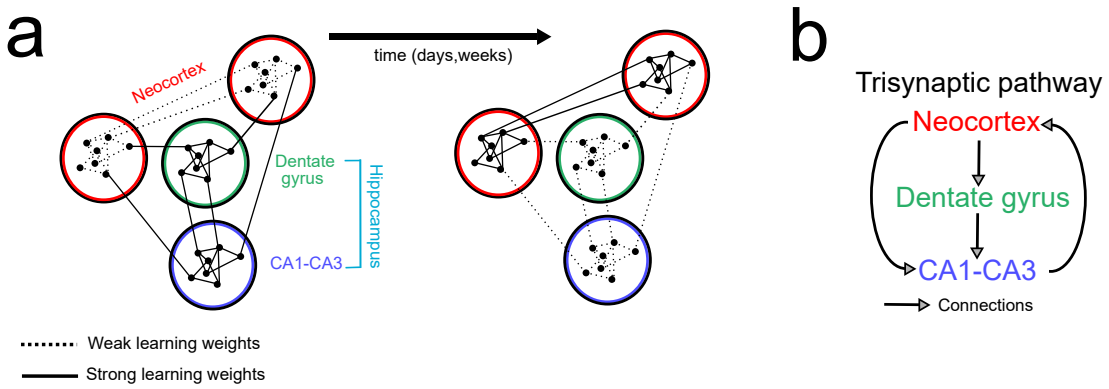

Figure 4.1: Interactions between the different brain areas involved in the standard consolidation theory. **(a)** Standard consolidation theory. An engram is initially present in neocortical areas (red), in a weak form, and in the hippocampus (dentate gyrus in green and CA regions in blue), in a stable form. After some days the distribution of the memory is reorganized. Connections are consolidated in the neocortex, while neocortico-hippocampal and hippocampal connections are degraded. **(b)** Simplified trisynaptic pathway, which is the circuit considered in our model. The different connections between three brain areas, the neocortex, the dentate gyrus, and CA regions are represented here.

4.2.1.2 Neural fields

Contrary to previous SCT connectionist models, we chose to represent the involved process with neural fields. This modelling approach consists of a continuum representation of large-scale biological neural networks. The models are characteristically composed of nonlinear integro-differential equations, with related kernels standing for spatial distributions of neural connections [33, 52]. We believe that this framework is particularly suitable to model SCT for two reasons. First, the whole process involves a complex combination of mechanisms occurring at various time scales, which makes it challenging to model. Reduced models such as neural fields enable us to still have a comprehension of this complexity, allowing for estimations and to some extent mathematical analysis. Second, our approach consists in articulating SCT, which involves interactions at a tissue level, with neurobiological mechanisms. And neural fields, while modelling large areas, keep a close relationship with biophysical realism and have been useful in comprehending some neurobiological processes such as epilepsy, encoding of visual stimuli, the representation of head direction or working memory, which is of particular interest for our addressed issues [33]. This last process corresponds to the temporary storage, on the time scale of seconds, of information in the brain. According to experiments, during a recall task, sensory inputs can be followed by a persistent activity for spatially defined clusters of neurons in the neocortex [95]. This stationary pulse known as a bump of activity corresponds to a class of solutions in neural field theory and has also been studied for multiple bumps patterns [138, 75]. We propose for our model that these bumps represent the different parts of an encoding and retrieved memory pattern. Differently from working memory thus, we consider here short and long-term memories, which imply synaptic modifications (see more explanations below).

In the subsubsection 1.4.2.2 of the introductory chapter 1, we presented a neural field equation (1.63) with synaptic depression. In its simplest form (with $q(x,t) = 1$ for all x, t), the neural field equation which in particular supports stationary bumps [9] is given by:

$$\frac{\partial u}{\partial t}(x,t) = -u(x,t) + \int_{-\infty}^{\infty} dy w(x-y) f(u(y,t) - \kappa) + I_{\text{ext}}(x,t) \tag{4.1}$$

This equation describes the evolution of the activity $u(x,t)$. The membrane time constant of around 10 ms, is often not explicitly written. $I_{\text{ext}}(x,t)$ represents an external input, $w(X)$ is the synaptic weight distribution with distance X, and f is the firing rate function, typically a sigmoid function.

$$f(u-\kappa) = \frac{1}{1+e^{-\beta_f(u-\kappa)}} \tag{4.2}$$

where β_f is the gain and κ is the threshold.

For a synaptic weight kernel chosen as

$$w(X) = \left(1 - \frac{|X|}{\sigma}\right) e^{-\frac{|X|}{\sigma}} \tag{4.3}$$

A stationary bump solution $u_0(x)$, obtained by simplifying the firing rate function as a heaviside function (i.e. $f(u-\kappa) = \Theta(u-\kappa)$ when $\beta_f \to \infty$), is given by

$$u_0(x) = \int_{-a}^{a} dy w(x-y) = W(x+a) - W(x-a) \tag{4.4}$$

With

$$W(X) = Xe^{-\frac{|X|}{\sigma}} \tag{4.5}$$

The bump width $2a$ is determined considering the boundary conditions:

$$u_0(\pm a) = \kappa \tag{4.6}$$

This founding equation constitutes the basis of our model. We extended it in several ways.

First, the synaptic current can be modulated by two negative feedbacks, the spike frequency adaptation and the synaptic depression, which are detailed in the papers of Kilpatrick and Bressloff [127, 126] (see the subsubsection 1.4.2.2 of the introductory chapter 1). The importance of these two processes for our model will be explained in the methods subsection 4.2.2. Spike frequency adaptation, see equation (4.11), describes the attenuation of firing rate after a prolonged period of firing, often due to a calcium-activated potassium current. This process can be implemented as an increase in the threshold $\kappa(x,t)$ [53]. The characteristic time scale of the process has been experimentally found to lie between 40 and 120 ms [153].
Synaptic depression, see equation (4.13), is the phenomenon of presynaptic resource depletion. This process can as well be introduced in the system of equations with the variable $q(x,t)$ in the nonlocal term. This synaptic scaling factor $q(x,t)$ represents the proportion of these resources. The characteristic time scale for depletion is estimated to be between 10 and 330 ms, and the one for ressources recovery has been experimentally shown to lie between 200 and 800 ms [5].
We also add a feedback mechanism for the threshold. As evoked above, insertion of highly excitable newborn neurons can lead to a decrease of the intrinsic excitability of mature neurons by modifying the intensity of currents. This mechanism can be implemented in terms of an increase in the threshold value.

Second, we introduce synaptic dynamics by introducing Hebbian plasticity and a decay expression for the kernel $w(x,y)$, see details in the subsection 4.2.2 with equations (4.17) (4.18) (4.20). Learning plasticity rules in neural field models can take the form of an immediate modulation of the kernel depending on the neurons activities [4]. However in the case of long-lasting synaptic modifications it is interesting to introduce a differential equation with a characteristic larger timescale. A rate-based plasticity rule preserving temporal correlations has been introduced for connections between pre- and post-synaptic neural fields [195], used in particular for topographic maps [89, 65]. However such temporal correlations are not important for our model, and we preferred a simpler Hebbian expression for learning to preserve mathematical and computational tractability. Furthermore, a core feature explaining the differences of learning speeds between the neocortex and the hippocampus is the distance separating distinct areas of an engram. Thus importantly we include in our Hebbian plasticity rule a modulation by the distance between neurons. To model the different distances between the pattern areas, which are assumed to be more remote in the neocortex, we introduce a shift term in the connectivity kernel (see equation (4.16) in the subsection 4.2.2). This learning rule introduced in a neural field however broke the continuity of activity [82], that is why we introduced a continuity function to maintain the continuity of neural fields, see the subsection 4.2.2 for details. In addition to this learning rule, our plasticity equation includes a slow decay term, to represent the degradation of memories in the absence of reactivation.
Another particularity of our model is the connection of three different neural fields, corresponding to the neocortex (C) and the hippocampus separated into the dentate gyrus (D) and the CA regions (H), merged for the sake of simplicity. These brain areas are connected following a particular structure, the trisynaptic pathway [19], see figure 4.1 (b).

Finally, the model is submitted to a long temporal sequence composed of a repetition of phases, see figure 4.2. The initial encoding is simulated by an external two-bumps input on the neocortex, which then propagates to the dentate gyrus and CA regions fields. It is important to note that the information of this bumps signal resides in the location and widths of these bumps. Afterwards, cycles composed of hippocampal replays (HR)– assumed to occur offline, during sleep– and retrieval cues (RC) – assumed to occur online, during a waking period– take place repeatedly. One cycle corresponds approximately to one day. Hippocampal replays are stimulated by an external homogeneous input on CA regions, assumed to represent slow-wave sleep [130]. This stimulation will activate briefly all the neurons of the field, but only neurons involved in the pattern with increased synaptic weights will reactivate bumps for a long time. A retrieval cue corresponds to a single-bump input on the neocortex. It represents an experience partially similar to the encoded pattern (2 bumps), which is likely to reactivate the memory. The neocortical engram can be reactivated either via the hippocampal fields at the beginning of the sequence, or independently when its synaptic weights are consolidated, see figure 4.2.

4.2.2 Description of the model

The system consists in three connected 1D neural fields, each one representing a brain area. The different variables are indexed with α to refer to the area they describe, the neocortex ($\alpha = C$), dentate gyrus ($\alpha = D$) and CA regions ($\alpha = H$), see figure 4.2. x is the position in a neural field and t is time. Let us present the differential equations defining the model's dynamics:

Activity The evolution of activity $u^\alpha(x,t)$ in region α, at position x and time t, is described by

$$\frac{\partial u^\alpha}{\partial t}(x,t) = -u^\alpha(x,t) + I^\alpha(x,t) + I^\alpha_{\text{ext}}(x,t) \tag{4.7}$$

Where $I^\alpha_{\text{ext}}(x,t)$ corresponds to an input current and $I^\alpha(x,t)$ is the synaptic current.

External currents $I^\alpha_{\text{ext}}(x,t)$ is applied at the beginning of each step: the encoding, hippocampal replay (HR) or retrieval cue (RC) step, see the introduction subsection 4.2.1 and figure 4.2 for the biological importance of these steps. Each external stimulation is maintained for a short period of time (see table 4.2).
For the initial encoding input, the external current in the neocortex (C) is a rectangular function, located around positions A^C and B^C, with widths equals to $2a$. These characteristics define the information contained in the memory pattern. We introduce the set $Z^\alpha = \{A^\alpha, B^\alpha\}$.

$$I^C_{\text{ext}}(x,t) = G^{C\text{Ext}} \sum_{z \in Z^C} \Big[\Theta(x-(z-a)) - \Theta(x-(z+a))\Big] i^C(t) \tag{4.8}$$

$i^C(t)$ is a switch function equals to 1 when the stimulus is applied, 0 otherwise. For retrieval cues the signal indicator is partial, only one area A^C or B^C (alternating) is stimulated.
During hippocampal replay steps the external current in CA regions (H) is uniform over space, equals to $G^{H\text{Ext}}$. All H neurons are stimulated for a brief time, however neurons implicated in the engram will fire for a longer duration due to stronger synaptic weights.

Synaptic current $I^\alpha(x,t)$ represents the averaged neural population activity, over the domain of integration Γ^α.

$$I^\alpha(x,t) = \sum_{\beta \in E} G^{\alpha\beta} \int_{\Gamma^\beta} dy q^\beta(y,t) w^{\alpha\beta}_{\text{tot}}(x,y,t) f(u^\beta(y,t) - \kappa^\beta_{\text{tot}}(y,t)) \tag{4.9}$$

Where $E = \{C, D, H\}$ is the set of field indexes. The constants $G^{\alpha\beta}$ represent the trisynaptic circuit, see figure 4.1 (b). $G^{\alpha\beta} > 0$ means that the β field sends connections the α field. Moreover, to equilibrate the total currents received by each field, we fix $G^{\alpha\beta} = 1$ for fields α which receive only one field β, while for other connections $G^{\alpha\beta} = 0.5$, see table 4.2.
$\kappa^\alpha_{\text{tot}}(x,t)$ is the threshold, $q^\alpha(x,t)$ is the synaptic scaling factor and $w^{\alpha\beta}_{\text{tot}}(x,y,t)$ describes the synaptic weights.

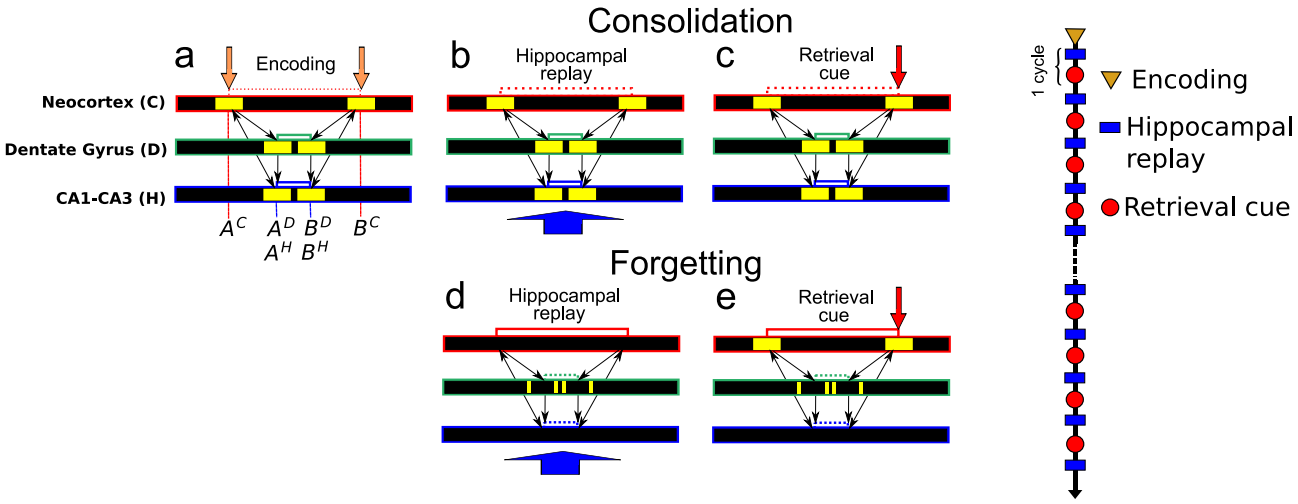

Figure 4.2: Temporal sequence describing standard consolidation theory key moments. **(Left)** Different steps of the computational model. **(a)** The first diagram represents the encoding phase, where two external signals arrive on the neocortical field at two distinct positions, A^C and B^C. The activated neocortical neurons that constitute now the pattern fire, which activates other neurons in the two other hippocampal fields (D, H), at positions A^D and B^D (and A^H and B^H). A^D and B^D are closer to each other than A^C and B^C, so that synaptic weights between them grow faster. After the encoding, cycles of hippocampal replay and retrieval cue steps come one after another, which allows consolidation. **(b)** The hippocampal replay step occurs during sleep. We modeled it by a spatially constant external stimulation on CA regions (H). **(c)** The retrieval cue is a partial signal on only A^C or B^C in the neocortex. **(d,e)** Newborn neurons are regularly generated in the dentate gyrus. In our model we emulate the effect of this process on the stability of hippocampal engrams. We introduce newborn neurons in the dentate gyrus (D). Following experimental suggestions [84], we modeled newborn neurons in D for neurons in the neighbourhood of the pattern by reducing their threshold. Indeed new neurons are more excitable, so they fire a lot. Because of that, the neurons of the pattern in the hippocampus receive a high current, so that their thresholds evolve and increase, in a homeostatic process of synaptic scaling. Thus when external stimuli arrive, the insertion of newborn neurons tends to silence the firing of the pre-existing neurons of the engram. And when a memory pattern is not reactivated, it slowly disappears. **(Right)** Summary of the steps for the whole process. After the encoding phase, cycles of hippocampal replay and retrieval cue steps come one after another. The time between two steps there is a long waiting period, 100 times longer than the duration of a pattern reactivation.

Adaptive thresholds The threshold $\kappa^{\alpha}_{\text{tot}}(x,t)$ is composed of two parts,

$$\kappa^{\alpha}_{\text{tot}}(x,t) = \kappa^{\alpha}(x,t) + \kappa^{\alpha}_{n}(x,t) \tag{4.10}$$

The evolution of $\kappa^{\alpha}(x,t)$ follows spike frequency adaptation [127, 126, 53].

$$\tau_{\kappa}\frac{\partial \kappa^{\alpha}}{\partial t}(x,t) = -(\kappa^{\alpha}(x,t) - \kappa_{\text{in}}) + \eta_{\kappa} f_a(u^{\alpha}(x,t) - \kappa_{\text{in}}) \tag{4.11}$$

In the original studies of this equation, the baseline threshold in the first term of the equation and the threshold in the firing function were different parameters [53, 127, 126]. However, detailed biophysical models indicate that it would be more biologically realistic to use the same parameter in the two terms [23]. That is why we employed here a single parameter κ_{in}.

In our model the presence of several connected neural fields which are quickly activated one after the other, see figure 4.2, modifies the total currents in the activity equation (4.7). This variation takes place quickly at the beginning of a phase, shortly after the stimulation. Spike frequency adaptation occurring at this timescale results in our model in an increase of the threshold from its initial value κ_{in} to a value $\kappa_{\text{in}} + \eta_{\kappa}$. This adaptation maintains the bump width, which characterizes the information of the memory pattern (see the subsection 4.2.4 for the relation between these threshold values and their width). Numerically, see subsection 4.2.3, for the adaptation to properly and quickly enough adjust to preserve the bump width, it was found necessary to use f_a, a firing function smoother than f with $\beta_{f_a} < \beta_f$.

The second term of the threshold $\kappa^{\alpha}_{\text{tot}}(x,t)$ is $\kappa^{\alpha}_{n}(x,t)$, which represents the progressive adaptation mechanism responsible for the local decrease of excitation in reaction to the integration of highly excitable newborn DG neurons. This process prevents the retrieval of hippocampal memories (D and H), see the introduction subsection for biological details 4.2.1. We propose an evolution equation similar to the one for spike frequency adaptation, however with a much slower timescale ($\tau_{\kappa_n} >> \tau_{\kappa}$) and a lower adaptation threshold ($\theta_n < \kappa_{\text{in}}$).

$$\tau_{\kappa_n}\frac{\partial \kappa^{\alpha}_{n}}{\partial t}(x,t) = -\kappa^{\alpha}_{n}(x,t) + \eta_{\kappa_n}\Theta(u^{\alpha}(x,t) - \theta_n) \tag{4.12}$$

A heaviside function Θ was used here for simplicity (the effects of a smoother firing rate function would need to be studied in the future).
To model the high excitability of newborn D neurons, the threshold of the neurons located around the areas involved in the engram is lowered at a value $g_n\kappa_{\text{in}}$ with $g_n < 1$. We only consider neighbour neurons because more distant neurons would have a very small effect, see figure 4.2 (d)(e). The domain of these newborn neurons can be written as

$$\bigcup_{z\in Z^D}\Big([z-a-\delta_n, z-a] \cup [z+a, z+a+\delta_n]\Big)$$

with δ_n the width of newborn neurons subarea. Since these neurons fire continuously for a long time even in the absence of input, the slow adaptation term $\kappa^{\alpha}_{n}(x,t)$ in the two hippocampal fields (D and H) reaches its stationary value η_{κ_n}. This will prevent the activation of bumps by external currents at the following steps since the thresholds would already be too high.

In addition to biological realism, it was necessary to distinguish the dentate gyrus and the CA regions in our model. Indeed, if instead only one hippocampal field was implemented, the highly excitable newborn neurons would have affected also the neocortical field, which would have prevented retrieval. Here, since the dentate gyrus does not send direct connections to the neocortex, only the dentate gyrus itself and the CA regions field are impacted by the local threshold rise due to neurogenesis.

Synaptic scaling The evolution of the synaptic scaling factor $q^{\alpha}(x,t)$ follows synaptic depression, as proposed by Kilpatrick and Bressloff (2010) [127, 126].

$$\frac{\partial q^{\alpha}}{\partial t}(x,t) = \frac{1-q^{\alpha}(x,t)}{\alpha_q} - m^{\alpha}_{q}(x,t)q^{\alpha}(x,t)f_a(u^{\alpha}(x,t) - \kappa^{\alpha}_{\text{tot}}(x,t)) \tag{4.13}$$

In our model this term is responsible for the disappearance of the bump after a certain time. In contrast to the original equation however, we introduce an activity dependent term for synaptic depletion

$$m^{\alpha}_{q}(x,t) = \beta_q u^{\alpha}(x,t) \tag{4.14}$$

The effect of this term is to maintain bump durations roughly constant when learning weights evolve and/or neurogenesis is applied.

Synaptic weights The kernel $w_{\text{tot}}^{\alpha\beta}(x,y,t)$ is defined as:

$$w_{\text{tot}}^{\alpha\beta}(x,y,t) = w(x - \Delta^{\alpha\beta}(x) - y) + \gamma^{\alpha\beta}\eta_s^{\alpha\beta}(x,t)s^{\alpha\beta}(x,y,t) \tag{4.15}$$

- $w(X)$ are the permanent weights between a post-synaptic neuron at position x and a presynaptic neuron at position y. They characterize the connectivity.

$$w(X) = \left(1 - \frac{|X|}{\sigma}\right) e^{-\frac{|X|}{s}} \tag{4.16}$$

The position-dependent shift $\Delta^{\alpha\beta}(x) = (B^\alpha - B^\beta)\,\text{sgn}(x)$ emulates the difference in size of the neorcortical and hippocampal fields. Despite the intrinsic difference of distances between pattern locations ($|A^C - B^C| > |A^D - B^D|$ and $|A^D - B^D| = |A^H - B^H|$), $\Delta^{\alpha\beta}(x)$ allows to force the permanent connection between A^C and A^H (or A^D), B^C and B^H (or B^D). For instance, for $x = A^C$,
$w(A^C - \Delta^{CH}(A^C) - A^H) = w(A^C - \Delta^{CC}(A^C) - A^C) = w(0) = 1$, i.e. the weight between A^C and A^C is the same as between A^C and A^H.

- The second term $\gamma^{\alpha\beta}\eta_s^{\alpha\beta}(x,t)s^{\alpha\beta}(x,y,t)$ represents synaptic plasticity. In this expression, $\gamma^{\alpha\beta}$ are positive constants, that are assumed to be larger for intra than for inter-field connections, $\gamma^{\alpha\alpha} > \gamma^{\alpha\beta}$ for $\alpha \neq \beta$, to represent stronger interactions within one brain area.
$s^{\alpha\beta}(x,y,t)$ is a variable that represents the learning weights.

$$\frac{\partial s^{\alpha\beta}}{\partial t}(x,y,t) = L^{\alpha\beta}(x,y,t) - F^{\alpha\beta}(x,y,t) \tag{4.17}$$

The first term $L^{\alpha\beta}(x,y,t)$ is a bounded, distance-dependent, Hebbian [91] learning rule.

$$L^{\alpha\beta}(x,y,t) = (1 - s^{\alpha\beta}(x,y,t))d(x,y) \times f(u^\alpha(x,t) - \kappa_{\text{tot}}^\alpha(x,t))f(u^\beta(y,t) - \kappa_{\text{tot}}^\beta(y,t)) \tag{4.18}$$

Where the distance modulates the learning rate.

$$d(x,y) = \frac{A_d}{\sigma_d} e^{-|x-y|/\sigma_d} \tag{4.19}$$

The closer x and y positions are, the larger $d(x,y)$ is and the quicker the learning process occurs. Especially since $|A^C - B^C| > |A^D - B^D|$ ($|A^H - B^H| = |A^D - B^D|$), we get $d(A^D - B^D) > d(A^C - B^C)$, i.e. the process is faster in the hippocampus (D, H) than in the neocortex (C).
The second term $F^{\alpha\beta}$ is a forgetting, decay term, which occurs much more slowly than the first term ($c_0 << 1$).

$$F^{\alpha\beta}(x,y,t) = \begin{cases} \frac{c_0}{s^{\alpha\beta}(x,y,t)} & \text{if } s^{\alpha\beta}(x,y,t) > 0 \\ 0 & \text{if } s^{\alpha\beta}(x,y,t) = 0 \end{cases} \tag{4.20}$$

The $s^{\alpha\beta}(x,y,t)$ variable decays until their minimal value, 0.
Between two steps or when patterns cannot be retrieved, neurons do not fire for a long time. So that $L^{\alpha\beta}(x,y,t)$ vanishes and the forgetting term $F^{\alpha\beta}(x,y,t)$ becomes progressively larger, until $s^{\alpha\beta}(x,y,t) = 0$.

This additional $s^{\alpha\beta}(x,y,t)$ factor would introduce a discontinuity in the activity [82]. We therefore add a continuity function $\eta_s^{\alpha\beta}(x,t)$ in equation (4.15) to maintain the continuity in $u^{\alpha\beta}(x,t)$ expression.

$$\eta_s^{\alpha\beta}(x,t) = \left[\int_{\Gamma^\beta} dy w(x - \Delta^{\alpha\beta}(x) - y)\Theta(s^{\alpha\beta}(x,y,t)) - \kappa_{\text{in}}\right]_+ \tag{4.21}$$

Symbol	Definition
Time varying functions	
u^α	Activity
f	Firing function
f_a	Firing function for κ^α and q^α equations
I^α	Synaptic current
I^α_{ext}	External current
$s^{\alpha\beta}$	Learning weight
$\eta^{\alpha\beta}_s$	Continuity function
$\kappa^\alpha_{\text{tot}}$	Threshold
κ^α	Threshold - adaptation
κ^α_n	Threshold - neurogenesis
q^α	Synaptic scaling factor
Time independent functions	
w	Permanent weight
W	Integral of the permanent weight
d	Distance function

Table 4.1: Main functions used for the neural field model

where

$$[\cdot]_+ = \begin{cases} \cdot & \text{if } \cdot > 0 \\ 0 & \text{if } \cdot \leq 0 \end{cases} \tag{4.22}$$

When $s^{\alpha\beta}(x, y, t) > 0$, i.e. for neurons of the pattern, the integral in equation (4.21) corresponds to the received bump current of one field, which is κ_{in} at boundaries. This guarantees continuity at boundaries, see the subsection 4.2.4 for more details.

4.2.3 The three connected neural fields with spike frequency adaptation, synaptic depression and synaptic weight dynamics reproduce the main features of the standard consolidation theory

The whole process begins with the encoding step which is followed by repeated cycles of hippocampal replay (HR) and retrieval cue (RC) step, see figure 4.2 (Right). Between active phases are 100 times longer inactive periods. First, we study below the consolidation mechanism, then the forgetting effect of neurogenesis is tested on consolidated memory patterns. Figure 4.2 is used as a visual support throughout this results subsection as a guide to the different phases of the process.
For conveniance, throughout this paper we name neurons within the excited region around A^α ($[A^\alpha - a, A^\alpha + a]$) or B^α ($[B^\alpha - a, B^\alpha + a]$), as respectively A^α or B^α neurons.
Furthermore, learning weights $s^{\alpha\beta}(x, y, t)$ are shown instead of $w^{\alpha\beta}_{\text{tot}}(x, y, t)$, because they constitute a relevant and concise measure of synaptic plasticity, since they are bounded between 0 and 1.

4.2.3.1 Consolidation

Encoding The process is initiated by the encoding step, where an external signal stimulates two distinct areas around the positions A^C and B^C, in the neocortex (C), see the schematized process in figure 4.2 (a) and the corresponding numerical simulation in figure 4.3 (a). Activated cortical (C) neurons then induce firing in the dentate gyrus (D), and when CA regions (H) neurons receive inputs from C and D, they are activated. Neurons fire at these two locations during a certain time before slow adaptation shuts them down. During this firing period learning weights values increase, seeequation (4.18). During encoding, all the weights increase between neurons located in an engram location ($[A^\alpha - a, A^\alpha + a]$ and $[B^\alpha - a, B^\alpha + a]$) because of Hebbian synaptic plasticity (see equation (4.18)). However as illustrated in supplementary figure S 1 (b) (c), the weights between neurons in A^α and B^α increase much slower. The $A^C - B^C$ weights increase more slowly than the $A^D - B^C$ ones, which in turn increase more slowly than the $A^D - B^D$ weights. This is due to the distance-modulated learning rate of equation (4.19). Therefore, in our model consolidation is slower

Parameter	Value	Definition
Structure and positions		
E	-	Set of field indexes
C	-	Neocortex field index
D	-	Dentate gyrus field index
H	-	CA regions field index
A^C	-16	Position of the C left pattern location
B^C	16	Position of the C right pattern location
A^D	-10	Position of the D left pattern location
B^D	10	Position of the D right pattern location
A^H	-10	Position of the H left pattern location
B^H	10	Position of the H right pattern location
a	0.9	Bump widths in all fields
G^{CC}	1	Amplitude of the current from C to C
G^{DD}	1	Amplitude of the current from D to D
G^{HH}	1	Amplitude of the current from H to H
G^{CH}	1	Amplitude of the current from H to C
G^{CD}	0	Amplitude of the current from D to C
G^{HD}	0.5	Amplitude of the current from D to H
G^{HC}	0.5	Amplitude of the current from C to H
G^{DC}	1	Amplitude of the current from C to D
G^{DH}	0	Amplitude of the current from H to D
σ	1.5	Width of the permanent weights
Firing rate		
β_f	250	Gain of the firing function
β_{f_a}	50	Gain of the firing function for κ^α and q^α equations
Learning kernels		
γ	1.5	Constant for intra-field learning weights ($\gamma^{\alpha\alpha} = \gamma$)
cr	0.2	Factor for the constant for inter-field learning weights ($\gamma^{\alpha\beta} = cr \times \gamma$, $\alpha \neq \beta$)
A_d	3	Amplitude of the distance function
σ_d	9	Width of the distance function
c_0	8.10^{-7}	Decay rate
Thresholds		
κ_{in}	0.54	Baseline threshold
τ_κ	0.8	Time scale for spike frequency adaptation
η_κ	0.54	Strength for spike frequency adaptation
τ_{κ_n}	1000	Time scale of the slow adaptation related to neurogenesis
η_{κ_n}	0.5	Strength of the slow adaptation related to neurogenesis
θ_n	0.001	Baseline threshold for slow adaptation related to neurogenesis
Synaptic scaling		
α_q	800	Time scale of synaptic resources recovery
β_q	0.01	Inverse of the time scale of synaptic resources depletion
External currents		
$G^{C\text{Ext}}$	1.5	Amplitude of the external current in C
$G^{H\text{Ext}}$	0.87	External current value in H
–	1.8	Duration of the external stimulation in C
–	1.2	Duration of the external stimulation in H
Neurogenesis		
δ_n	0.32	Width of the newborn neurons area
g_n	0.1	Factor of newborn neurons reduced threshold
Numerical parameters		
x_{m1}	-30	Left extremity of a field
x_{m2}	30	Right extremity of a field
dx	0.08	Spatial increment
dt	0.1	Time increment

Table 4.2: Parameters values used for the neural field model. Because of the abstract nature of the model, units were not taken into account here. See the subsection 4.2.5 for a discussion on the timescale parameters.

in the neocortex (C) because the locations of the memory pattern are further away than in the hippocampus, see the methods subsection 4.2.2.

Hippocampal replay A way to consolidate is through the repeated reactivations during sleep, which originated in the hippocampus, see the schematized hippocampal replays in figure 4.2 (b) and the numerical simulation in figure 4.3 (b) and in supplementary figure S 2. During hippocampal replay, an external signal stimulates all neurons of the CA regions (H) field. However, only the neurons involved in the pattern locations fire for a long time. Indeed, the current they receive has a higher value, since their learning weights are stronger. This firing in H leads to pattern reactivations in C and D, see figure 4.3 (b). The two parts of the memory pattern being active, the cross-learning weights can grow and thus consolidate the engram, see supplementary figure S 2 (b)(c).

Retrieval cue Since the learning weights between A^α and B^α grow faster in the hippocampus, memory in the early steps of the process can be retrieved only with the hippocampal neurons, as illustrated in the numerical simulation of figure 4.3 (c). During this step, only the B^C location is stimulated. Retrieval is achieved when this stimulation of B^C leads to the activation of A^C. However at the initial stages of the process, the activation of A^C is not direct from B^C to A^C, it goes via the hippocampus. Indeed, at the initial stage the weights between A^C and B^C are small. So the signal from B^C is first sent to hippocampal fields. Inside the hippocampus, the $A^D - B^D$ or $A^H - B^H$ weights are strong enough to reactivate A^D or A^H. This two-bump signal is then sent back to the neocortex via the strong $A^H - A^C$ weights, which allows the complete reactivation of A^C, see figure 4.3 (c). With the two locations of the neocortical memory pattern being active ($[A^C - a, A^C + a]$ and $[B^C - a, B^C + a]$), the cross-learning weights can grow in the neocortex and thus consolidate the engram, see figure 4.4 (a) and supplementary figure S 3 (b)(c).
To illustrate further that the neocortex is dependent on the hippocampal fields for its engram retrieval in these initial stages, we did the same simulation but with impaired learning weights connections in the hippocampal fields, between them and the neocortical field (setting the constants $\gamma^{\alpha\beta} = 0$ for all α, β, except for γ^{CC} in equation (4.15)). In this configuration, the complete neocortical pattern cannot be retrieved (figure 4.3 (d)) and no cross-learning weights consolidation can occur (supplementary figure S 4 (b)(c)). Hence, memory cannot be retrieved without a functional hippocampus during the initial stages of the consolidation process.

End of consolidation After approximately 6 cycles (equivalent to six days) of retrieval cue and hippocampal replay steps, the learning weights are fully consolidated everywhere, see figure 4.4 (a). In particular, strong weights connect A^C and B^C in the neocortex, which was the longest process. The simulation of a retrieval cue step with impaired learning weights connections as presented in the above paragraph, highlights a complete neocortical pattern retrieval, see figure 4.3 (e). Contrary to the initial stages of the consolidation process where neocortical pattern retrieval was not possible without the hippocampus learning weights (figure 4.3 (d)), at the end of consolidation retrieval can happen independently of the hippocampal fields (figure 4.3 (d)), since of $A^C - B^C$ weights are strong enough.

4.2.3.2 Forgetting

During this consolidation process, we have seen how the neocortical pattern was progressively consolidated through hippocampal pattern reactivations. We evoked in the introduction the fact that while neocortical memories, once consolidated, can remain for years, it seems that hippocampal patterns disappear, and the neocortical pattern becomes independent of the hippocampus. To understand this other part of the double dynamics (consolidation/erasure), we followed the neurogenesis hypothesis. This theory states that adult neurogenesis in the dentate gyrus (D), disturbs hippocampal circuits and thus leads to an impossibility to retrieve the pattern. And when a pattern is never retrieved, it slowly disappears. To model neurogenesis, we did not replace neurons of the pattern. Indeed, the neurons involved in a pattern seem on the opposite to have a survival advantage [145]. Instead, we focus on neurons that are located in the neighbourhood of the pattern (further away from the pattern, no significant effects is expected). These newborn neurons fire a lot, so the thresholds of neurons around them adapt and stay high. Upon stimulation, the neurons of the hippocampal patterns are not activated because of their large threshold, see figure 4.3 (f)(g).

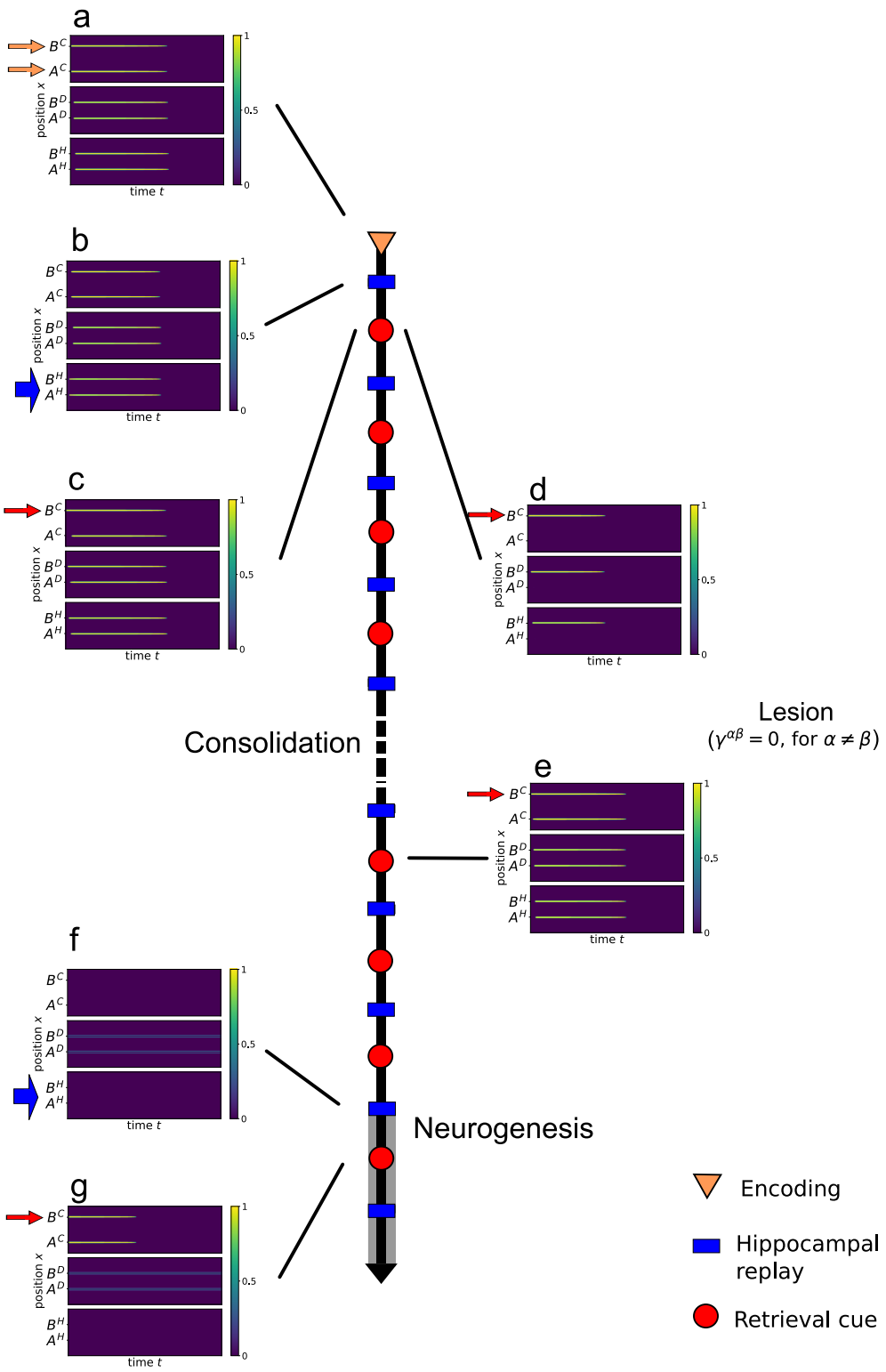

Figure 4.3: Snapshots in the temporal sequence of firing rates in the three fields, neocortex (C), dentate gyrus (D) and CA regions (H). **(a)** The encoding step shows faster learning in hippocampal fields than in neocortical ones. The initial stimuli are two bumps around positions A^C and B^C in the neocortical field. They activate C neurons which in turn activate D neurons. Then since C and D neurons fire, H neurons can be activated. In the end, neurons shutdown, due to the depletion of synaptic resources. **(b)** The hippocampal replay step allows engrams reactivation. We modeled hippocampal reactivation by sending a stimulus uniform over space on H. All H neurons receive this input, but only those involved in the pattern fire for a long time, because of their non zero learning weights. Activated H neurons lead to firing in C neurons, which then activate D neurons.

(c) The retrieval cue step allows engrams reactivation. This step consists in stimulating only the A^C or B^C location of the neocortex (here B^C). Retrieval is exhibited by subsequent activation of A^C. A signal is sent on only B^C in the neocortical field. The weights between A^C and B^C are still small, C is still dependent on H to recover the whole pattern. Thus, B^C neurons first activate B^D, then B^H neurons are activated by B^C and B^H neurons, which will activate A^H neurons thanks to the strong enough $B^H - A^H$ learning weights. Finally, the A^H neurons activate A^C neurons via the strong $A^C - A^H$ weights, leading to the whole pattern recovery.**(d,e)** The retrieval cue stimulation with hippocampal "lesion" is obtained by cancelling the constants $\gamma^{\alpha\beta}$ in the hippocampal fields, between them and the neocortical field ($\gamma^{\alpha\beta} = 0$ for all α, β except γ^{CC}). **(d)** Neocortical engram reactivation depends on hippocampal fields during the retrieval cue steps. Only the B^α neurons, directly stimulated by the partial retrieval cue, fire. Memory cannot be retrieved without a functional hippocampus. **(e)** Neocortical engram reactivation is independent of hippocampal fields during the retrieval cue steps at the end of consolidation. The A^α neurons are also activated, since $A^C - B^C$ weights are strong enough at this stage. Memory is here retrieved without a functional hippocampus. **(f,g)** When neurogenesis is effective, neurons in the neighbourhood of the pattern in the dentate gyrus field are modeled as highly excitable newborn neurons (lower threshold, see the subsection 4.2.2). The thin lines in the D field show the continuous firing of those new neurons. As a result, the thresholds of the neurons in the vicinity adapt and stay high. **(f)** Neurogenesis in the dentate gyrus prevents the reactivation of hippocampal engrams during the hippocampal replay phase. The neurons of the hippocampal pattern stay silent in response to the replay pattern, due to the high thresholds caused by the excitable newborn D neurons. **(g)** Neurogenesis in the dentate gyrus prevents the reactivation of hippocampal engrams during neocortical retrieval cues. C neurons fire since there are no direct connections from D to C. However nothing fires in the hippocampal fields, due to the high thresholds caused by the excitable newborn D neurons. The retrieval cue activates the whole pattern in C independently of the hippocampal fields.

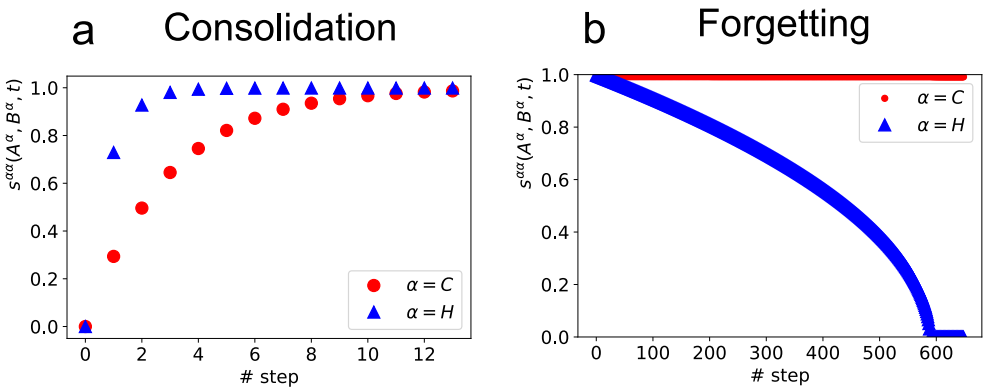

Figure 4.4: The learning weights $s^{CC}(A^C, B^C, t)$, $s^{HH}(A^H, B^H, t)$ evolution in the neural fields model highlights the slow learning, stable memory features of the neocortex and the fast learning, unstable memory features of the hippocampus. Each point is a measure of the learning weights $s^{CC}(A^C, B^C, t)$ (red circles) and $s^{HH}(A^H, B^H, t)$ (blue triangles) at the beginning of a step. $s^{DD}(A^D, B^D, t)$ is not shown here, since it displays the same dynamics as $s^{HH}(A^H, B^H, t)$. (a) The neocortex is a slower learner than the hippocampus. During the consolidation phase, $A^H - B^H$ rise faster than $A^C - B^C$ learning weights. $s^{HH}(A^H, B^H, t)$ reach the maximal value 1 after approximately 4 steps, while for neocortical ones it is achieved in 12 steps. This difference is explained by the distance-dependent plasticity rule (see equation (4.19)), since the distance between A^C, B^C is larger than between A^H, B^H ($|A^C - B^C| > |A^H - B^H|$). (b) The hippocampus forgets the pattern, while it remains stable in the neocortex. When neurogenesis is effective, the hippocampal pattern cannot be retrieved (see figure 4.3 (f) (g)), so that $s^{HH}(A^H, B^H, t)$ slowly decrease (see equations (4.17) (4.20)). On the opposite, the neocortical pattern can be retrieved independently of the hippocampal fields during the retrieval cue steps (see figure 4.3 (g)), so that $s^{CC}(A^C, B^C, t)$ are maintained at the maximum value 1.

Hippocampal patterns are never retrieved, contrary to neocortical patterns during retrieval cues since the C pattern is now strong enough to be retrieved entirely. So after approximately 300 cycles – equivalent to 300 days), which represent approximately 43 weeks – we can observe the complete erasure of hippocampal patterns while the neocortical pattern is still strong, see figure 4.4 (b) and supplementary figure S 5 (c)(d). The final test of the neocortical partial retrieval cue is achieved, see figure S 5 (b). The neocortical pattern is well retrieved, independently of the hippocampal fields.

4.2.4 Effect of learning weights on bump solutions and stability analyses

This subsection focuses on the effect of the learning weights on the existence and the stability of stationary bumps solutions. We assume that the width of the bump is conserved accross the fields, i.e. $a^C = a^D = a^H = a$, which is verified numerically. To carry out an analytical treatment of existence and stability of bumps we consider the case where all learning weights are at their equilibrium value, after the consolidation process, with the decay term $F^{\alpha\beta}(x, y, t)$ neglected, since $c_0 << \min(d(x, y))$. In fact this leads to a dimension reduction of the system, since bumps profiles will all be the same. Which is not the case for transient learning weights due to the differences of timescales in and between fields. Furthermore, the term of the threshold $\kappa_n^\alpha(x, t)$ is not considered here, due to its large time scale. It could be used as a slow-varying parameter in continuation bifurcation analysis. The spike frequency adaptation and the synaptic depression effects are studied separatly.

Throughout this analysis we will use the results of the papers [127, 126], that are restricted to a single field, but we adapt them to our model composed of three connected neural fields, with learning weights.

4.2.4.1 Spike frequency adaptation

Existence of stationary bumps solution As is usual in the field, we first set the firing functions as heaviside functions ($\beta_f \to \infty$, $\beta_{f_a} \to \infty$). In this case a stationary bump solution $\left(u_0^\alpha(x), \kappa_0^\alpha(x), s_0^{\alpha\beta}(x, y)\right)$ satisfies equations (4.23) (4.24) (4.25):

$$u_0^\alpha(x) = \begin{cases} \sum\limits_{\beta \in E} G^{\alpha\beta} J^{\alpha\beta}(x, a) & \text{if } x \notin R[u_0^\alpha] \\ \sum\limits_{\beta \in E} G^{\alpha\beta}[J^{\alpha\beta}(x, a)\xi_s - (\xi_s - 1)\kappa_{\text{in}}] & \text{if } x \in R[u_0^\alpha] \end{cases} \tag{4.23}$$

$$\kappa_0^\alpha(x) = \begin{cases} \kappa_{\text{in}} & \text{if } x \notin R[\kappa_0^\alpha] \\ \kappa_{\text{in}} + \eta_\kappa & \text{if } x \in R[\kappa_0^\alpha] \end{cases} \tag{4.24}$$

$$s_0^{\alpha\beta}(x, y) = \begin{cases} 0 & \text{if } x \notin R[u_0^\alpha] \text{ or } y \notin R[u_0^\beta] \\ 1 & \text{if } x \in R[u_0^\alpha],\ y \in R[u_0^\beta] \end{cases} \tag{4.25}$$

With

$$J^{\alpha\beta}(x, a) = \sum_{z \in Z^\beta} \Big[W(x - \Delta^{\alpha\beta}(x) - (z - a)) - W(x - \Delta^{\alpha\beta}(x) - (z + a)) \Big] \tag{4.26}$$

$R[u_0^\alpha]$ is the excited region for u_0^α, which corresponds also to the location where learning weights have a non-zero value, defined as

$$R[u_0^\alpha] = \bigcup_{z \in Z^\alpha} [z - a, z + a] \tag{4.27}$$

The bump boundaries are defined by the threshold conditions:

$$u_0^\alpha(z \pm a) = \kappa_{\text{in}} + \eta_\kappa = 2 \times 2ae^{-2a/s} \tag{4.28}$$

$R[\kappa_0^\alpha]$, the excited region for κ_0^α is different

$$R[\kappa_0^\alpha] = \bigcup_{z \in Z^\alpha} [z - b, z + b] \tag{4.29}$$

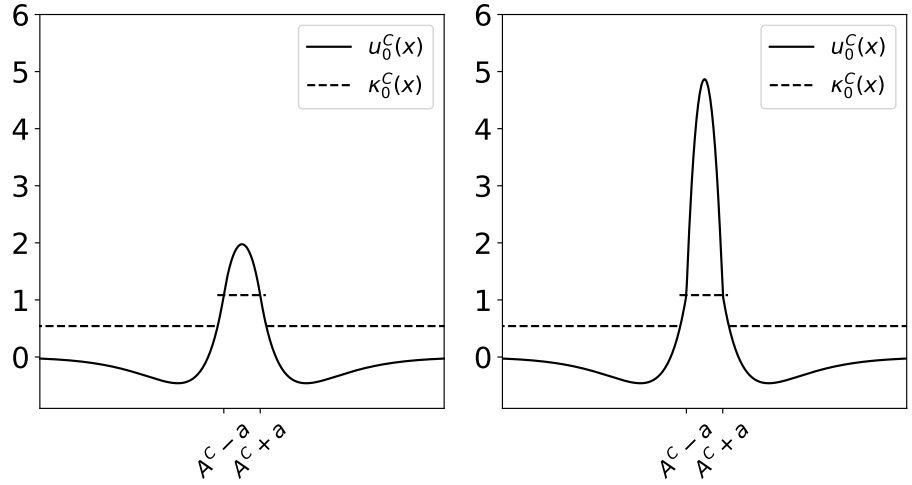

Figure 4.5: Shape of a bump in the C field. (Left) With no learning, all $s_0^{\alpha\beta}(x,y) = 0$ along the whole field (Right) with synaptic modifications at their maximum value, all $s_0^{\alpha\beta}(x,y) = 1$ in the pattern areas.

with b implied in the relation

$$u_0^\alpha(z \pm b) = \kappa_{\text{in}} = 2ae^{-2a/s} \tag{4.30}$$

Please note that $b > a$.

The factor ξ_s is defined as:

$$\xi_s = 1 + \gamma(1 + cr)4a \tag{4.31}$$

The second term of ξ_s represents the sum over the fields and the bumps of the integral of the learning weights. The term ξ_s accounts for the learning weights in the neural fields model. In absence of learning, $\xi_s = 1$, otherwise $\xi_s > 1$. We will study its effect on the existence of bumps and on their stability. We introduce the total weights defined as the sum of the synaptic plasticity term with learning weight at equilibrium and the permanent weights.

$$w_{\text{tot}}^{\alpha\beta}(x,y) = w(x - \Delta^{\alpha\beta}(x) - y) + \gamma^{\alpha\beta}\eta_s^{\alpha\beta}(x)s_0^{\alpha\beta}(x,y) \tag{4.32}$$

where

$$\eta_s^{\alpha\beta}(x) = \left[J^{\alpha\beta}(x,a) - \kappa_{\text{in}}\right]_+ \tag{4.33}$$

Two bump profiles in the C field with all $s_0^{\alpha\beta}(x,y) = 0$ and all $s_0^{\alpha\beta}(x,y) = 1$ are presented in respectively in figures 4.5 (Left) and (Right). We can observe the continuity of the solution even with learning weights. The bump boundaries a are maintained with plasticity, but inside $R[u_0^C]$ the amplitude of the bump is larger.

Stability of the bumps Following the computations of Kilpatrick and Bressloff (2010) [127], we develop equation (4.7) with $u^\alpha(x,t) = u_0^\alpha(x) + \epsilon\phi_u^\alpha(x,t)$, where $\phi_u^\alpha(x,t)$ are smooth perturations and $\epsilon << 1$. Since we truncate the results at first order, learning weights perturbations do not appear, as well as for threshold perturbations. Please note that the linear stability equations we derive here thus will not reflect the underlying translation invariance of the system.
We then assume separability $\phi_u^\alpha(x,t) = e^{\lambda t}\psi_u^\alpha(x)$.
The calculations are detailed in Kilpatrick and Bressloff (2010) [127], the modifications of our analysis compared to [127] is mainly that the value above which the threshold starts increasing and the baseline threshold are both equal to κ_{in}, which simplifies the analysis. More specifically, in our model, the three fields connections and the learning weights add a 2 factor multiplying the permanent weights, and induce a modification of the spatial derivative of $u_0^\alpha(x)$. In fact the factor π_u takes into account different left and right derivatives, see equation (4.35).
The general equation can be written as:

$$(\lambda + 1)\psi_u^\alpha(x) = \sum_{\beta \in E} G^{\alpha\beta} \sum_{z \in Z^\beta} \left[w_{\text{tot}}^{\alpha\beta}(x, z-a)\frac{\psi_u^\beta(z-a)}{|u_0'^\beta(z-a)|} + w_{\text{tot}}^{\alpha\beta}(x, z+a)\frac{\psi_u^\beta(z+a)}{|u_0'^\beta(z+a)|} \right] \tag{4.34}$$

and the factor

$$\frac{1}{|u_0'^{\alpha}(z+\sigma a)|} = \begin{cases} \pi_u \text{ if } \psi_u^{\alpha}(z+\sigma a) > 0 \\ \frac{\pi_u}{\xi_s} \text{ if } \psi_u^{\alpha}(z+\sigma a) < 0 \end{cases} \tag{4.35}$$

with

$$\pi_u = \frac{1}{2(w(0) - w(2a))} \tag{4.36}$$

The essential spectrum is located at $\lambda = -1$. The discrete spectrum is obtained by setting $x = z \pm a$, with $z = A^{\alpha}$ or B^{α}. At these boundaries $\eta_s^{\alpha}(x) = 0$, erasing the learning weights terms. Furthermore the distance between two bumps, even in the nearest case in D, H, is large enough so that the permanent weights values between them are neglectable. Moreover, all learning weights are equal. Therefore, we can assume that $u_0^{\alpha}(x)$, $\kappa_0^{\alpha}(x)$ are equal at their bump boundaries independently of the field. We also consider $\psi_u^{\alpha}(x)$, $\psi_{\kappa}^{\alpha}(x)$ equals for each boundary. This simplification allows the analytical analysis below.
Moreover, within the linear regime, infinitesimal changes in u^{α} will only perturb the threshold in a neighborhood of $x = z \pm b$, so that $\phi_{\kappa}^{\alpha}(z \pm a, t) = 0$.
There are four classes of solutions which determine the discrete spectrum: expansion, contraction, leftward shift and rightward shift of the stationary bump solution.

Expansion case: $\forall \beta \in E, \forall z \in Z^{\beta}, \forall \sigma \in \{-1, 1\}$, $\psi_u^{\beta}(z + \sigma a) > 0$

$$\Big[2\pi_u[w(0) - w(2a)] - (\lambda + 1)\Big]\Big[2\pi_u[w(0) + w(2a)] - (\lambda + 1)\Big] = 0 \tag{4.37}$$

$$\lambda_{\pm} = \frac{w(0) \pm w(2a)}{w(0) - w(2a)} - 1 \leq 0 \tag{4.38}$$

These eigenvalues are independent of ξ_s. With our parameter values, we find that $\lambda_{-} = 0$ and $\lambda_{+} > 0$, uncovering a degenerate case for which we cannot conclude on the stability.

Contraction case: $\forall \beta \in E, \forall z \in Z^{\beta}, \forall \sigma \in \{-1, 1\}$, $\psi_u^{\beta}(z + \sigma a) < 0$

$$\lambda_{\pm} = \frac{1}{\xi_s} \frac{w(0) \pm w(2a)}{w(0) - w(2a)} - 1 \leq 0 \tag{4.39}$$

Figure 4.6 presents the evolution of the contraction eigenvalues with γ ($\xi_s = 1 + \gamma(1 + cr)4a$). With our parameter values the bump is stable to contraction perturbation, with increasing stability when γ increases.

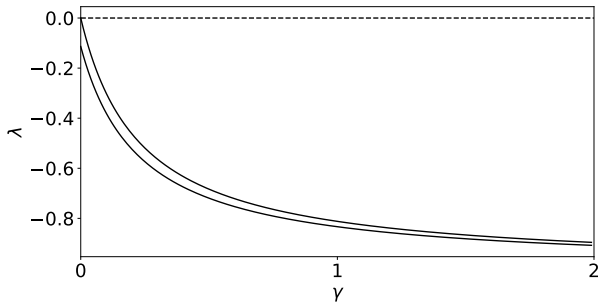

Figure 4.6: Learning weights stabilize the bump in case of a contraction perturbation. Eigenvalues λ decrease as γ increases (which increases ξ_s, as $\xi_s = 1 + \gamma(1 + cr)4a$).

Leftward shift case: This case corresponds to a class of solutions where $\forall \beta \in E, \forall z \in Z^{\beta}$, $\psi_u^{\beta}(z + a) < 0$ and $\psi_u^{\beta}(z - a) > 0$.

$$\Big[2\pi_u w(0) - (\lambda + 1)\Big]\Big[2\pi_u/\xi_s w(0) - (\lambda + 1)\Big] - 1/\xi_s \Big[2\pi_u w(2a)\Big]^2 = 0 \tag{4.40}$$

$$\lambda_{\pm} = 2\pi_u \frac{(1+1/\xi_s)w(0) \pm \sqrt{(1+1/\xi_s)^2 w(0)^2 - 4[w(0)^2 - 1/\xi_s w(2a)^2]}}{2} - 1 \tag{4.41}$$

These eigenvalues are real for small ξ_s values (complex eigenvalues violate the initial assumption that λ are real), where $\lambda_{\pm} \leq 0$ and $\xi_s > 1$. When ξ_s increases, λ_+ decreases and λ_- increases, see figure 4.7. Therefore, we cannot conclude on the effect of learning weights on shift perturbations.

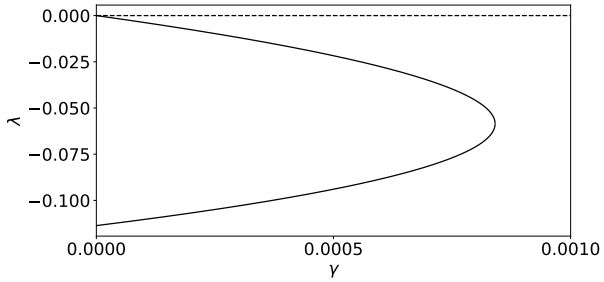

Figure 4.7: It is not possible to conclude on the influence of learning weights in case of a shift perturbation. These eigenvalues are real for small γ values, where $\lambda_{\pm} \leq 0$. λ_+ decreases and λ_- increases as γ increases (which increases ξ_s, as $\xi_s = 1 + \gamma(1 + cr)4a$).

Rightward shift case: This case corresponds to a class of solutions where $\forall \beta \in E, \forall z \in Z^{\beta}$, $\psi_u^{\beta}(z+a) > 0$ and $\psi_u^{\beta}(z-a) < 0$.
The spectrum associated with rightward shifts is identical to that of leftward shifts due to the reflection symmetry of the system.

As a conclusion, learning weights stabilize the system through contraction, but have no effects on stability in case of an expansion perturbation. The eigenvalues are all negative. We cannot conclude on their influence on the shift behaviour since it increases one eigenvalue and diminish the other one.
This method can only provide sufficient conditions for instability but not stability of a bump. So there could be unstable modes not detected by this analysis, although numerical simulations suggest that this is not the case for the parameters of the model.

4.2.4.2 Synaptic depression

We now study the effect of the learning weights on the existence of bumps and stability in presence of synaptic depression.
We have seen in the previous subsection that for spike frequency adaptation $\phi_{\kappa}(z \pm a, t) = 0$, so it will not be detailed here.
With the parameters values used in our model, there is no stationary bump solution when synaptic depression is added (it shuts the neural bump activities down). We still develop the analysis, which could be used in the future to study the effect of the learning weights on an alternative system, but we do not compute values of eigenvalues and thus, we do not conclude here on stability behaviours.
We consider the original equation with $m_q^{\alpha}(x,t) = \beta_q$.

Existence of stationary bumps solution On setting the firing functions as a heaviside functions, a stationary bump solution $\left(u_0^{\alpha}(x), q_0^{\alpha}(x), s_0^{\alpha\beta}(x,y)\right)$ satisfies equations (4.42) (4.43) (4.25):

$$u_0^{\alpha}(x) = \begin{cases} \frac{1}{1+\alpha_q\beta_q} \sum\limits_{\beta \in E} G^{\alpha\beta} J^{\alpha\beta}(x,a) & \text{if } x \notin R[u_0^{\alpha}] \\ \frac{1}{1+\alpha_q\beta_q} \sum\limits_{\beta \in E} G^{\alpha\beta}[J^{\alpha\beta}(x,a)\xi_s - (\xi_s - 1)\kappa_{\text{in}}] & \text{if } x \in R[u_0^{\alpha}] \end{cases} \tag{4.42}$$

The excited region and bumps boundaries are defined by the same conditions described in equations (4.27) and (4.28).

$$q_0^\alpha(x) = \begin{cases} 1 & \text{if } x \notin R[u_0^\alpha] \\ \frac{1}{1+\alpha_q\beta_q} & \text{if } x \in R[u_0^\alpha] \end{cases} \tag{4.43}$$

The equilibrium solution of the learning weight factor $s_0^{\alpha\beta}(x,y)$ was defined in (4.25).

We remind that for our parameter values, this bump solution does not exist.

Stability of the bumps Following Kilpatrick and Bressloff (2010) [127], we develop the equations (4.7) (4.11) with $u^\alpha(x,t) = u_0^\alpha(x) + \epsilon\phi_u^\alpha(x,t)$ and $q^\alpha(x,t) = q_0^\alpha(x) + \epsilon\phi_q^\alpha(x,t)$, where $\psi_u^\alpha(x,t)$, $\phi_q^\alpha(x,t)$ are smooth perturations and $\epsilon << 1$. With a method similar to the one developed in the previous subsubsection 4.2.4.1, we find the general equation:

$$(\lambda+1)\psi_u^\alpha(x) = \\ \sum_{\beta\in E} G^{\alpha\beta} \sum_{z\in Z^\beta} \sum_{\sigma\in\{-1,1\}} w_{\text{tot}}^{\alpha\beta}(x, z+\sigma a)\left[1 - \frac{\beta_q \Theta(\psi_u^\beta(z+\sigma a))}{(\lambda + 1/\alpha_q + \beta_q)}\right] G(\psi_u^\beta(z+\sigma a)) \frac{\psi_u^\beta(z+\sigma a)}{|u_0'^\beta(z+\sigma a)|} \tag{4.44}$$

$\frac{1}{|u_0'^\alpha(z+\sigma a)|}$ is defined as in equation (4.35), but with π_u defined here as:

$$\pi_u = \frac{1+\alpha_q\beta_q}{2(w(0) - w(2a))} \tag{4.45}$$

The function $G(X)$ is written as:

$$G(X) = \begin{cases} 1 \text{ if } X > 0 \\ (1+\alpha_q\beta_q)^{-1} \text{ if } X < 0 \end{cases} \tag{4.46}$$

Here also, there are four classes of solutions which determine the discrete spectrum: expansion, contraction, leftward shift and rightward shift of the stationary bump solution.

Expansion case: This case corresponds to a class of solutions where $\forall\beta \in E, \forall z \in Z^\beta, \forall\sigma \in \{-1,1\}$, $\psi_u^\beta(z+\sigma a) > 0$. With the simplified equation, since all $\psi_u^\beta(z+\sigma a)$ have the same sign, all $\psi_u^\beta(z+\sigma a)$ are equal and all $\psi_u^\beta(z+\sigma a) > 0$. Finally λ satisfies the equation

$$(\lambda + \alpha_q^{-1} + \beta_q)(\lambda+1) = (\lambda + \alpha_q^{-1})(1+\alpha_q\beta_q)\Omega \tag{4.47}$$

With

$$\Omega = \frac{w(0) + w(2a)}{w(0) - w(2a)} \tag{4.48}$$

The solutions of this equation are:

$$\lambda_\pm = \frac{\Omega(1+\alpha_q\beta_q) - (1+\alpha_q^{-1}+\beta_q) \pm \sqrt{(\Omega(1+\alpha_q\beta_q) - (1+\alpha_q^{-1}+\beta_q))^2 + 4(\Omega-1)(\alpha_q^{-1}+\beta_q)}}{2} \tag{4.49}$$

These eigenvalues are independent of ξ_s, thus stability does not depend on γ.

Contraction case: This case corresponds to a class of solutions where $\forall\beta \in E, \forall z \in Z^\beta, \forall\sigma \in \{-1,1\}$, $\psi_u^\beta(z+\sigma a) < 0$. With the simplified equation, since all $\psi_u^\beta(z+\sigma a)$ have the same sign, all $\psi_u^\beta(z+\sigma a)$ are equal and all $\psi_u^\beta(z+\sigma a) < 0$. The solution is

$$\lambda = \Omega/\xi_s - 1 \tag{4.50}$$

Assuming $\Omega > 0$ and $\xi_s \geq 1$, the stability is increased by learning weights when γ increases (since $\xi_s = 1 + \gamma(1+cr)4a$).

Leftward shift case: This case corresponds to a class of solutions where $\forall \beta \in E, \forall z \in Z^\beta$, $\psi_u^\beta(z+a) < 0$ and $\psi_u^\beta(z-a) > 0$.

With the simplified equation, since all $\psi_u^\beta(z+a)$ (respectively $\psi_u^\beta(z-a)$) have the same sign, all $\psi_u^\beta(z+a)$ ($\psi_u^\beta(z-a)$) are equal.

The resulting equation is

$$\left[\Gamma_{\beta_q}(\lambda) - \pi_u(\lambda + \alpha_q^{-1})2w(0)\right]\left[\Gamma_{\beta_q}(\lambda) - \pi_u/\xi_s(\lambda + \alpha_q^{-1})2w(0)\right] - 1/\xi_s\left[\pi_u(\lambda + \alpha_q^{-1})2w(2a)\right]^2 + \frac{\lambda\alpha_q\beta_q/\xi_s\gamma_u}{1+\alpha_q\beta_q}\left[[\Gamma_{\beta_q}(\lambda) - \pi_u(\lambda + \alpha_q^{-1})2w(0)]2w(0) - [\pi_u(\lambda + \alpha_q^{-1})2w(2a)]2w(2a)\right] = 0 \tag{4.51}$$

With

$$\Gamma_{\beta_q}(\lambda) = (\lambda + \alpha_q^{-1} + \beta_q)(\lambda + 1) \tag{4.52}$$

The roots of the equation can be searched numerically, and must satisfy the conditions $\psi_u^\beta(z+a) < 0$ and $\psi_u^\beta(z-a) > 0$. But, since we do not compute them for any set of parameters, we cannot conclude on the effect of learning weights on stability in this case.

Rightward shift case: This case corresponds to a class of solutions where $\forall \beta \in E, \forall z \in Z^\beta$, $\psi_u^\beta(z+a) > 0$ and $\psi_u^\beta(z-a) < 0$. Due to the symmetry of the system, the spectrum associated with rightward shifts is identical to that of leftward shifts.

As a conclusion, even without computing eigenvalues with a given set of parameters, it was still possible to estimate the stability behaviours, provided that equilibrium bump solutions exist. As in the previous subsubsection 4.2.4.1, we found that learning weights stabilize the system through contraction, but have no effects on stability in case of an expansion perturbation. However, we cannot conclude on their influence on the shift behaviour since we did not compute eigenvalues values.

All in all, this subsection provided an analytical framework to study the three neural fields model with spike frequency adaptation, synaptic depression and learning weights.

4.2.5 Discussion

Summary The standard consolidation theory describes two interacting memory storage systems. The neocortex needs several days to consolidate its memory pattern through its different regions, but this memory can remain for years. The consolidation of the latter is ensured by the reactivations of the hippocampal engram which is fastly strengthened but also erased within a few weeks [215]. Previous computational models have reproduced SCT processes and addressed various questions [215, 160, 122, 162, 8, 104, 113]. However, to our knowledge, little attention has been paid to the underlying neurobiological processes responsible for the differences in learning and the erasure of memories between the neocortex and the hippocampus. We proposed in this paper a computational model of SCT including two current hypotheses:

- The slow consolidation in the neocortex could be explained by its large structure, implying long durations to connect remote areas of the same memory pattern.
- The forgetting of hippocampal memories could be due to adult neurogenesis in the dentate gyrus and disturbing memory retrieval.

These two considerations, within a complex spatial structure of three interconnected brain areas (neocortex, dentate gyrus, and CA regions) and following a temporal process composed of two kinds of important steps (hippocampal replay and retrieval cue) make the whole process challenging to model. This complexity, as well as the tissue-level scale of the theory, makes the neural field theory an appealing framework for SCT modelling. We proposed here an original neural field model unifying the different elements mentioned above, with original components compared with classic neural field models; such as interactions between three coupled neural fields, synaptic plasticity, or a long temporal sequence. Our numerical simulations reproduced the main features of the standard consolidation theory, summarized in figure 4.8. The neocortical pattern, initially dependent on the

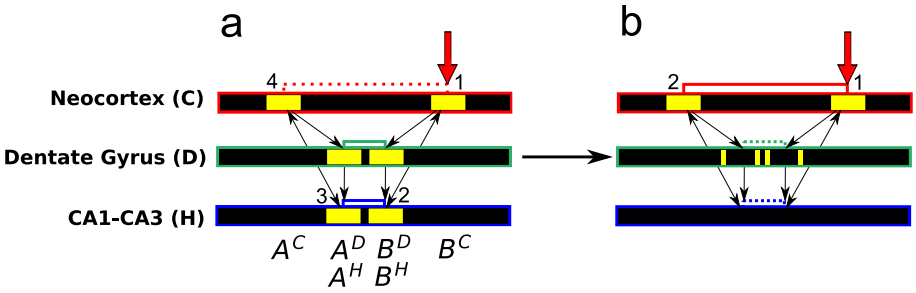

Figure 4.8: Evolution from a dependent to an independent neocortical pattern retrieval in the connected neural fields. The retrieval cue is a partial signal on only A^C or B^C in the neocortex, here B^C (vertical red arrow). **(a)** At the beginning of the whole process, when the neocortex is dependent on the hippocampus, the activity is transmitted following $1 \to 2 \to 3 \to 4$. A^C is activated via the hippocampal fields. **(b)** However at the end of the process, the cortical weights between A^C and B^C are strong enough to activate each other directly ($1 \to 2$), independently of the hippocampus whose pattern retrieval is prevented by neurogenesis in the dentate gyrus.

fastly constituted hippocampus for retrieval, becomes independent at the end of the consolidation, while the hippocampal pattern disappears.

After the encoding step, connections between neocortical modules are weaker than those in the hippocampus, because of the larger distance between them. Therefore, at this stage pattern retrieval in the neocortex needs neocortex-hippocampus connections (see figure 4.8 (a)). However with increasing time, hippocampal replay as well as retrieval cue steps induce bumps of firing and thus learning weights consolidation in the three fields, especially for connections located more remotely and in particular in the neocortex. This explains why distance-dependent learning rate takes more time to achieve highly consolidated synaptic weights in the model.
In parallel with the learning dynamics, the effect of dentate gyrus neurogenesis on the stability of hippocampal memories has also been studied. Newborn highly excitable neurons, modeled here by a reduction of the thresholds of a small fraction of dentate gyrus neurons, were introduced. Their continuous firing prevented the reactivation of both dentate gyrus and CA region patterns, due to threshold adaptations in nearby pattern neurons. Hippocampal memory retrieval is thus inhibited as soon as the neurogenesis is significant, i.e. at long timescales. Here, at long times the neocortical engram is the only one to be retrieved during the retrieval cue steps (see figure 4.8 (b)), since it does not receive direct inputs from the dentate gyrus, and thus is saved from erasure.

Finally, we provided an analytical framework to study the bump solutions and their stability for the three neural fields model with spike frequency adaptation, synaptic depression and learning weights. In particular this analysis shows that learning weights would stabilize the system when a contraction perturbation is applied.

Future directions Our computational model is highly simplified and would need to be improved in many ways. First, the learning weight equations might be refined to achieve expressions with a stronger biophysical support, as the adaptation of STDP for neural fields [195], while maintaining the continuum. In particular the phenomenological continuity function $\eta_s^{\alpha\beta}(x,t)$ could be re-evaluated, and replaced by another mechanism providing continuity of the bump solutions, an important feature in neural field models.
Further, to approach biological reality, it is important to question the pertinence of the use of neural fields for hippocampus networks since neural fields have been developed to model neocortical networks instead [51].

Moreover, the timescales used in our model are questionable. We take for reference the time constant for the neural activity $u^\alpha(x,t)$ which has been fixed equal to 1 in our model, but which is estimated to be around 10 ms experimentally [5]. In our model the synaptic resources recovery rate α_q in synaptic depression equation (4.13), should lie between 20 and 80 (since experimentally estimated to be between 200 and 800 ms [5]). However, the numerical value used in our simulations

is $\alpha_q = 800$.
Similarly, the spike frequency timescale τ_κ should be between 4 and 12 (experimentally estimated to be between 40 and 120 ms [153]). But in our numerical simulations we used $\tau_\kappa = 0.8$.
These differences between the experimental values and those used for our parameters can be explained by the complexity of the process to model. Indeed multiple timescales are present in this model, including those mentioned above, the activity-dependent synaptic resources depeletion rate $m_q^\alpha(x,t)$ (equations (4.13) (4.14)), the timescale for the threshold related to neurogenesis τ_{κ_n} (equation (4.12)), the distance-dependent learning rate $d(x,y)$ (equations (4.18) (4.19)), the forgetting rate c_0 (equation (4.20)), the duration of the stimulations $I_{\text{ext}}^\alpha(x,t)$ (equation (4.8) for $I_{\text{ext}}^C(x,t)$). So importantly, the values of these temporal parameters must be reevaluate in future works, to be closer to biological reality.
Furthermore some additional phenomenological mechanisms can be discussed. In the equation (4.12) for the threshold related to neurogenesis ${\kappa_n}^\alpha(x,t)$, a heaviside function was used for simplicity. But the effects of a smoother firing rate function would need to be studied in the future. In addition, the phenomenological introduction of an activity dependent synaptic resources depeletion rate $m_q^\alpha(x,t) = \beta_q u^\alpha(x,t)$ in equations (4.13) (4.14) was necessary in this model, but further research must be carried out to study whether this mechanism is physiological or should be removed from the equations.

This model succinctly studied the neurogenesis mechanism leading to the erasure of memories, and would need to be further developed to be fully understood as it has been in some detailed references [63, 163, 236, 21]. In particular, its integration in a neural field model in coordination with the different homeostasis processes could be investigated in more detail. Another interesting hypothesis for forgetting is evoked by experiments of silencing of engrams [223, 121].
Our model aimed to provide a proof of principle and a selection for the main ingredients to include in the model. It would then be interesting to test whether similar results can be obtained with a more realistic neural network. Such a model would allow more complex pattern configurations and more accurate learning weight dynamics rules. More detailed attention to anatomical properties of the circuits would be of great interest [193] and more realistic synaptic plasticity equations could be implemented [222].

Here, we focused on the widespread standard consolidation theory. However, there exist other models and questions around systems memory consolidation concepts.
For instance, the multiple trace theory suggests that some of the hippocampus patterns are conserved in the long term. This theory follows observations of hippocampal damages that produced temporally-graded retrograde amnesia only for semantic memories, but not for episodic ones [172]. The trace transformation theory further proposes that with a selection that depends on the circumstances at retrieval, the neocortical or the hippocampal memory which could both prevail [241]. On the other hand, the more recent concept of active systems consolidation studies into more detail the influence of sleep on consolidation [130]. Another interesting related phenomenon which has already been modeled in some connectionist models [8, 104], is systems memory reconsolidation. In this approach, it is the replay of an already consolidated memory, which can involve again the hippocampus [173].

In addition to these theories, some models suggest that the prefrontal cortex might play a key role in memory organization [140]. On the one hand, the prefrontal cortex is involved in the processing and integration of ancient neocortical memories and seems to inhibit hippocampal activity when new information is too similar to an already stored neocortical pattern [83, 191]. This has been included in a recent connectionist model [114]. On the other hand, the prefrontal cortex has also been identified to be a location for working memory [119]. It has been introduced in a computational model studying the link between working and long-term memory, while the hippocampus was seen as the place of intermediate-term memory [77]. Tonegawa also studied the role of the prefrontal cortex and the basolateral amygdala in memory reorganization [223].

Finally, the stability analyses results in the subsection 4.2.4 were not assessed numerically through the different perturbations. It is an important work to establish in the future, in particular because this analysis only provides conditions for instability. Furthermore, the synaptic depression analysis was carried out with $m_q^\alpha(x,t) = \beta_q$, but it will be important to study the case $m_q^\alpha(x,t) = \beta_q u^\alpha(x,t)$,

used in our numerical simulations.

4.3 General conclusion

We proposed in this chapter a complex model of interacting neural fields with learning rules to model a cognitive neuroscience issue, the systems memory reorganization.

This work will have to be improved in the future, but can be seen as an insight to further use neural fields modelling for cognitive computational neuroscience. Neural fields have already been used to model several cognitive processes [175] such as vision [34], or learning and memory in sensory cortices [133]. We believe that this framework constitutes an appropriate compromise between cognitive fidelity, biological fidelity and complexity.

Conclusion and perspectives

Since the previous chapters were already discussed, we provide here a general conclusion and perspectives about the modelling approaches in theoretical neuroscience.

During this thesis, several issues in neuroscience have been addressed: synaptic plasticity at corticostriatal and thalamostriatal synapses (chapter 2), modulation of Up-Down oscillations by astrocytes (chapter 3, section 3.2), the role of astrocytes in epileptic seizures (chapter 3, section 3.3), and the systems memory reorganization between the neocortex and the hippocampus (chapter 4). There is still some work to carry out to close the open topics. The new experimental data for the ITDP model at corticostriatal and thalamostriatal synapses will need to be analyzed, and the computational model will likely need some modifications. Moreover, to characterize the role of astrocytes in epileptic seizures, it will be crucial to examine in more detail the dynamics for different astrocytes parameters. I could continue to contribute to both projects in the future.

For each issue to model, appropriate features have been identified and implemented at the relevant abstraction level. Schematically, models can be organized into two classes of abstraction levels [146]. Detailed biophysical models are made with many realistic elements assessed experimentally. This method allows an in-depth comparison with experimental data. However its complexity makes it hard to tune parameters, whose values are of primary importance for the approriate modelling of the phenomenon. More abstract models with few parameters allow to overcome this problem, which provides a better understanding of the system. Moreover, the range of parameter values are often wider, which makes the model more robust. But these adavantages go hand in hand with a loss in accuracy of the prediction. It is important to underly that the abstraction level concerns low level elements (for example biochemical signalling), but also high level ones (for example social dynamics). Only the characteristics judged necessary to explain a given phenomenon are taken into account.

To identify a suitable level of abstraction for a phenomenon, it is important to know the possible experimental measurements so that the outcomes of the model can be assessed experimentally. A recording can be seen as an abstracted description of a real process, and knowing the level of reduction of such data guide the modelling approach. For examples, the calcium-based model presented in the introduction was developed in close relationship with experimental STDP experiments [98], the integrate-and-fire networks are adapted to be compared with rastergrams obtained by spike-sorting [116], and neural fields have proven to be suitable models to be compared with EEG and MEG data [117].

All in all, various levels of abstraction are necessary in computational neuroscience to deal with a wide range of spatiotemporal scales, from biophysical to cognitive processes.
However, a large issue, that is shared with other complex systems research fields, is that some macroscopic scale dynamics cannot be accurately modeled without microscopic descriptions. Indeed, precise models can often only be found at much smaller scales (for instance, biophysical single-cell and synapse dynamics) [125]. In recent years, a multiscale framework, named equation-free modelling [221], has been developed to compute coarse-level processes for models described at a finer scale. Such algorithms identify which microscopic simulations lead to the macroscopic behaviour [90].

The equation-free framework is part of the model-based methods presented throughout this thesis, organized following a bottom-up approach, see figure C 1 (Right). The basis of this method is to

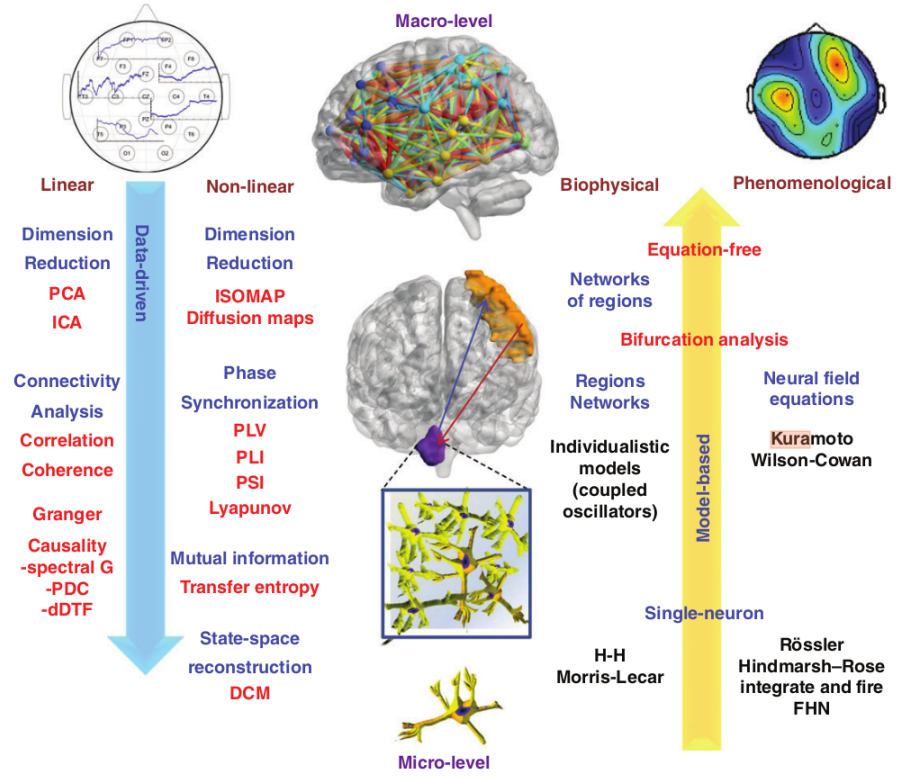

Figure C 1: Insight of bottom-up and top-down modelling methods and mathematical tools in neuroscience, adapted from Siettos and Starke (2016) [213]. Two main approaches can be distinguished, a top-down, data-driven (Left) and a bottom-up, model-based one (Right). The latter method is the one which has been used throughout this thesis.

consider first a mathematical model, and study whether complex dynamics can emerge from these equations [213].
Nevertheless, this method is not the only one used in computational neuroscience, another facet is the top-down approach, see figure C 1 (Left). Contrary to the bottom-up case, this method is data-driven [217]. It starts from measurements of brain dynamics (for instance, EEG, LFP or fMRI), then models are built to reproduce the recordings. This approach can be seen as an inverse problem solving, whose aim is to infer brain organization and mechanisms from macroscale observations [213]. Various methods exist within the top-down approach, examples include linear tools such as simple correlation and coherence [31] or Granger causality [96, 246], and nonlinear methods such as mutual information graphs [231] or manifold learning algorithms (for instance, ICA [43] or ISOMAP [12]).

Some recent studies attempt to combine both bottom-up and top-down approaches to link mechanistics dynamics to large scale recordings [93]. For instance, dynamic causal modeling (DCM) is a framework based on nonlinear ODEs describing groups of neurons (bottom-up), that aims to infer the effective connectivity of networks (top-down) [88]. DCM has been applied to various processes such as visual perception [245], emotion [176], and also to disorders such as depression [170], schizophrenia [57], or bipolar disorder [32].

To conclude with a more personal perspective, I wish that the interactions between all the different approaches to understand cognitive processes; through various disciplines and methods, experimental or theoretical, with different spatiotemporal and abstraction scales, could lead to positive applications such as better medical treatments for brain related disorders, and that the understanding of human behaviour could lead to more appropriate public policies [47].

Bibliography

[1] Covariance Matrix Adaptation Evolutionary Strategy (CMA-ES) — pagmo 2.19.0 documentation. https://esa.github.io/pagmo2/docs/cpp/algorithms/cmaes.html#_CPPv4N5pagmo5cmaesE.

[2] List of algorithms — pygmo 2.19.5 documentation. https://esa.github.io/pygmo2/algorithms.html.

[3] A model of neuronal bursting using three coupled first order differential equations. *Proceedings of the Royal Society of London. Series B. Biological Sciences*, 221(1222):87–102, Mar. 1984.

[4] A. H. Abbassian, M. Fotouhi, and M. Heidari. Neural fields with fast learning dynamic kernel. *Biological Cybernetics*, 106(1):15–26, Jan. 2012.

[5] L. F. Abbott, J. A. Varela, K. Sen, and S. B. Nelson. Synaptic Depression and Cortical Gain Control. *Science*, 275(5297):221–224, Jan. 1997.

[6] M. Abeles and M. Goldstein. Multispike train analysis. *Proceedings of the IEEE*, 65(5):762–773, 1977.

[7] T. D. Albright, E. R. Kandel, and M. I. Posner. Cognitive neuroscience. *Current Opinion in Neurobiology*, 10(5):612–624, Oct. 2000.

[8] O. B. Amaral, R. Osan, R. Roesler, and A. B. Tort. A synaptic reinforcement-based model for transient amnesia following disruptions of memory consolidation and reconsolidation. *Hippocampus*, 18(6):584–601, June 2008.

[9] S.-i. Amari. Dynamics of pattern formation in lateral-inhibition type neural fields. *Biological Cybernetics*, 27(2):77–87, 1977.

[10] M. Amiri, F. Bahrami, and M. Janahmadi. Functional contributions of astrocytes in synchronization of a neuronal network model. *Journal of Theoretical Biology*, 292:60–70, Jan. 2012.

[11] D. Amit. Model of global spontaneous activity and local structured activity during delay periods in the cerebral cortex. *Cerebral Cortex*, 7(3):237–252, Apr. 1997.

[12] A. Anderson and M. S. Cohen. Decreased small-world functional network connectivity and clustering across resting state networks in schizophrenia: An fMRI classification tutorial. *Frontiers in Human Neuroscience*, 7, 2013.

[13] R. G. Andrzejak, C. Rummel, F. Mormann, and K. Schindler. All together now: Analogies between chimera state collapses and epileptic seizures. *Scientific Reports*, 6(1):23000, Mar. 2016.

[14] A. Araque, G. Carmignoto, P. G. Haydon, S. H. R. Oliet, R. Robitaille, and A. Volterra. Gliotransmitters travel in time and space. *Neuron*, 81(4):728–739, Feb. 2014.

[15] D. Avitabile, M. Desroches, and E. Knobloch. Spatiotemporal canards in neural field equations. *Physical Review E*, 95(4):042205, Apr. 2017.

[16] N. Axmacher, F. Mormann, G. Fernández, C. E. Elger, and J. Fell. Memory formation by neuronal synchronization. *Brain Research Reviews*, 52(1):170–182, Aug. 2006.

[17] E. Baird-Daniel, A. G. S. Daniel, M. Wenzel, D. Li, J.-Y. Liou, P. Laffont, M. Zhao, R. Yuste, H. Ma, and T. H. Schwartz. Glial Calcium Waves are Triggered by Seizure Activity and Not Essential for Initiating Ictal Onset or Neurovascular Coupling. *Cerebral Cortex*, 27(6):3318–3330, June 2017.

[18] N. R. Bartlett and S. C. Bartlett. Synchronization of a motor response with an anticipated sensory event. *Psychological Review*, 66:203–218, 1959.

[19] J. Basu and S. A. Siegelbaum. The Corticohippocampal Circuit, Synaptic Plasticity, and Memory. *Cold Spring Harbor Perspectives in Biology*, 7(11):a021733, Nov. 2015.

[20] M. Bazhenov, I. Timofeev, M. Steriade, and T. J. Sejnowski. Model of thalamocortical slow-wave sleep oscillations and transitions to activated states. *Journal of Neuroscience*, 22:8691–8704, 2002.

[21] S. Becker. A computational principle for hippocampal learning and neurogenesis. *Hippocampus*, 15(6):722–738, 2005.

[22] A. Bellot-Saez, G. Cohen, A. van Schaik, L. Ooi, J. W Morley, and Y. Buskila. Astrocytic modulation of cortical oscillations. *Scientific Reports*, 8(1):11565, Aug. 2018.

[23] J. Benda and A. V. M. Herz. A Universal Model for Spike-Frequency Adaptation. *Neural Computation*, 15(11):2523–2564, Nov. 2003.

[24] J. M. Benita, A. Guillamón, G. Deco, and M. V. Sanchez-Vives. Synaptic depression and slow oscillatory activity in a biophysical network model of the cerebral cortex. *Frontiers in Computational Neuroscience*, 6:64, 2012.

[25] V. Berec. Chimera state and route to explosive synchronization. *Chaos, Solitons & Fractals*, 86:75–81, May 2016.

[26] R. L. Beurle. Properties of a Mass of Cells Capable of Regenerating Pulses. *Philosophical Transactions of the Royal Society of London. Series B, Biological Sciences*, 240(669):55–94, 1956.

[27] E. Bienenstock, L. Cooper, and P. Munro. Theory for the development of neuron selectivity: Orientation specificity and binocular interaction in visual cortex. *The Journal of Neuroscience*, 2(1):32–48, Jan. 1982.

[28] E. Bindocci, I. Savtchouk, N. Liaudet, D. Becker, G. Carriero, and A. Volterra. Three-dimensional Ca(2+) imaging advances understanding of astrocyte biology. *Science*, 356(6339):eaai8185, May 2017.

[29] L. Blum Moyse and H. Berry. Modelling the modulation of cortical Up-Down state switching by astrocytes. *PLoS Computational Biology*, 18(7):e1010296, July 2022.

[30] L. A. Bradfield, J. Bertran-Gonzalez, B. Chieng, and B. W. Balleine. The Thalamostriatal Pathway and Cholinergic Control of Goal-Directed Action: Interlacing New with Existing Learning in the Striatum. *Neuron*, 79(1):153–166, July 2013.

[31] M. A. Brazier. Spread of seizure discharges in epilepsy: Anatomical and electrophysiological considerations. *Experimental Neurology*, 36(2):263–272, Aug. 1972.

[32] M. Breakspear, G. Roberts, M. J. Green, V. T. Nguyen, A. Frankland, F. Levy, R. Lenroot, and P. B. Mitchell. Network dysfunction of emotional and cognitive processes in those at genetic risk of bipolar disorder. *Brain*, 138(11):3427–3439, Nov. 2015.

[33] P. C. Bressloff. Spatiotemporal dynamics of continuum neural fields. *Journal of Physics A: Mathematical and Theoretical*, 45(3):033001, Jan. 2012.

[34] P. C. Bressloff, J. D. Cowan, M. Golubitsky, P. J. Thomas, and M. C. Wiener. Geometric visual hallucinations, Euclidean symmetry and the functional architecture of striate cortex. *Philosophical Transactions of the Royal Society of London. Series B: Biological Sciences*, 356(1407):299–330, Mar. 2001.

[35] P. C. Bressloff and J. G. Taylor. Dynamics of compartmental model neurons. *Neural Networks*, 7(6-7):1153–1165, Jan. 1994.

[36] D. S. Brooks and M. I. Eronen. The significance of levels of organization for scientific research: A heuristic approach 1. *Studies in History and Philosophy of Science Part C: Studies in History and Philosophy of Biological and Biomedical Sciences*, 68–69:34–41, Apr. 2018.

[37] E. N. Brown, R. E. Kass, and P. P. Mitra. Multiple neural spike train data analysis: State-of-the-art and future challenges. *Nature Neuroscience*, 7(5):456–461, May 2004.

[38] N. Brunel and V. Hakim. Fast global oscillations in networks of integrate-and-fire neurons with low firing rates. *Neural Computation*, 11:1621–1671, 1999.

[39] Z. Brzosko, S. B. Mierau, and O. Paulsen. Neuromodulation of Spike-Timing-Dependent Plasticity: Past, Present, and Future. *Neuron*, 103(4):563–581, Aug. 2019.

[40] Y. Buskila, A. Bellot-Saez, and J. W. Morley. Generating brain waves, the power of astrocytes. *Frontiers in Neuroscience*, 13:1125, 2019.

[41] J. T. Cacioppo, L. G. Tassinary, and G. Berntson, editors. *Handbook of Psychophysiology*. Cambridge University Press, 3 edition, Jan. 2001.

[42] C. Cakan, C. Dimulescu, L. Khakimova, D. Obst, A. Flöel, and K. Obermayer. Spatiotemporal patterns of adaptation-induced slow oscillations in a whole-brain model of slow-wave sleep. *Frontiers in Computational Neuroscience*, 15:800101, 2021.

[43] V. D. Calhoun, J. Liu, and T. Adalı. A review of group ICA for fMRI data and ICA for joint inference of imaging, genetic, and ERP data. *NeuroImage*, 45(1):S163–S172, Mar. 2009.

[44] A. Cavagna, I. Giardina, T. Mora, and A. M. Walczak. Physical constraints in biological collective behaviour. *Current Opinion in Systems Biology*, 9:49–54, 2018.

[45] S. Chandrasekhar. Stochastic Problems in Physics and Astronomy. *Reviews of Modern Physics*, 15(1):1–89, Jan. 1943.

[46] H. Chaté, F. Ginelli, G. Grégoire, F. Peruani, and F. Raynaud. Modeling collective motion: Variations on the Vicsek model. *European Physical Journal B*, 64(3-4):451–456, Aug. 2008.

[47] C. Chevalier and M. Perona. *Homo sapiens dans la cité: comment adapter l'action publique à la psychologie humaine*. Odile Jacob, Paris, 2022.

[48] D. B. Chklovskii, B. W. Mel, and K. Svoboda. Cortical rewiring and information storage. *Nature*, 431(7010):782–788, Oct. 2004.

[49] C. Clopath, L. Büsing, E. Vasilaki, and W. Gerstner. Connectivity reflects coding: A model of voltage-based STDP with homeostasis. *Nature Neuroscience*, 13(3):344–352, Mar. 2010.

[50] A. Compte, M. V. Sanchez-Vives, D. A. McCormick, and X.-J. Wang. Cellular and network mechanisms of slow oscillatory activity (<1 Hz) and wave propagations in a cortical network model. *Journal of Neurophysiology*, 89(5):2707–2725, May 2003.

[51] S. Coombes. Waves, bumps, and patterns in neural field theories. *Biological Cybernetics*, 93(2):91–108, Aug. 2005.

[52] S. Coombes, P. Beim Graben, and R. Potthast. Tutorial on Neural Field Theory. In S. Coombes, P. Beim Graben, R. Potthast, and J. Wright, editors, *Neural Fields*, pages 1–43. Springer Berlin Heidelberg, Berlin, Heidelberg, 2014.

[53] S. Coombes and M. R. Owen. Bumps, Breathers, and Waves in a Neural Network with Spike Frequency Adaptation. *Physical Review Letters*, 94(14):148102, Apr. 2005.

[54] R. Cossart, D. Aronov, and R. Yuste. Attractor dynamics of network UP states in the neocortex. *Nature*, 423(6937):283–288, May 2003.

[55] D. A. Coulter and C. Steinhäuser. Role of Astrocytes in Epilepsy. *Cold Spring Harbor Perspectives in Medicine*, 5(3):a022434, Jan. 2015.

[56] R. L. Cowan and C. J. Wilson. Spontaneous firing patterns and axonal projections of single corticostriatal neurons in the rat medial agranular cortex. *Journal of Neurophysiology*, 71(1):17–32, Jan. 1994.

[57] L.-B. Cui, J. Liu, L.-X. Wang, C. Li, Y.-B. Xi, F. Guo, H.-N. Wang, L.-C. Zhang, W.-M. Liu, H. He, P. Tian, H. Yin, and H. Lu. Anterior cingulate cortex-related connectivity in first-episode schizophrenia: A spectral dynamic causal modeling study with functional magnetic resonance imaging. *Frontiers in Human Neuroscience*, 9, Nov. 2015.

[58] G. Dallérac, O. Chever, and N. Rouach. How do astrocytes shape synaptic transmission? Insights from electrophysiology. *Frontiers in Cellular Neuroscience*, 7, 2013.

[59] F. David, J. T. Schmiedt, H. L. Taylor, G. Orban, G. D. Giovanni, V. N. Uebele, J. J. Renger, R. C. Lambert, N. Leresche, and V. Crunelli. Essential thalamic contribution to slow waves of natural sleep. *The Journal of Neuroscience*, 33:19599–19610, 2013.

[60] R. L. Davis and Y. Zhong. The Biology of Forgetting—A Perspective. *Neuron*, 95(3):490–503, Aug. 2017.

[61] M. De Pitta and H. Berry. A Neuron–Glial perspective for computational neuroscience. In M. De Pitta and H. Berry, editors, *Computational Glioscience*, pages 3–35. Springer, 2019.

[62] M. De Pittà, V. Volman, H. Berry, and E. Ben-Jacob. A Tale of Two Stories: Astrocyte Regulation of Synaptic Depression and Facilitation. *PLoS Computational Biology*, 7(12):e1002293, Dec. 2011.

[63] K. Deisseroth, S. Singla, H. Toda, M. Monje, T. D. Palmer, and R. C. Malenka. Excitation-Neurogenesis Coupling in Adult Neural Stem/Progenitor Cells. *Neuron*, 42(4):535–552, May 2004.

[64] A. Destexhe and C. Bedard. Local field potential. *Scholarpedia*, 8(8):10713, 2013.

[65] G. I. Detorakis and N. P. Rougier. A Neural Field Model of the Somatosensory Cortex: Formation, Maintenance and Reorganization of Ordered Topographic Maps. *PLoS ONE*, 7(7):e40257, 12 juil. 2012.

[66] M. di Bernardo, C. J. Budd, A. R. Champneys, and P. Kowalczyk. *Piecewise-Smooth Dynamical Systems: Theory and Applications*. Applied Mathematical Sciences. Springer, Jan. 2008.

[67] E. Díaz-Hernández, R. Contreras-López, A. Sánchez-Fuentes, L. Rodríguez-Sibrían, J. O. Ramírez-Jarquín, and F. Tecuapetla. The Thalamostriatal Projections Contribute to the Initiation and Execution of a Sequence of Movements. *Neuron*, 100(3):739–752.e5, Nov. 2018.

[68] A. D. Ekstrom, M. J. Kahana, J. B. Caplan, T. A. Fields, E. A. Isham, E. L. Newman, and I. Fried. Cellular networks underlying human spatial navigation. *Nature*, 425(6954):184–188, Sept. 2003.

[69] T. A. Engel, N. A. Steinmetz, M. A. Gieselmann, A. Thiele, T. Moore, and K. Boahen. Selective modulation of cortical state during spatial attention. *Science*, 354(6316):1140–1144, Dec. 2016.

[70] B. G. Ermentrout and J. D. Cowan. A mathematical theory of visual hallucination patterns. *Biological Cybernetics*, 34(3):137–150, 1979.

[71] G. Ermentrout and C. Chow. Modeling neural oscillations. *Physiology & Behavior*, 77(4-5):629–633, Dec. 2002.

[72] G. B. Ermentrout and J. B. McLeod. Existence and uniqueness of travelling waves for a neural network. *Proceedings of the Royal Society of Edinburgh: Section A Mathematics*, 123(3):461–478, 1993.

[73] T. Fellin. Communication between neurons and astrocytes: Relevance to the modulation of synaptic and network activity. *Journal of Neurochemistry*, 108(3):533–544, Feb. 2009.

[74] J. Feng. *Computational Neuroscience: A Comprehensive Approach*. CRC Press, Oct. 2003.

[75] F. Ferreira, W. Erlhagen, and E. Bicho. Multi-bump solutions in a neural field model with external inputs. *Physica D: Nonlinear Phenomena*, 326:32–51, July 2016.

[76] T. A. Fiacco and K. D. McCarthy. Multiple lines of evidence indicate that gliotransmission does not occur under physiological conditions. *The Journal of Neuroscience*, 38(1):3–13, Jan. 2018.

[77] F. Fiebig and A. Lansner. Memory consolidation from seconds to weeks: A three-stage neural network model with autonomous reinstatement dynamics. *Frontiers in Computational Neuroscience*, 8, July 2014.

[78] S. Finkbeiner. Calcium waves in astrocytes-filling in the gaps. *Neuron*, 8(6):1101–1108, June 1992.

[79] R. S. Fisher, W. V. E. Boas, W. Blume, C. Elger, P. Genton, P. Lee, and J. Engel. Epileptic Seizures and Epilepsy: Definitions Proposed by the International League Against Epilepsy (ILAE) and the International Bureau for Epilepsy (IBE). *Epilepsia*, 46(4):470–472, Apr. 2005.

[80] R. FitzHugh. Mathematical models of threshold phenomena in the nerve membrane. *The Bulletin of Mathematical Biophysics*, 17(4):257–278, Dec. 1955.

[81] A. Foncelle, A. Mendes, J. Jedrzejewska-Szmek, S. Valtcheva, H. Berry, K. T. Blackwell, and L. Venance. Modulation of Spike-Timing Dependent Plasticity: Towards the Inclusion of a Third Factor in Computational Models. *Frontiers in Computational Neuroscience*, 12:49, July 2018.

[82] M. Fotouhi, M. Heidari, and M. Sharifitabar. Continuous neural network with windowed Hebbian learning. *Biological Cybernetics*, 109(3):321–332, June 2015.

[83] P. W. Frankland and B. Bontempi. The organization of recent and remote memories. *Nature Reviews Neuroscience*, 6(2):119–130, 2005.

[84] P. W. Frankland, S. Köhler, and S. A. Josselyn. Hippocampal neurogenesis and forgetting. *Trends in Neurosciences*, 36(9):497–503, Sept. 2013.

[85] P. W. Frankland, C. O'Brien, M. Ohno, A. Kirkwood, and A. J. Silva. α-CaMKII-dependent plasticity in the cortex is required for permanent memory. *Nature*, 411(6835):309–313, May 2001.

[86] W. Freeman. Hilbert transform for brain waves. *Scholarpedia*, 2(1):1338, 2007.

[87] P. Fries. A mechanism for cognitive dynamics: Neuronal communication through neuronal coherence. *Trends in Cognitive Sciences*, 9(10):474–480, Oct. 2005.

[88] K. Friston, L. Harrison, and W. Penny. Dynamic causal modelling. *NeuroImage*, 19(4):1273–1302, Aug. 2003.

[89] N. Gale, J. Rodger, M. Small, and S. Eglen. Analysis of Activity Dependent Development of Topographic Maps in Neural Field Theory with Short Time Scale Dependent Plasticity. *Mathematical Neuroscience and Applications*, Volume 2:8390, Mar. 2022.

[90] C. W. Gear, J. M. Hyman, P. G. Kevrekidid, I. G. Kevrekidis, O. Runborg, and C. Theodoropoulos. Equation-Free, Coarse-Grained Multiscale Computation: Enabling Mocroscopic Simulators to Perform System-Level Analysis. *Communications in Mathematical Sciences*, 1(4):715–762, 2003.

[91] W. Gerstner and W. M. Kistler. Mathematical formulations of Hebbian learning. *Biological Cybernetics*, 87(5-6):404–415, Dec. 2002.

[92] W. Gerstner, W. M. Kistler, R. Naud, and L. Paninski. *Neuronal Dynamics: From Single Neurons to Networks and Models of Cognition*. Cambridge University Press, 1 edition, July 2014.

[93] W. Gerstner, H. Sprekeler, and G. Deco. Theory and Simulation in Neuroscience. *Science*, 338(6103):60–65, Oct. 2012.

[94] C. Giaume and K. D. McCarthy. Control of gap-junctional communication in astrocytic networks. *Trends in Neurosciences*, 19(8):319–325, Aug. 1996.

[95] P. Goldman-Rakic. Cellular basis of working memory. *Neuron*, 14(3):477–485, Mar. 1995.

[96] C. W. J. Granger. Investigating Causal Relations by Econometric Models and Cross-spectral Methods. *Econometrica*, 37(3):424, Aug. 1969.

[97] M. Graupner. Mechanisms of induction and maintenance of spike-timing dependent plasticity in biophysical synapse models. *Frontiers in Computational Neuroscience*, 4, 2010.

[98] M. Graupner and N. Brunel. Calcium-based plasticity model explains sensitivity of synaptic changes to spike pattern, rate, and dendritic location. *Proceedings of the National Academy of Sciences*, 109(10):3991–3996, Mar. 2012.

[99] J. Griffith. On the Stability of Brain-Like Structures. *Biophysical Journal*, 3(4):299–308, July 1963.

[100] Å. Grunditz, N. Holbro, L. Tian, Y. Zuo, and T. G. Oertner. Spine Neck Plasticity Controls Postsynaptic Calcium Signals through Electrical Compartmentalization. *The Journal of Neuroscience*, 28(50):13457–13466, Dec. 2008.

[101] J. A. Gubner. *Probability and Random Processes for Electrical and Computer Engineers*. Cambridge University Press, June 2006.

[102] S. Guerra-Gomes, N. Sousa, L. Pinto, and J. F. Oliveira. Functional roles of astrocyte calcium elevations: From synapses to behavior. *Frontiers in Cellular Neuroscience*, 11:427, 2017.

[103] V. Hakim and P. Silberzan. Collective cell migration: A physics perspective. *Reports on progress in physics. Physical Society (Great Britain)*, 80(7):076601, July 2017.

[104] P. Helfer and T. R. Shultz. A computational model of systems memory consolidation and reconsolidation. *Hippocampus*, 30(7):659–677, July 2020.

[105] M. H. Hennig. Theoretical models of synaptic short term plasticity. *Frontiers in Computational Neuroscience*, 7, 2013.

[106] M. H. Hennig, M. Postlethwaite, I. D. Forsythe, and B. P. Graham. Interactions between multiple sources of short-term plasticity during evoked and spontaneous activity at the rat calyx of Held: Dynamics of short-term plasticity. *The Journal of Physiology*, 586(13):3129–3146, July 2008.

[107] K. Heuser, C. G. Nome, K. H. Pettersen, K. S. Åbjørsbråten, V. Jensen, W. Tang, R. Sprengel, E. Taubøll, E. A. Nagelhus, and R. Enger. Ca2+ Signals in Astrocytes Facilitate Spread of Epileptiform Activity. *Cerebral Cortex*, 28(11):4036–4048, Nov. 2018.

[108] S. Hill and G. Tononi. Modeling sleep and wakefulness in the thalamocortical system. *Journal of Neurophysiology*, 93:1671–1698, 2005.

[109] A. L. Hodgkin and A. F. Huxley. A quantitative description of membrane current and its application to conduction and excitation in nerve. *The Journal of Physiology*, 117(4):500–544, Aug. 1952.

[110] D. Holcman and M. Tsodyks. The emergence of up and down states in cortical networks. *PLoS Computational Biology*, 2(3), 2006.

[111] J. Hopfield. Hopfield network. *Scholarpedia*, 2(5):1977, 2007.

[112] V. Houades, A. Koulakoff, P. Ezan, I. Seif, and C. Giaume. Gap Junction-Mediated Astrocytic Networks in the Mouse Barrel Cortex. *The Journal of Neuroscience*, 28(20):5207–5217, May 2008.

[113] M. D. Howard, S. W. Skorheim, and P. K. Pilly. A model of bi-directional interactions between complementary learning systems for memory consolidation of sequential experiences. *Frontiers in Systems Neuroscience*, 16:972235, Oct. 2022.

[114] T. Hwu and J. L. Krichmar. A neural model of schemas and memory encoding. *Biological Cybernetics*, 114(2):169–186, Apr. 2020.

[115] S. Jäkel and L. Dimou. Glial cells and their function in the adult brain: A journey through the history of their ablation. *Frontiers in Cellular Neuroscience*, 11:24, 2017.

[116] D. Jercog, A. Roxin, P. Barthó, A. Luczak, A. Compte, and J. de la Rocha. UP-DOWN cortical dynamics reflect state transitions in a bistable network. *eLife*, 6:e22425, Aug. 2017.

[117] V. Jirsa, K. Jantzen, A. Fuchs, and J. Kelso. Spatiotemporal forward solution of the EEG and MEG using network modeling. *IEEE Transactions on Medical Imaging*, 21(5):493–504, May 2002.

[118] P. Jiruska, M. de Curtis, J. G. R. Jefferys, C. A. Schevon, S. J. Schiff, and K. Schindler. Synchronization and desynchronization in epilepsy: Controversies and hypotheses. *The Journal of Physiology*, 591(4):787–797, 2013.

[119] F. Joaquin. Cognitive functions of the prefrontal cortex. *Frontiers in Human Neuroscience*, 4, 2010.

[120] S. A. Josselyn, S. Köhler, and P. W. Frankland. Finding the engram. *Nature Reviews Neuroscience*, 16(9):521–534, Sept. 2015.

[121] S. A. Josselyn and S. Tonegawa. Memory engrams: Recalling the past and imagining the future. *Science*, 367(6473):eaaw4325, Jan. 2020.

[122] S. Káli and P. Dayan. Off-line replay maintains declarative memories in a model of hippocampal-neocortical interactions. *Nature Neuroscience*, 7(3):286–294, Mar. 2004.

[123] E. R. Kandel. The Molecular Biology of Memory Storage: A Dialogue Between Genes and Synapses. *Science*, 294(5544):1030–1038, Nov. 2001.

[124] J. Kardos, Z. Szabó, and L. Héja. Framing Neuro-Glia Coupling in Antiepileptic Drug Design: Miniperspective. *Journal of Medicinal Chemistry*, 59(3):777–787, Feb. 2016.

[125] I. G. Kevrekidis and G. Samaey. Equation-Free Multiscale Computation: Algorithms and Applications. *Annual Review of Physical Chemistry*, 60(1):321–344, May 2009.

[126] Z. P. Kilpatrick and P. C. Bressloff. Effects of synaptic depression and adaptation on spatiotemporal dynamics of an excitatory neuronal network. *Physica D: Nonlinear Phenomena*, 239(9):547–560, May 2010.

[127] Z. P. Kilpatrick and P. C. Bressloff. Stability of bumps in piecewise smooth neural fields with nonlinear adaptation. *Physica D: Nonlinear Phenomena*, 239(12):1048–1060, June 2010.

[128] K. Kishimoto and S. Amari. Existence and stability of local excitations in homogeneous neural fields. *Journal of Mathematical Biology*, 7(4):303–318, 1979.

[129] H. Kitano. Biological robustness. *Nature Reviews Genetics*, 5(11):826–837, Nov. 2004.

[130] J. G. Klinzing, N. Niethard, and J. Born. Mechanisms of systems memory consolidation during sleep. *Nature Neuroscience*, 22(10):1598–1610, Oct. 2019.

[131] S. Y. Ko and P. W. Frankland. Neurogenesis-dependent transformation of hippocampal engrams. *Neuroscience Letters*, 762:136176, Sept. 2021.

[132] C. Koch. *Biophysics of Computation: Information Processing in Single Neurons*. Oxford University Press, Oct. 2004.

[133] T. Kohonen. Physiological interpretation of the Self-Organizing Map algorithm. *Neural Networks*, 6(7):895–905, Jan. 1993.

[134] L. F. Koziol and D. E. Budding. Procedural Learning. In N. M. Seel, editor, *Encyclopedia of the Sciences of Learning*, pages 2694–2696. Springer US, Boston, MA, 2012.

[135] M. A. Kramer, W. Truccolo, U. T. Eden, K. Q. Lepage, L. R. Hochberg, E. N. Eskandar, J. R. Madsen, J. W. Lee, A. Maheshwari, E. Halgren, C. J. Chu, and S. S. Cash. Human seizures self-terminate across spatial scales via a critical transition. *Proceedings of the National Academy of Sciences*, 109(51):21116–21121, Dec. 2012.

[136] Y. Kuramoto. Collective synchronization of pulse-coupled oscillators and excitable units. *Physica D: Nonlinear Phenomena*, 50(1):15–30, May 1991.

[137] C. R. Laing and W. C. Troy. Two-bump solutions of Amari-type models of neuronal pattern formation. *Physica D: Nonlinear Phenomena*, 178(3-4):190–218, Apr. 2003.

[138] C. R. Laing, W. C. Troy, B. Gutkin, and G. B. Ermentrout. Multiple Bumps in a Neuronal Model of Working Memory. *SIAM Journal on Applied Mathematics*, 63(1):62–97, Jan. 2002.

[139] C. Lainscsek, N. Rungratsameetaweemana, S. S. Cash, and T. J. Sejnowski. Cortical chimera states predict epileptic seizures. *Chaos: An Interdisciplinary Journal of Nonlinear Science*, 29(12):121106, Dec. 2019.

[140] S. Laroche, S. Davis, and T. M. Jay. Plasticity at hippocampal to prefrontal cortex synapses: Dual roles in working memory and consolidation. *Hippocampus*, 10(4):438–446, 2000.

[141] E. Ledoux and N. Brunel. Dynamics of networks of excitatory and inhibitory neurons in response to time-dependent inputs. *Frontiers in Computational Neuroscience*, 5, 2011.

[142] H. S. Lee, A. Ghetti, A. Pinto-Duarte, X. Wang, G. Dziewczapolski, F. Galimi, S. Huitron-Resendiz, J. C. Piña-Crespo, A. J. Roberts, I. M. Verma, T. J. Sejnowski, and S. F. Heinemann. Astrocytes contribute to gamma oscillations and recognition memory. *Proceedings of the National Academy of Sciences of the United States of America*, 111(32):E3343–E3352, Aug. 2014.

[143] M. Lemieux, J.-Y. Chen, P. Lonjers, M. Bazhenov, and I. Timofeev. The impact of cortical deafferentation on the neocortical slow oscillation. *The Journal of Neuroscience*, 34:5689–5703, 2014.

[144] F. Leroy, D. H. Brann, T. Meira, and S. A. Siegelbaum. Input-Timing-Dependent Plasticity in the Hippocampal CA2 Region and Its Potential Role in Social Memory. *Neuron*, 95(5):1089–1102.e5, Aug. 2017.

[145] B. Leuner, S. Mendolia-Loffredo, Y. Kozorovitskiy, D. Samburg, E. Gould, and T. J. Shors. Learning Enhances the Survival of New Neurons beyond the Time when the Hippocampus Is Required for Memory. *The Journal of Neuroscience*, 24(34):7477–7481, Aug. 2004.

[146] D. Levenstein, V. A. Alvarez, A. Amarasingham, H. Azab, Z. S. Chen, R. C. Gerkin, A. Hasenstaub, R. Iyer, R. B. Jolivet, S. Marzen, J. D. Monaco, A. A. Prinz, S. Quraishi, F. Santamaria, S. Shivkumar, M. F. Singh, R. Traub, F. Nadim, H. G. Rotstein, and A. D. Redish. On the Role of Theory and Modeling in Neuroscience. *The Journal of Neuroscience*, 43(7):1074–1088, Feb. 2023.

[147] S. Lim and J. Rinzel. Noise-induced transitions in slow wave neuronal dynamics. *Journal of Computational Neuroscience*, 28(1):1–17, 2010.

[148] J. Lisman and R. Morris. Why is the cortex a slow learner? *Nature*, 411(6835):248–249, May 2001.

[149] J. Lisman and N. Spruston. Postsynaptic depolarization requirements for LTP and LTD: A critique of spike timing-dependent plasticity. *Nature Neuroscience*, 8(7):839–841, July 2005.

[150] J. Lisman and N. Spruston. Questions about STDP as a General Model of Synaptic Plasticity. *Frontiers in Synaptic Neuroscience*, 2, 2010.

[151] A. Luczak, P. Barthó, S. L. Marguet, G. Buzsáki, and K. D. Harris. Sequential structure of neocortical spontaneous activity in vivo. *Proceedings of the National Academy of Sciences of the United States of America*, 104(1):347–352, Jan. 2007.

[152] B. B. Machta, R. Chachra, M. K. Transtrum, and J. P. Sethna. Parameter Space Compression Underlies Emergent Theories and Predictive Models. *Science*, 342(6158):604–607, Nov. 2013.

[153] D. V. Madison and R. A. Nicoll. Control of the repetitive discharge of rat CA 1 pyramidal neurones in vitro. *The Journal of Physiology*, 354(1):319–331, Sept. 1984.

[154] S. Mahon. Relationship between EEG Potentials and Intracellular Activity of Striatal and Cortico-striatal Neurons: An In Vivo Study under Different Anesthetics. *Cerebral Cortex*, 11(4):360–373, Apr. 2001.

[155] S. Majhi, B. K. Bera, D. Ghosh, and M. Perc. Chimera states in neuronal networks: A review. *Physics of Life Reviews*, 28:100–121, Mar. 2019.

[156] S. Makovkin, E. Kozinov, M. Ivanchenko, and S. Gordleeva. Controlling synchronization of gamma oscillations by astrocytic modulation in a model hippocampal neural network. *Scientific Reports*, 12(1):6970, Apr. 2022.

[157] T. Manninen, R. Havela, and M.-L. Linne. Computational Models for Calcium-Mediated Astrocyte Functions. *Frontiers in Computational Neuroscience*, 12:14, Apr. 2018.

[158] D. Marr, D. Willshaw, and B. McNaughton. Simple Memory: A Theory for Archicortex. In L. Vaina, editor, *From the Retina to the Neocortex*, pages 59–128. Birkhäuser Boston, Boston, MA, 1991.

[159] S. J. Martin, P. D. Grimwood, and R. G. M. Morris. Synaptic Plasticity and Memory: An Evaluation of the Hypothesis. *Annual Review of Neuroscience*, 23(1):649–711, Mar. 2000.

[160] J. L. McClelland, B. L. McNaughton, and R. C. O'Reilly. Why there are complementary learning systems in the hippocampus and neocortex: Insights from the successes and failures of connectionist models of learning and memory. *Psychological Review*, 102(3):419–457, 1995.

[161] R. J. McGinn, E. L. Von Stein, J. E. Summers Stromberg, and Y. Li. Precision medicine in epilepsy. In *Progress in Molecular Biology and Translational Science*, volume 190, pages 147–188. Elsevier, 2022.

[162] M. Meeter and J. M. J. Murre. Tracelink: A model of consolidation and amnesia. *Cognitive Neuropsychology*, 22(5):559–587, July 2005.

[163] L. A. Meltzer, R. Yabaluri, and K. Deisseroth. A role for circuit homeostasis in adult neurogenesis. *Trends in Neurosciences*, 28(12):653–660, Dec. 2005.

[164] A. Mendes, G. Vignoud, S. Perez, E. Perrin, J. Touboul, and L. Venance. Concurrent Thalamostriatal and Corticostriatal Spike-Timing-Dependent Plasticity and Heterosynaptic Interactions Shape Striatal Plasticity Map. *Cerebral Cortex*, 30(8):4381–4401, June 2020.

[165] S. D. Meriney and E. Fanselow. *Synaptic Transmission*. Elsevier, 2019.

[166] T. Minamimoto, Y. Hori, and M. Kimura. Complementary Process to Response Bias in the Centromedian Nucleus of the Thalamus. *Science*, 308(5729):1798–1801, June 2005.

[167] P. Missonnier, M.-P. Deiber, G. Gold, P. Millet, M. Gex-Fabry Pun, L. Fazio-Costa, P. Giannakopoulos, and V. Ibáñez. Frontal theta event-related synchronization: Comparison of directed attention and working memory load effects. *Journal of Neural Transmission*, 113(10):1477–1486, Oct. 2006.

[168] F. Mormann, T. Kreuz, R. G. Andrzejak, P. David, K. Lehnertz, and C. E. Elger. Epileptic seizures are preceded by a decrease in synchronization. *Epilepsy Research*, 53(3):173–185, Mar. 2003.

[169] C. Morris and H. Lecar. Voltage oscillations in the barnacle giant muscle fiber. *Biophysical Journal*, 35(1):193–213, July 1981.

[170] D. R. Musgrove, L. E. Eberly, B. Klimes-Dougan, Z. Basgoze, K. M. Thomas, B. A. Mueller, A. Houri, K. O. Lim, and K. R. Cullen. Impaired Bottom-Up Effective Connectivity Between Amygdala and Subgenual Anterior Cingulate Cortex in Unmedicated Adolescents with Major Depression: Results from a Dynamic Causal Modeling Analysis. *Brain Connectivity*, 5(10):608–619, Dec. 2015.

[171] L. Nadel. Multiple Memory Systems: What and Why. *Journal of Cognitive Neuroscience*, 4(3):179–188, July 1992.

[172] L. Nadel and M. Moscovitch. Memory consolidation, retrograde amnesia and the hippocampal complex. *Current Opinion in Neurobiology*, 7(2):217–227, Apr. 1997.

[173] K. Nader and E. Ö. Einarsson. Memory reconsolidation: An update. *Annals of the New York Academy of Sciences*, 1191(1):27–41, Mar. 2010.

[174] J. Nagumo, S. Arimoto, and S. Yoshizawa. An Active Pulse Transmission Line Simulating Nerve Axon. *Proceedings of the IRE*, 50(10):2061–2070, Oct. 1962.

[175] L. I. Newman and T. A. Polk. The Computational Cognitive Neuroscience of Learning and Memory: Principles and Models. In *Advances in Psychology*, volume 139, pages 77–99. Elsevier, 2008.

[176] V. T. Nguyen, M. Breakspear, X. Hu, and C. C. Guo. The integration of the internal and external milieu in the insula during dynamic emotional experiences. *NeuroImage*, 124:455–463, Jan. 2016.

[177] J. A. Noriega-Prieto and A. Araque. Sensing and regulating synaptic activity by astrocytes at tripartite synapse. *Neurochemical research*, Apr. 2021.

[178] P. L. Nunez. The brain wave equation: A model for the EEG. *Mathematical Biosciences*, 21(3-4):279–297, Dec. 1974.

[179] E. Oja. Simplified neuron model as a principal component analyzer. *Journal of Mathematical Biology*, 15(3):267–273, Nov. 1982.

[180] J. F. Oliveira, V. M. Sardinha, S. Guerra-Gomes, A. Araque, and N. Sousa. Do stars govern our actions? Astrocyte involvement in rodent behavior. *Trends in Neurosciences*, 38(9):535–549, Sept. 2015.

[181] F. Oschmann, H. Berry, K. Obermayer, and K. Lenk. From in silico astrocyte cell models to neuron-astrocyte network models: A review. *Brain Research Bulletin*, 136:76–84, Jan. 2018.

[182] E. V. Pankratova, A. I. Kalyakulina, S. V. Stasenko, S. Y. Gordleeva, I. A. Lazarevich, and V. B. Kazantsev. Neuronal synchronization enhanced by neuron–astrocyte interaction. *Nonlinear Dynamics*, 97(1):647–662, July 2019.

[183] V. Parpura, T. A. Basarsky, F. Liu, K. Jeftinija, S. Jeftinija, and P. G. Haydon. Glutamate-mediated astrocyte–neuron signalling. *Nature*, 369(6483):744–747, June 1994.

[184] D. C. Patel, B. P. Tewari, L. Chaunsali, and H. Sontheimer. Neuron–glia interactions in the pathophysiology of epilepsy. *Nature Reviews Neuroscience*, 20(5):282–297, May 2019.

[185] G. Perea, M. Navarrete, and A. Araque. Tripartite synapses: Astrocytes process and control synaptic information. *Trends in neurosciences*, 32(8):421–431, Aug. 2009.

[186] E. Perrin. *Interaction Des Plasticités Cortico-Striatales et Thalamo-Striatales Lors d'un Apprentissage Procédural et de l'adaptation Sensorimotrice*. These de doctorat, Sorbonne université, Oct. 2022.

[187] E. Perrin and L. Venance. Bridging the gap between striatal plasticity and learning. *Current Opinion in Neurobiology*, 54:104–112, Feb. 2019.

[188] C. C. H. Petersen, T. T. G. Hahn, M. Mehta, A. Grinvald, and B. Sakmann. Interaction of sensory responses with spontaneous depolarization in layer 2/3 barrel cortex. *Proceedings of the National Academy of Sciences of the United States of America*, 100(23):13638–13643, Nov. 2003.

[189] K. E. Poskanzer and R. Yuste. Astrocytic regulation of cortical UP states. *Proceedings of the National Academy of Sciences of the United States of America*, 108(45):18453–18458, Nov. 2011.

[190] K. E. Poskanzer and R. Yuste. Astrocytes regulate cortical state switching in vivo. *Proceedings of the National Academy of Sciences of the United States of America*, 113(19):E2675–E2684, May 2016.

[191] A. R. Preston and H. Eichenbaum. Interplay of Hippocampus and Prefrontal Cortex in Memory. *Current Biology*, 23(17):R764–R773, Sept. 2013.

[192] A. A. Prinz, D. Bucher, and E. Marder. Similar network activity from disparate circuit parameters. *Nature Neuroscience*, 7(12):1345–1352, Dec. 2004.

[193] M. Pyka and S. Cheng. Pattern Association and Consolidation Emerges from Connectivity Properties between Cortex and Hippocampus. *PLoS ONE*, 9(1):e85016, Jan. 2014.

[194] P. Rigas and M. A. Castro-Alamancos. Thalamocortical Up states: Differential effects of intrinsic and extrinsic cortical inputs on persistent activity. *The Journal of Neuroscience*, 27(16):4261–4272, Apr. 2007.

[195] P. A. Robinson. Neural field theory of synaptic plasticity. *Journal of Theoretical Biology*, 285(1):156–163, Sept. 2011.

[196] A. Roth and M. C. W. Van Rossum. Modeling Synapses. In E. De Schutter, editor, *Computational Modeling Methods for Neuroscientists*, pages 139–160. The MIT Press, Sept. 2009.

[197] A. Roxin and A. Compte. Oscillations in the bistable regime of neuronal networks. *Physical Review E*, 94(1):012410, July 2016.

[198] A. Roxin and S. Fusi. Efficient Partitioning of Memory Systems and Its Importance for Memory Consolidation. *PLoS Computational Biology*, 9(7):e1003146, 25 juil. 2013.

[199] D. A. Rusakov. Disentangling calcium-driven astrocyte physiology. *Nature Reviews Neuroscience*, 16(4):226–233, Apr. 2015.

[200] S. Sachidhanandam, V. Sreenivasan, A. Kyriakatos, Y. Kremer, and C. C. H. Petersen. Membrane potential correlates of sensory perception in mouse barrel cortex. *Nature Neuroscience*, 16(11):1671–1677, Nov. 2013.

[201] P. Salami, M. Borzello, M. A. Kramer, M. B. Westover, and S. S. Cash. Quantifying seizure termination patterns reveals limited pathways to seizure end. *Neurobiology of Disease*, 165:105645, Apr. 2022.

[202] M. V. Sanchez-Vives and D. A. McCormick. Cellular and network mechanisms of rhythmic recurrent activity in neocortex. *Nature Neuroscience*, 3(10):1027–1034, Oct. 2000.

[203] M. Santello, N. Toni, and A. Volterra. Astrocyte function from information processing to cognition and cognitive impairment. *Nature Neuroscience*, 22(2):154–166, Feb. 2019.

[204] I. Savtchouk and A. Volterra. Gliotransmission: Beyond Black-and-White. *The Journal of Neuroscience*, 38(1):14–25, Jan. 2018.

[205] O. Schwartz, J. W. Pillow, N. C. Rust, and E. P. Simoncelli. Spike-triggered neural characterization. *Journal of Vision*, 6(4):13, July 2006.

[206] G. Seifert, G. Carmignoto, and C. Steinhäuser. Astrocyte dysfunction in epilepsy. *Brain Research Reviews*, 63(1):212–221, May 2010.

[207] T. J. Sejnowski. Storing covariance with nonlinearly interacting neurons. *Journal of Mathematical Biology*, 4(4):303–321, 1977.

[208] T. J. Sejnowski, C. Koch, and P. S. Churchland. Computational Neuroscience. *Science*, 241(4871):1299–1306, Sept. 1988.

[209] T. J. Sejnowski and G. Tesauro. The Hebb Rule for Synaptic Plasticity: Algorithms and Implementations. In *Neural Models of Plasticity*, pages 94–103. Elsevier, 1989.

[210] A. Shai and M. E. Larkum. Branching into brains. *eLife*, 6:e33066, Dec. 2017.

[211] E. Shigetomi, S. Patel, and B. S. Khakh. Probing the complexities of astrocyte calcium signaling. *Trends in cell biology*, 26(4):300–312, Apr. 2016.

[212] Y. Shu, A. Hasenstaub, and D. A. McCormick. Turning on and off recurrent balanced cortical activity. *Nature*, 423(6937):288–293, May 2003.

[213] C. Siettos and J. Starke. Multiscale modeling of brain dynamics: From single neurons and networks to mathematical tools. *WIREs Systems Biology and Medicine*, 8(5):438–458, Sept. 2016.

[214] Y. Smith, A. Galvan, T. J. Ellender, N. Doig, R. M. Villalba, I. Huerta-Ocampo, T. Wichmann, and J. P. Bolam. The thalamostriatal system in normal and diseased states. *Frontiers in Systems Neuroscience*, 8, 2014.

[215] L. R. Squire and P. Alvarez. Retrograde amnesia and memory consolidation: A neurobiological perspective. *Current Opinion in Neurobiology*, 5(2):169–177, Apr. 1995.

[216] L. R. Squire, C. E. Stark, and R. E. Clark. The medial temporal lobe. *Annual Review of Neuroscience*, 27(1):279–306, July 2004.

[217] C. Stam. Nonlinear dynamical analysis of EEG and MEG: Review of an emerging field. *Clinical Neurophysiology*, 116(10):2266–2301, Oct. 2005.

[218] M. Steriade, A. Nunez, and F. Amzica. Intracellular analysis of relations between the slow ($<$ 1 Hz) neocortical oscillation and other sleep rhythms of the electroencephalogram. *The Journal of Neuroscience*, 13(8):3266–3283, Aug. 1993.

[219] E. M. Tartaglia and N. Brunel. Bistability and up/down state alternations in inhibition-dominated randomly connected networks of LIF neurons. *Scientific reports*, 7(1):11916, Sept. 2017.

[220] C. Tetzlaff, C. Kolodziejski, I. Markelic, and F. Wörgötter. Time scales of memory, learning, and plasticity. *Biological Cybernetics*, 106(11-12):715–726, Dec. 2012.

[221] C. Theodoropoulos, Y.-H. Qian, and I. G. Kevrekidis. "Coarse" stability and bifurcation analysis using time-steppers: A reaction-diffusion example. *Proceedings of the National Academy of Sciences*, 97(18):9840–9843, Aug. 2000.

[222] D. F. Tomé, S. Sadeh, and C. Clopath. Coordinated hippocampal-thalamic-cortical communication crucial for engram dynamics underneath systems consolidation. *Nature Communications*, 13(1):840, Feb. 2022.

[223] S. Tonegawa, M. D. Morrissey, and T. Kitamura. The role of engram cells in the systems consolidation of memory. *Nature Reviews Neuroscience*, 19(8):485–498, Aug. 2018.

[224] M. Torao-Angosto, A. Manasanch, M. Mattia, and M. V. Sanchez-Vives. Up and down states during slow oscillations in slow-wave sleep and different levels of anesthesia. *Frontiers in Systems Neuroscience*, 15:609645, 2021.

[225] T. Trappenberg. *Fundamentals of Computational Neuroscience*. OUP Oxford, Oct. 2009.

[226] W. Truccolo, J. A. Donoghue, L. R. Hochberg, E. N. Eskandar, J. R. Madsen, W. S. Anderson, E. N. Brown, E. Halgren, and S. S. Cash. Single-neuron dynamics in human focal epilepsy. *Nature Neuroscience*, 14(5):635–641, May 2011.

[227] M. Tsodyks, K. Pawelzik, and H. Markram. Neural Networks with Dynamic Synapses. *Neural Computation*, 10(4):821–835, May 1998.

[228] M. Tsodyks, A. Uziel, and H. Markram. T Synchrony Generation in Recurrent Networks with Frequency-Dependent Synapses. *The Journal of Neuroscience*, 20(1):RC50–RC50, Jan. 2000.

[229] C. Van Vreeswijk, L. F. Abbott, and G. Bard Ermentrout. When inhibition not excitation synchronizes neural firing. *Journal of Computational Neuroscience*, 1(4):313–321, Dec. 1994.

[230] A. Verkhratsky and M. Nedergaard. Physiology of astroglia. *Physiological Reviews*, 98(1):239–389, Jan. 2018.

[231] R. Vicente, M. Wibral, M. Lindner, and G. Pipa. Transfer entropy—a model-free measure of effective connectivity for the neurosciences. *Journal of Computational Neuroscience*, 30(1):45–67, Feb. 2011.

[232] G. Vignoud, L. Venance, and J. D. Touboul. Interplay of multiple pathways and activity-dependent rules in STDP. *PLOS Computational Biology*, 14(8):e1006184, Aug. 2018.

[233] L. M. Ward. Synchronous neural oscillations and cognitive processes. *Trends in Cognitive Sciences*, 7(12):553–559, Dec. 2003.

[234] D. J. Watts and S. H. Strogatz. Collective dynamics of 'small-world' networks. *Nature*, 393(6684):440–442, June 1998.

[235] H. Weingartner and E. S. Parker, editors. *Memory Consolidation*. Psychology Press, 0 edition, Mar. 2014.

[236] V. I. Weisz and P. F. Argibay. Neurogenesis interferes with the retrieval of remote memories: Forgetting in neurocomputational terms. *Cognition*, 125(1):13–25, Oct. 2012.

[237] J. M. Whitacre. Biological Robustness: Paradigms, Mechanisms, and Systems Principles. *Frontiers in Genetics*, 3, 2012.

[238] D. J. Willshaw, P. Dayan, and R. G. M. Morris. Memory, modelling and Marr: A commentary on Marr (1971) 'Simple memory: A theory of archicortex'. *Philosophical Transactions of the Royal Society B: Biological Sciences*, 370(1666):20140383, Apr. 2015.

[239] H. R. Wilson and J. D. Cowan. Excitatory and Inhibitory Interactions in Localized Populations of Model Neurons. *Biophysical Journal*, 12(1):1–24, Jan. 1972.

[240] H. R. Wilson and J. D. Cowan. A mathematical theory of the functional dynamics of cortical and thalamic nervous tissue. *Kybernetik*, 13(2):55–80, Sept. 1973.

[241] G. Winocur, M. Moscovitch, and B. Bontempi. Memory formation and long-term retention in humans and animals: Convergence towards a transformation account of hippocampal–neocortical interactions. *Neuropsychologia*, 48(8):2339–2356, July 2010.

[242] M. Wolfrum and O. E. Omel'chenko. Chimera states are chaotic transients. *Physical Review E*, 84(1):015201, July 2011.

[243] H. H. Yin and B. J. Knowlton. The role of the basal ganglia in habit formation. *Nature Reviews Neuroscience*, 7(6):464–476, June 2006.

[244] H. H. Yin, S. P. Mulcare, M. R. F. Hilário, E. Clouse, T. Holloway, M. I. Davis, A. C. Hansson, D. M. Lovinger, and R. M. Costa. Dynamic reorganization of striatal circuits during the acquisition and consolidation of a skill. *Nature Neuroscience*, 12(3):333–341, Mar. 2009.

[245] V. Youssofzadeh, G. Prasad, A. J. Fagan, R. B. Reilly, S. Martens, J. F. Meaney, and K. Wong-Lin. Signal Propagation in the Human Visual Pathways: An Effective Connectivity Analysis. *The Journal of Neuroscience*, 35(39):13501–13510, Sept. 2015.

[246] A. Zalesky, A. Fornito, and E. Bullmore. On the use of correlation as a measure of network connectivity. *NeuroImage*, 60(4):2096–2106, May 2012.

[247] A. Ziaeemehr, M. Zarei, and A. Sheshbolouki. Emergence of global synchronization in directed excitatory networks of type I neurons. *Scientific Reports*, 10(1):3306, Feb. 2020.

[248] F. Zubler, A. Steimer, H. Gast, and K. A. Schindler. Seizure Termination. In *International Review of Neurobiology*, volume 114, pages 187–207. Elsevier, 2014.

Supplementary materials (Chapter 4)

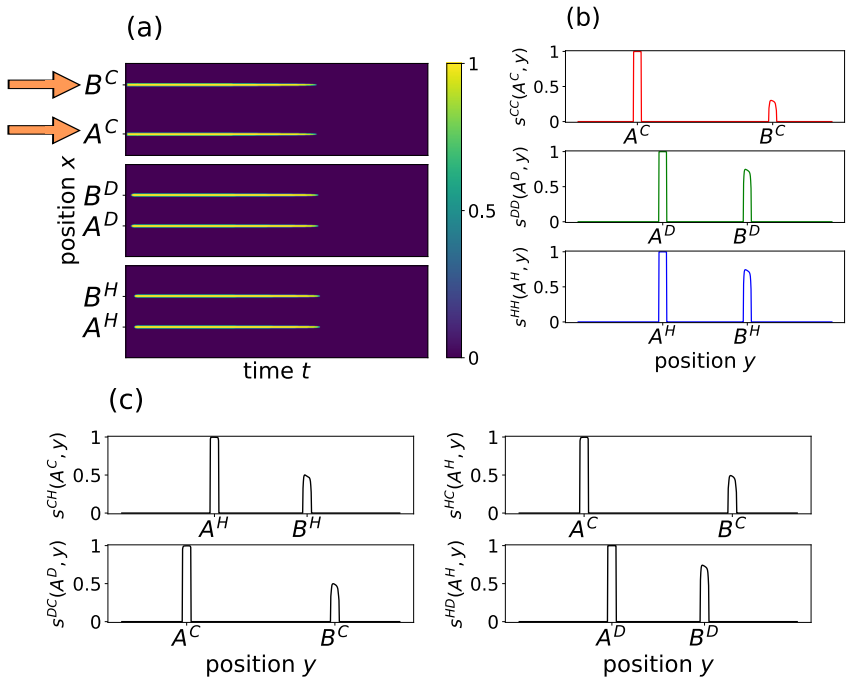

Figure S 1: The encoding phase shows faster learning in hippocampal fields than in neocortical ones. **(a)** Firing rates in the three fields, neocortex (C), dentate gyrus (D) and CA regions (H). The initial stimuli are two bumps around positions A^C and B^C in the neocortical field. They activate C neurons which in turn activate D neurons. Then since C and D neurons fire, H neurons can be activated. In the end, neurons shutdown, due to the depletion of synaptic resources. **(b)** Intra and **(c)** inter-field learning weights at the end of the encoding phase. Learning weights within the A^α part of each pattern are at their maximum. Indeed, neurons inside this location are very close to each other, so their weights grow fast. On the opposite the weights between the A^α and B^α parts are smaller, since the distance is more important. Especially these cross weights are still smaller in C than in D and H fields, since the distance between A^C and B^C is larger than those between A^D and B^D (or A^H and B^H). Thus in our model, distance is the main reason why the neocortex is a slow learner and the hippocampus a fast learner.

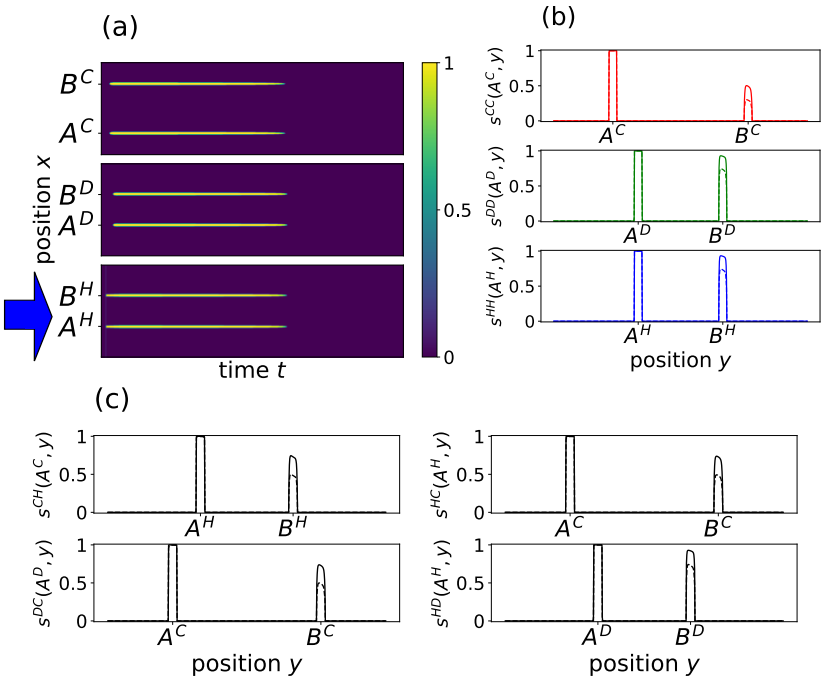

Figure S 2: The hippocampal replay step allows engrams reactivation. **(a)** Firing rates in the three fields, neocortex (C), dentate gyrus (D) and CA regions (H). We modeled hippocampal reactivation by sending a spatially uniform stimulus on H. All H neurons receive this input, but only those involved in the pattern fire for a long time, because of their non zero learning weights. Activated H neurons lead to firing in C neurons, which then activate D neurons. **(b)** Intra and **(c)** inter-field learning weights at the end of the hippocampal replay phase (solid lines) compared to learning weights at the end of the encoding phase (dotted lines). Weights consolidate thanks to pattern reactivation, in particular in the neocortex.

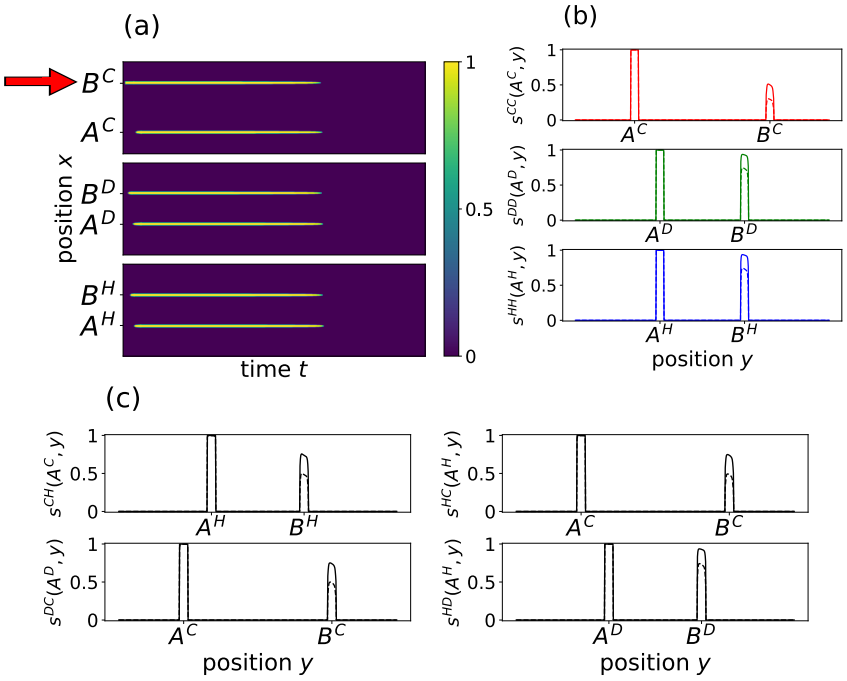

Figure S 3: The retrieval cue step allows engrams reactivation. This step consists in stimulating only the A^C or B^C location of the neocortex (here B^C). Retrieval is exhibited by subsequent activation of A^C. **(a)** Firing rates in the three fields, neocortex (C), dentate gyrus (D) and CA regions (H). A signal is sent on only B^C in the neocortical field. The weights between A^C and B^C are still small, C is still dependent on H to recover the whole pattern. Thus, B^C neurons first activate B^D then B^H neurons, which will activate A^H neurons thanks to the strong enough $B^H - A^H$ learning weights. Finally, the A^H neurons activate A^C neurons via the strong $A^C - A^H$ weights, leading to the whole pattern recovery. **(b)** Intra and **(c)** inter-field learning weights at the end of the retrieval cue process (solid lines) compared to learning weights at the end of the encoding phase (dotted lines). Weights are consolidated thanks to pattern reactivation, in particular in the neocortex.

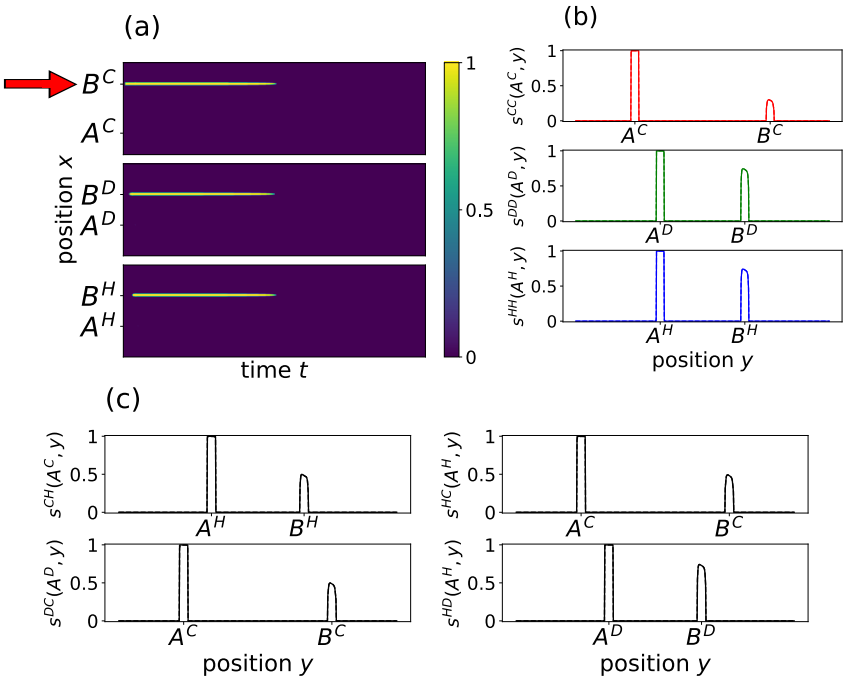

Figure S 4: Neocortical engram reactivation depends on hippocampal fields during the retrieval cue steps. The retrieval cue stimulation with hippocampal "lesion" is obtained by cancelling the learning weights amplitudes in the hippocampal fields, between them and the neocortical field ($\gamma^{\alpha\beta} = 0$ for all α,β except γ^{CC}). **(a)** Firing rates in the three fields, neocortex (C), dentate gyrus (D) and CA regions (H). Only the B^α neurons, directly stimulated by the partial retrieval cue, fire. Memory cannot be retrieved without a functional hippocampus. **(b)** The intra and **(c)** inter-field learning weights between the A^α and B^α cannot be consolidated in absence of firing of the whole pattern.

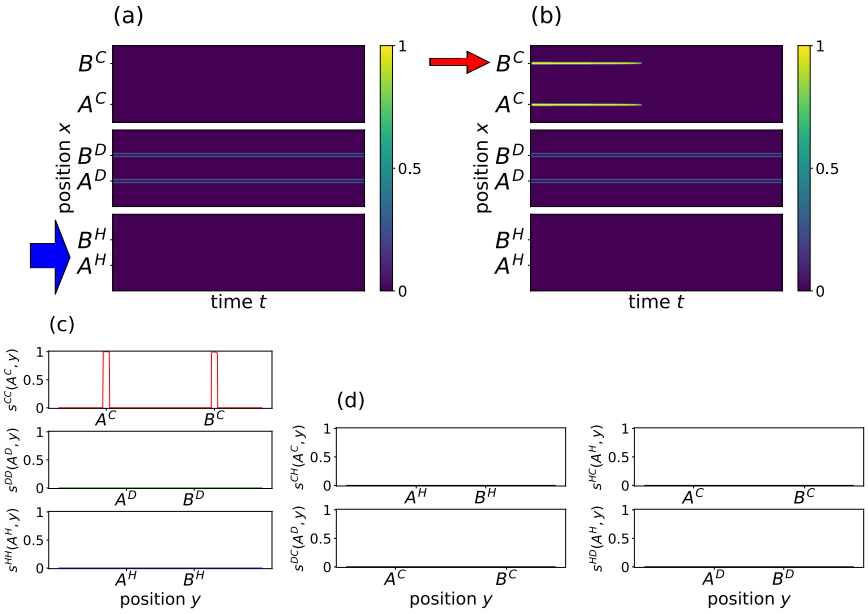

Figure S 5: Neurogenesis in the dentate gyrus prevents the reactivation of hippocampal engrams. **(a)** Firing rates in the three fields, neocortex (C), dentate gyrus (D) and CA regions (H), during the hippocampal replay phase. Neurons in the neighbourhood of the pattern in the dentate gyrus field are modeled as highly excitable newborn neurons (lower threshold, see the methods subsection 4.2.2). The thin lines in the D field show the continuous firing of those new neurons. As a result, the thresholds of the neurons in the vicinity adapt and stay high. Therefore, the neurons of the pattern stay silent in response to the replay pattern. **(b)** During neocortical retrieval cues, C neurons fire since there are no direct connections from D to C. However nothing fires in the hippocampal fields. The retrieval cue activates the whole pattern in C independently of the hippocampal fields. **(c)** Intra and **(d)** inter-field learning weights after 325 cycles with neurogenesis (solid lines). Learning weights are fully consolidated in the neocortex and have disappeared in hippocampal fields.

FOLIO ADMINISTRATIF

THESE DE L'INSA LYON, MEMBRE DE L'UNIVERSITE DE LYON

NOM : BLUM MOYSE
(avec précision du nom de jeune fille, le cas échéant)

DATE de SOUTENANCE : 14/09/2023

Prénoms : Lisa, Corinne, Hélène

TITRE : Computational neuroscience models at different levels of abstraction for synaptic plasticity, astrocyte modulation of synchronization and systems memory consolidation

NATURE : Doctorat

Numéro d'ordre : 2023ISAL0058

Ecole doctorale : Infomaths (ED512)

Spécialité : Informatique

RESUME : Dans cette thèse, des modèles théoriques à niveaux d'abstraction croissants sont développés pour aborder des questions issues d'expériences de neuroscience. Ils sont étudiés par des approches numériques et analytiques.
Avec le laboratoire de Laurent Venance (Paris), nous avons développé un modèle du protocole ITDP (input-timing-dependent plasticity) pour la plasticité des synapses cortico- et thalamo-striatales. Le modèle a été calibré par des données ex vivo et permettra de déterminer la présence de plasticité synaptique in vivo, lors d'expériences de comportement visant à déterminer le rôle des entrées corticales et thalamiques dans l'apprentissage moteur.
Au niveau des populations neuronales, j'ai étudié la modulation des comportements collectifs neuronaux par les astrocytes, en particulier la synchronisation Up-Down, une alternance spontannée entre des périodes de forte activité collective et des périodes de silence. J'ai proposé des modèles de fréquence de décharge et de réseaux de neurones à spikes de populations interconnectées de neurones et d'astrocytes. Ils proposent des explications sur la façon dont les astrocytes induisent les transitions Up-Down. Les astrocytes sont aussi probablement impliqués dans la génération des crises d'épilepsie, pendant lesquelles la synchronisation neuronale est altérée. Sur la base des modèles précédents, j'ai développé un réseau neurone-astrocyte avec une connectivité en clusters, montrant la transition entre des dynamiques Up-Down et des évènements de très forte activité mimant une crise d'épilepsie.
Enfin, au niveau du cerveau lui-même, j'ai étudié la théorie standard de la consolidation, selon laquelle la mémoire à court terme dans l'hippocampe permet la consolidation de la mémoire à long terme dans le néocortex. J'ai cherché à expliquer ce phénomène en intégrant des hypothèses biologiques – taille du néocortex expliquant la lenteur de l'apprentissage, et neurogenèse dans l'hippocampe expliquant l'effacement de sa mémoire – dans un modèle de champs neuronaux interconnectés qui reproduit bien les principales caractéristiques de la théorie.

MOTS-CLÉS : neurosciences computationnelles, input-timing-dependent plasticity, astrocytes, synchronisation, champs neuronaux, théorie de la consolidation des systèmes

Laboratoire (s) de recherche : Laboratoire d'informatique en image et systèmes d'information (LIRIS CNRS UMR5205)

Directeur de thèse: Hugues Berry

Président de jury :

Composition du jury :
Clopath, Claudia (Professor, Imperial College London, UK, Rapporteure)
Desroches, Mathieu (Chargé de Recherche HDR, Inria, Sophia-Antipolis, Rapporteur)
Delord, Bruno (Professeur, Sorbonne Université, Paris, Examinateur)
Rouzaud-Cornabas, Jonathan (Maître de conférence, Insa Lyon, Examinateur)
Berry, Hugues (Directeur de recherche, Inria, Lyon, Directeur de thèse)